Structures of aqueous surfactant systems: A study of binary micellar solutions and ternary surfactant/fatty alcohol/water emulsions

Fakultät für Naturwissenschaften

Department Chemie

der Universität Paderborn

Zur Erlangung des Grades

Dr. rer. nat.

genehmigte Dissertation

vorgelegt von

Felix Grewe

aus Paderborn

Diese Dissertation wurde in der Zeit von Mai 2010 bis Juli 2013 im Fachgebiet Physikalische Chemie am Department Chemie der Fakultät für Naturwissenschaften der Universität Paderborn unter Anleitung von Prof. Dr. Claudia Schmidt angefertigt.

Promotionskommission:

Erstgutachterin:	Prof. Dr. C. Schmidt
Zweitgutachter:	PD Dr. H. Egold
3. Mitglied:	Prof. Dr. H.-S. Kitzerow
Vorsitzender:	Prof. i.R. Dr. H. C. Marsmann

Eingereicht am:	26.07.2013
Tag der Disputation:	29.08.2013

Danksagung

Als erstes möchte ich mich bei all denjenigen bedanken, die im Folgenden nicht namentlich erwähnt werden, mich jedoch tatkräftig während meines Promotionsstudiums unterstützt haben. Mein besonderer Dank gilt jedoch:

Meiner Familie für jahrelange Unterstützung und Rückhalt.

Meiner Ehefrau Johanna, die mich jeden Tag aufs neue motiviert hat und mir jederzeit emotional zur Seite stand.

Frau Prof. Dr. Claudia Schmidt für die jahrelange Betreuung und ihre Bereitschaft jederzeit über Fragestellungen zu diskutieren.

Herrn PD Dr. Hans Egold für die Übernahme des Zweitgutachtens sowie viele Diskussionen über NMR Spektren.

Meinen ehemaligen Kollegen Dr. Richard Szopko, Dr. Gönül Ar und Dr. Mingxue Tang, die mich in den Umgang mit dem NMR Spektrometer eingeführt haben. Meinem Kollegen Martin Schneider, mit dem ich mehrere Messzeiten an der

Neutronenstreuanlage in München verbracht habe, sowie Dr. Vitaliy Pipich, der dortigen Kontaktperson, als auch Dr. Günther Goerigk, der ehemaligen Kontaktpersonen, der mir weiterhin bei Fragen zur Seite stand.

Stefanie Eriksson und Prof. Dr. Daniel Topgaard von der Universität Lund, bei denen ich Diffusions-NMR-Messungen durchführen durfte.

Dr. Frank Polzer für die Aufnahme der cryo-TEM Bilder.

Malte-Ole Schneemann für das Nachzeichnen der Konturen einzelner cryo-TEM Aufnahmen und Johannes Brinkmann für das Zählen und Vermessen

der auf den cryo-TEM Bildern zu sehenden Strukturen.

Karin Stolte aus der zentralen Analytik der Universität Paderborn für die Aufnahme unzähliger Protonenspektren.

Contents

List of Figures

List of Tables

1 Introduction

Binary surfactant/water and ternary surfactant/cosurfactant/water systems can self-assemble into a wide variety of liquid crystalline structures, which can be used for many different applications [1–3]. These structures can be investigated via NMR spectroscopy, which is a noninvasive and very versatile method. The critical micellar concentration (cmc), for example, can be determined via the change of the chemical shift which results from the change of the chemical environment of the alkyl chains of the surfactants from hydrophilic to hydrophobic [4–6]. Furthermore, phase transitions from the micellar region to a lyotropic liquid crystalline mesophase can be observed via proton NMR since the transition leads to a strong line broadening of the signals, resulting from the reduced mobility of the molecules [7]. Hence, NMR spectroscopy is a powerful tool to investigate surfactant systems.

At high surfactant concentrations of surfactant/water systems very viscous samples can be produced. Furthermore, gel-like emulsions can be made of surfactant, fatty alcohol and water mixtures even at low concentrations. For this purpose, often fatty alcohols with chain lengths longer than 12 are used as cosurfactant. Such emulsions find applications in pharmaceutical, cosmetical and personal care, laundry and food products [1–3, 8–11]. They are mixed at temperatures above the melting point of the alcohols and then cooled down below the chain melting temperature of the alcohols. Below the chain melting temperature, the alkyl chains of the alcohol are crystalline and enhance the stability of the emulsion.

For many concentrated gel forming systems in the lamellar phase region it

was found that the structure consists of uni- or multilamellar vesicles instead of extended planar lamellae [8, 12–17]. The vesicles are formed due to mechanical strain during sample preparation and are in the most cases thermodynamically not stable [17]. The shear-induced formation of multilamellar vesicles and the relation between vesicle size and shear rate were first investigated in detail by Roux [12].

As mentioned before, even highly diluted aqueous emulsions containing surfactant and fatty alcohol are able to form gel-like samples. For the system consisting of cetyl alcohol, sodium dodecyl sulfate and water, which is investigated in this PhD thesis, gel-like samples were found for water concentrations higher than 90 wt. % [2].

As for a lot of colloidal systems, the processing parameters such as temperature and shear rate have an influence on the structure of the emulsion, which can be investigated by rheo-NMR spectroscopy. With this method, the influence of shear forces on the phase structure and molecular dynamics can be investigated [18–21]. Several soft matter systems were investigated *in situ* under shear. As a nucleus for rheo-NMR, deuterium is preferred due to its sensitivity towards changes of the orientation of the molecules [22]. One disadvantage is the limitation to deuterated systems. Up to now, proton rheo-NMR is rarely used [23–25]. From this type of NMR information about the dynamic state of the alkyl chains of the surfactant and alcohol molecules may be determined. In the case of crystalline or glass-like chains, proton NMR will not yield any narrow signals of high intensity while mobile chains will provide sharp liquid like peaks.

In the following chapter 2 of this PhD thesis, the basics of aqueous surfactant systems as well as surfactant/cosurfactant systems and the methods used are explained. Chapter 3 is about the investigation of the micellization and the micellar region of the binary sodium dodecyl sulfate/water (SDS/D_2O)

system in a broad concentration range (0.007 to 35 wt. % SDS) via proton NMR spectroscopy. In addition to the changes of the chemical shift and the line width, a concentration dependency of the splitting of the α-CH_2 and CH_3 groups of the alkyl chains was found. At concentrations close to the phase transition from the micellar region to a lyotropic liquid crystalline mesophase the splitting shows a strong temperature dependence. To verify this unexpected pretransitional effect a second system, namely, cetyltrimethylammonium bromide/water (CTAB/D_2O) was investigated. In chapter 4 the results of the dilute gel-forming system SDS/CA/D_2O are presented. A series of samples with a constant water content of 97 wt. % and a varying ratio of SDS to CA was studied by differential scanning calorimetry, proton NMR spectroscopy, cryogenic transmission electron microscopy, very small angle neutron scattering, small angle X-ray scattering, pulsed field gradient NMR spectroscopy, rheology and ^{13}C solid state NMR spectroscopy. Furthermore, the influence of the alcohol chain length and three different ways of sample preparation are investigated. In chapter 5 the construction of the rf coil and the shear cell for the construction of a proton rheo-NMR probe are described. Furthermore, first measurements with this new probe are presented.

2 Fundamentals

2.1 Basics of aqueous surfactant and surfactant/ cosurfactant systems

2.1.1 Surfactant solutions

Surfactants are amphiphilic molecules which possess a polar head group and a non-polar chain. They are subdivided into anionic, cationic and nonionic surfactants depending on their head group moiety. In figure 2.1 a typical surfactant of each type is shown. Compound **1**, an anionic surfactant, is called sodium dodecyl sulfate (abbreviated as SDS) and represents the group of the alkyl sulfates. Cetyltrimethylammonium bromide (compound **2**, abbreviated as CTAB) is a cationic surfactant. A typical group of nonionic surfactants are poly(oxyethylene) alkyl ether compounds like dodecylhexaoxyethylene glycol monoether (compound **3**, abbreviated as $C_{12}E_6$).

The amphiphilic nature of the surfactants leads to their self-assembly. In water at low surfactant concentrations, the hydrocarbon chains are in the middle of the assembled aggregates and form a liquid-like hydrocarbon core while the polar headgroups create a hydrophilic surface which shields the hydrophobic area from water contact [26–28]. Such aggregates, consisting of 50 up to several hundred molecules, are called micelles and are one of the main types of amphiphilic structures. For the micellization a minimum surfactant concentration, called critical micellar concentration (abbreviated as cmc), must be reached [26, 27, 29, 30]. A further requirement for the micellization is the

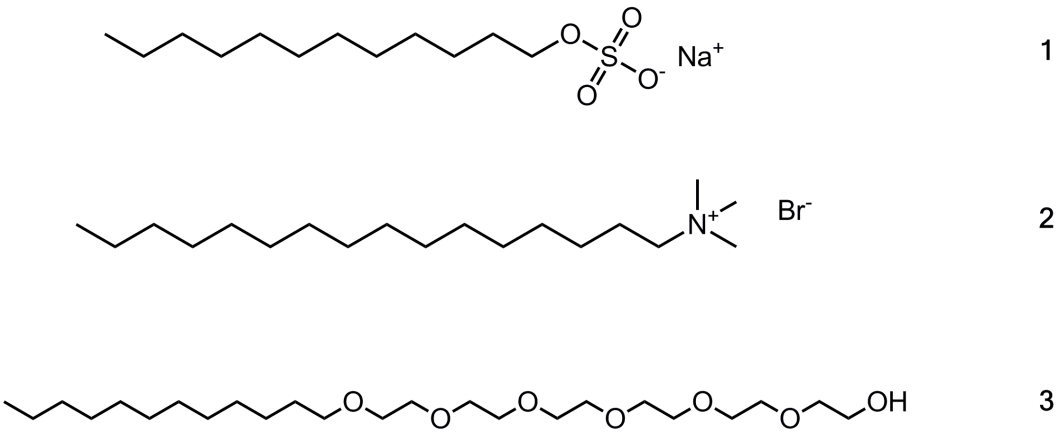

Figure 2.1: *Surfactant structures of sodium dodecyl sulfate (SDS, **1**), cetyltrimethylammonium bromide (CTAB, **2**) and dodecylhexaoxyethylene glycol monoether ($C_{12}E_6$, **3**).*

ability of the alkyl chains to occupy the core of a micelle as completely as possible [26, 31]. The micellar shape can be for example spherical, elliptical or rod-like and depends on the surfactant properties like attractive and repulsive forces as well as the molecular geometry [26, 27, 31].

Above the cmc the formation of many small micelles is entropically favored in contrast to the growth of a few large micelles. According to general assumptions, the micelles aggregate in a spherical shape before they grow with increasing concentration of surfactant. The size of the spherical micelles is limited by the length of the hydrophobic chain of the surfactants. As a consequence of the increasing number of molecules in a micelle the shape of the aggregates has to change. Otherwise cavities would develop and the stability of the micelles would decrease. For a rough prediction of the shape of the aggregates the packing parameter P (eq. 2.1) can be used. It is calculated by dividing the volume of the hydrophobic part V by the product of the minimal occupied interfacial area of the head group A and length of the hydrophobic chain in the micelle core l [26, 30, 32]:

$$P = \frac{V}{A \cdot l} \tag{2.1}$$

Packing parameters smaller than one are typical for micellar (water-soluble micelles) structures. Planar extended bilayers, large vesicles and flexible bilayer structures often have a packing parameter of one and inverse micelles (oil-soluble micelles) a packing parameter which is higher than one.

With increasing surfactant concentration the number and size of micelles increase. The interactions between the micellar surfaces are repulsive, resulting, for example, from electrostatic forces. The only possibility to maximise the spatial separation between the micelles getting closer to one another with increasing concentration is to change shape and size [26]. The resulting periodic structures are called mesophases or lyotropic liquid crystals. The structures of the lyotropic liquid crystals are influenced by the surfactant molecule, solvent, temperature and additives. Two typical liquid crystalline structures are shown in figure 2.2. When exceeding a threshold concentration of surfactant the micelles which prefer to build up disc-like aggregates will aggregate as a lamellar phase. This type of mesophase obtains a one dimensional positional order. Rod-like aggregates will create a hexagonal phase, which has a two dimensional hexagonal lattice with an orientational order of the rods and a long-range positional order [27, 28].

2.1.2 Influence of the exchange of H_2O by D_2O on the cmc

In this thesis different aqueous surfactant systems are investigated via ^{1}H NMR spectroscopy. To reduce the signal intensity of the solvent, H_2O is replaced by D_2O. This exchange has an influence on the phase boundaries.

Also, the exchange has an influence on the critical micellar concentration. Mukerjee found in 1966, for example, that the cmc of SDS is reduced from 8.27 mM in H_2O to 8.05 mM in D_2O [33]. In an article published by Berr [34], the same behavior (reduction of the cmc of SDS from 8.20 mM in H_2O to 7.60 mM in D_2O) is described. Berr found the same effect for CTAB. For

this surfactant the cmc is reduced from 1.00 mM in H_2O to 0.82 mM in D_2O. Besides the influence on the cmc, there is also an influence on the aggregation number of the micelles, which is higher in D_2O than in H_2O [34].

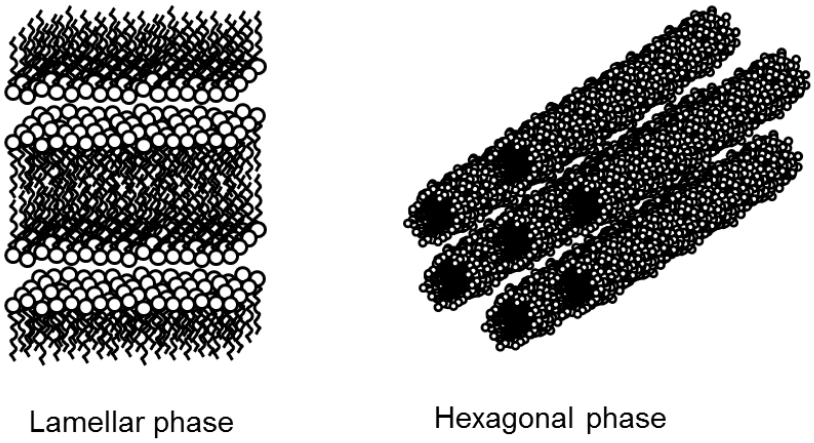

Figure 2.2: *Illustration of the lamellar and hexagonal lyotropic liquid crystalline structures.*

A typical property of amphiphilic aggregates is the ability to solubilize foreign molecules or to incorporate them into their structure. If the foreign molecule is amphiphilic and not able to build up micelles because of its poor hydrophilicity, it is called cosurfactant. In the case of mismatching packing parameters of cosurfactant and surfactant, the incorporation of the cosurfactant into the structure of the aggregates will influence shape and curvature of the aggregates [27]. Amaral, for example, found a transition from the nematic cylindrical phase to a nematic disc-like phase by adding decanol to the binary systems $C_{10}H_{21}SO_4Na$/water and $C_{12}H_{25}SO_4Na$/water [35].

2.2 Pulsed gradient spin echo NMR (PGSE NMR)

For the determination of the self-diffusion coefficients of free and hindered water, ^{1}H PGSE NMR experiments can be performed. For this purpose, the Hahn echo experiment is modified by the addition of pulsed gradients. Such experiments go back to Stejskal and Tanner in 1965 [36,37]. The pulse sequence which I used is shown in figure 2.3. It consists of a spin echo experiment with two trapezoidal gradient pulses inserted in the evolution delays.

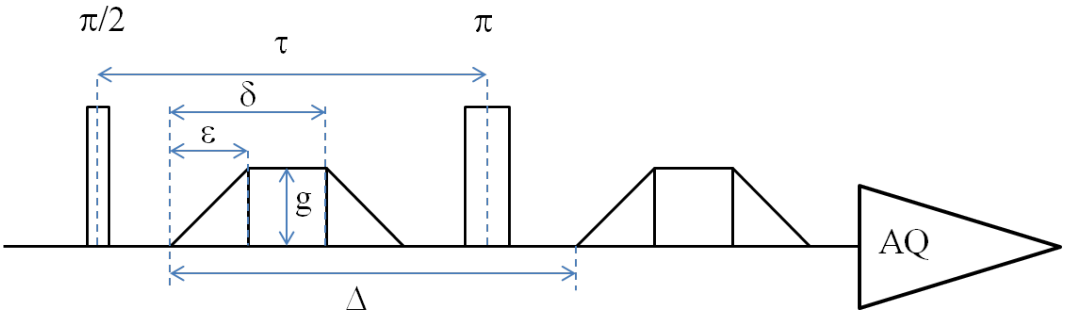

Figure 2.3: *Schematic representation of the pulsed gradient spin echo sequence used.*

τ is the time between the 90° and 180° pulse as shown in figure 2.3, Δ the temporal distance between the gradient pulses, δ the duration of the gradient as shown in figure 2.3, ϵ is the rise and fall time of the gradients, g the strength of the gradient, and 2τ the time between 90° pulse and the echo.

In figure 2.4 the pulsed field gradient spin echo experiment is presented in a very simplified way. The rotation of four magnetization vectors with the same x and y coordinates but different z coordinates is shown in the rotating frame. Relaxation processes are neglected. The magnetic field gradients are applied in z direction.

At first the PGSE experiment is explained for the case of no diffusion. The magnetizations are tilted from the z axis to the xy plane by a 90° pulse. Now the rotation of the magnetization, which depends on the strength of the magnetic field, can be detected. In a homogeneous magnetic field all the magne-

tization vectors rotate with the same frequency, the Larmor frequency. This rotation is shown in the first two columns.

During the first magnetic field gradient pulse, the total strength of the magnetic field depends on the spatial position. Hence, the rotation frequency depends on the position of the molecules, which is illustrated by different colors. As a consequence the magnetizations rotate with different frequencies and start to defocus over time (magnetization vectors from different positions are phase shifted with respect to each other). At the end of the gradient the vectors rotate again with the same Larmor frequency but remain defocused.

The next two columns show the phase of the magnetization vectors before and after the 180° pulse is applied. After the 180° pulse, the second magnetic field gradient with the same settings as the first gradient is applied. During the gradient the magnetization vectors refocus. The aligned magnetization vectors yield a maximum magnetization.

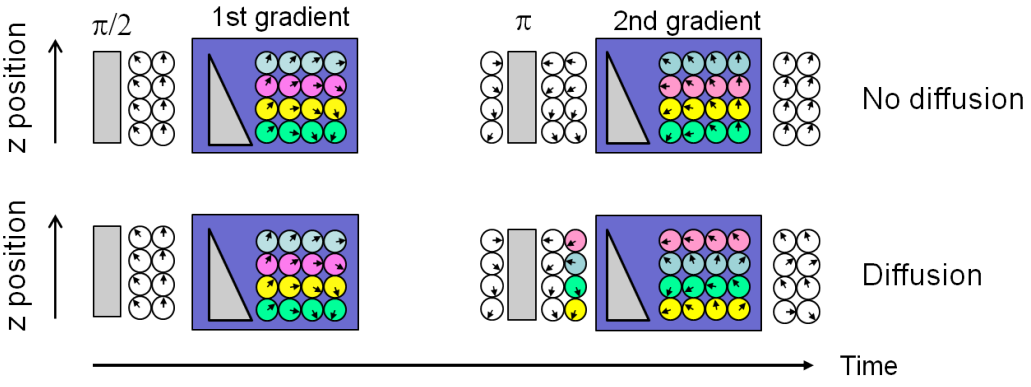

Figure 2.4: *Schematic representation of the pulsed field gradient spin echo.*

In the case of diffusion, the situation up to the end of the first gradient is the same. If the molecules change their positions between the first and the second gradient, they cannot refocus during the second gradient. The effect of diffusion of the molecules is shown for simplicity in the column before the second gradient. As a consequence the magnetization decreases and the signal intensity decreases, too.

During the evaluation process of the experimental results of the self-diffusion coefficients of water, the integrated water signals are determined as a function of the gradient strength g. In the case of only one diffusion coefficient (free water), the echo intensity is described by [38]

$$I = I_0 \exp(-\gamma^2 D g^2 \left\{\delta^2 (\Delta - \delta/3) + B\right\}). \tag{2.2}$$

γ is the gyromagnetic ratio of protons, D is the diffusion coefficient of the studied molecule, B depends on the shape of the gradient pulses and I_0 is the signal intensity in the absence of diffusion. For $B = 0$ equation 2.2 describes a PGSE sequence with rectangular gradients [38–40]. For a pulse sequence with trapezoidal gradients parameter B is defined by

$$B = \frac{\epsilon^3}{30} - \frac{\delta\epsilon^2}{6}. \tag{2.3}$$

Equation 2.4 describes the case in which more than one diffusion coefficient exists:

$$I = A_1 \cdot e^{bD_1} + A_2 \cdot e^{bD_2} + \ldots + A_n \cdot e^{bD_n} \tag{2.4}$$

$$b = -\gamma^2 g^2 \left\{\delta^2 (\Delta - \delta/3) + B\right\} \tag{2.5}$$

D_n are the different diffusion coefficients and A_n their fractions. Parameter b (eq. 2.5) is defined by the experimental settings.

The observed diffusion coefficients depend on the size of the embedding geometries with a radius R and the diffusion time Δ. The dependency is shown in figure 2.5 for different time scales $\xi = D\Delta/R^2$. For short time scales, the molecule does not diffuse far enough to feel the restriction. For $\xi \approx 1$, some of the molecules feel the restriction and an apparent diffusion coefficient, which depends on the diffusion time Δ is detected. In the case of long time scales, all molecules feel the restriction. Hence, the displacement is independent of Δ [39].

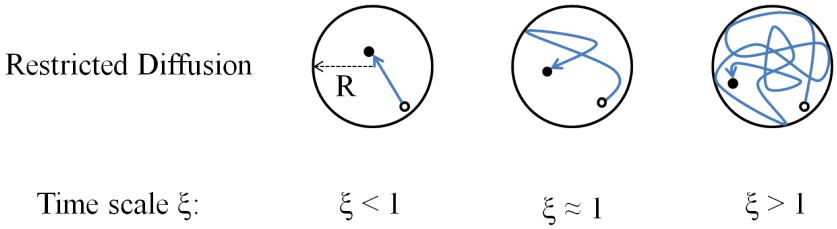

Figure 2.5: *Schematic illustration of restricted diffusion for different time scales.*

2.3 Rheology

2.3.1 Rotating experiments

Properties like flow behavior and viscosity of liquids, dispersions and emulsions are typically investigated via rheological methods. In this section the fundamental rheological parameters of rotating experiments will be defined. Imagine two plates with a liquid between them (as shown in figure 2.6). The upper plate with the shear area A is moved via the shear force F and the resulting velocity v is measured. The lower plate is fixed and therefore its velocity is zero ($v = 0$). By this process the liquid between the plates with the distance h will be sheared. Requirements, which are necessary for the exact measurement/calculation of the rheological parameters, are a laminar flow and the adhesion of the liquid to the plates. In other words, there shall not be any vortexes within the flow and the liquid shall not slip along the plates [41].

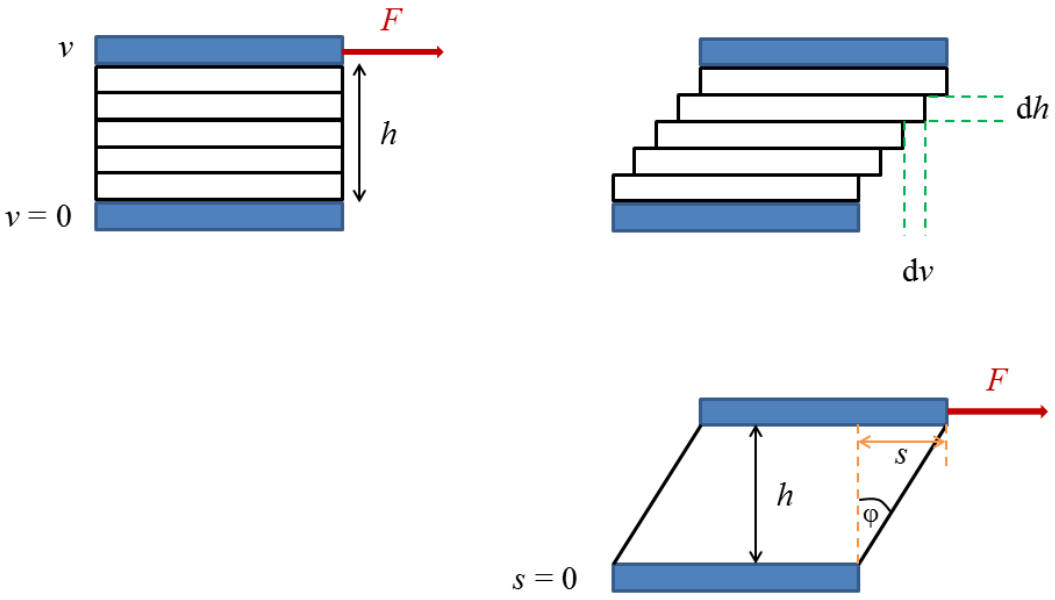

Figure 2.6: *Schematic illustration of the shear process of a liquid between two plates.*

The applied shear stress τ (unit: 1 Pa = 1 N/m^2) is defined by

$$\tau = \frac{F}{A} \tag{2.6}$$

and the shear rate $\dot{\gamma}$ (unit: 1/s) by the infinitesimal change of the velocity change dv per laminar flow layer of infinitesimal thickness dh.

$$\dot{\gamma} = \frac{\mathrm{d}v}{\mathrm{d}h} \tag{2.7}$$

Within the shear gap h the velocity decreases linearly. Therefore, the shear rate is constant all over the gap h.

The dynamic shear viscosity η (unit: 1 Pas = 1 N s/m^2), abbreviated as viscosity, of an ideal viscous fluid at a constant temperature is defined by equation

$$\eta = \frac{\tau}{\dot{\gamma}}. \tag{2.8}$$

The applied (shear) deformation (γ, unit: %) is defined by the quotient of displacement s and the plate distance h (see fig. 2.6 bottom).

$$\gamma = \frac{s}{h}. \tag{2.9}$$

To be able to perform continuous measurements for an arbitrary time, rotating instead of linear measuring systems are used. One of them is the couette geometry consisting of an outer and an inner cylinder with a gap between them. One of the cylinders is moved relative to the other. If the gap between the walls of the cylinders is small enough the shear unit can be treated as a two-plate system in good approximation. In this case, shear stress and shear rate are approximately constant and equations 2.6 to 2.9 are valid. The maximum gap width, for which the equations can be used in industrial labs, is defined by DIN EN ISO 3219 of October 1994. According to this standard, the

maximum allowed ratio $(\delta_{\mathrm{cc}})_{\max}$ between the external (R_e) and inner radius (R_i) is

$$(\delta_{\mathrm{cc}})_{\max} = \left(\frac{R_e}{R_i}\right)_{\max} = 1.0847. \tag{2.10}$$

In the case of a concentric cylinder geometry with a broad gap the velocity depends more strongly on the radius leading to a nonlinear velocity distribution. Hence, the shear rate is no longer constant and the above equations do not apply.

Figure 2.7 shows two cylindrical geometries with the maximum distance for a small gap according to the DIN norm and a geometry with a wide gap.

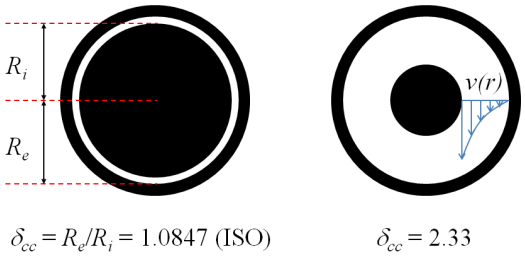

Figure 2.7: *Profiles of two cylindrical measuring systems with a small and a wide gap.*

The shear rate within the small gap is defined by [41]:

$$\dot{\gamma}_{\mathrm{cc}} = \frac{(1+\delta_{\mathrm{cc}}^2)}{(\delta_{\mathrm{cc}}^2-1)}\,\omega. \tag{2.11}$$

Here ω (unit: rad/s) is the angular velocity. The relation between rotational speed in turns per minute n (unit: 1/min) and angular velocity is defined by

$$\omega = \frac{(2\pi n)\ \mathrm{min}}{60\ \mathrm{s}}. \tag{2.12}$$

Another common measuring system is the cone-plate system, which is schematically shown in figure 2.8. According to the ISO 3219 standard, the cone angle α has to be between one and four degree and the radius R between 10 mm and 100 mm.

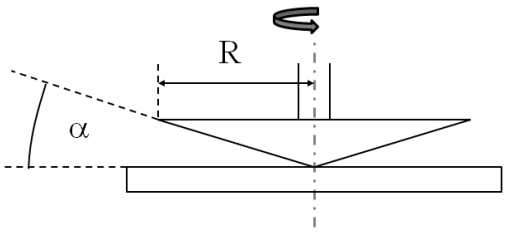

Figure 2.8: *Schematic illustration of a cone-plate geometry.*

The shear rate within the gap of the cone/plate geometry is defined [41] by

$$\dot{\gamma}_{\mathrm{cp}} = \frac{\omega}{\tan\alpha}. \tag{2.13}$$

A combination of the couette and cone/plate geometry, like the Mooney-Ewart measuring system (shown in fig. 2.9), has the advantage of reducing end effects. The aim of this geometry is to achieve the same averaged shear rate within the annular and conic gap ($\dot{\gamma} = \dot{\gamma}_{\mathrm{cc}} = \dot{\gamma}_{\mathrm{cp}}$). The resulting construction requirements are given by equation 2.14 and 2.15 [41].

$$\alpha = (\delta_{\mathrm{cc}}^2 - 1)/(1 + \delta_{\mathrm{cc}}^2) \tag{2.14}$$

$$\delta_{\mathrm{cc}}^2 = (\alpha + 1)/(1 - \alpha) \tag{2.15}$$

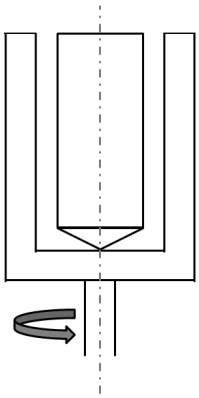

Figure 2.9: *Schematic illustration of a Mooney-Ewart geometry.*

2.3.2 Oscillating experiments

For oscillating rheological experiments rotationally symmetric shear cells like plate-plate or cone-plate geometries are used. During the experiment the upper plate with the shear area A is deflected by an angle φ by the shear force F while the lower plate is fixed. Two typical oscillating experiments are the amplitude sweep and the frequency sweep. During the amplitude sweep, the frequency of the oscillation is kept constant ($\omega = \text{const.}$) and the amplitude of the deformation is changed. In the case of a frequency sweep, the amplitude of the deformation is kept constant ($\gamma_A = \text{const.}$) and the angular frequency is variable. In both cases, the sample is strained periodically,

$$\gamma(t) = \gamma_A \cdot \sin\omega t \tag{2.16}$$

and the resulting shear stress is measured. The stress also follows a sine curve but it is shifted by a phase angle δ:

$$\tau(t) = \tau_A \cdot \sin(\omega t + \delta). \tag{2.17}$$

The quotient of $\tau(t)$ and $\gamma(t)$ defines the shear modulus of oscillating experiments.

$$G = \frac{\tau(t)}{\gamma(t)} \tag{2.18}$$

G^* describes the viscoelastic behavior of a sample and consists of the storage modulus G' (elastic part) and the loss modulus G'' (viscous part). The sum of these parts can be illustrated by a vector diagram (figure 2.10) and is desribed mathematically by equation 2.19.

$$|G^*| = \sqrt{(G')^2 + (G'')^2} \tag{2.19}$$

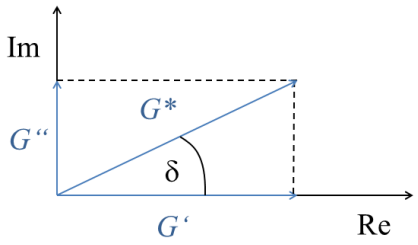

Figure 2.10: *Vector diagram of G^*.*

G' stands for the energy of deformation which is stored during the shearing process. This stored energy acts as the driving force during the process of recovering the initial structure and is not dissipated. G'' represents the energy which gets lost during the shearing process. This energy is used for the change of the structure of the sample or becomes transfered to the environment [41].

The ratio between the lost and stored deformation energy is called loss factor or damping factor and is defined as:

$$\tan \delta = G''/G'. \tag{2.20}$$

The loss factor yields information about the viscoelastic deformation behavior. The complex viscosity is defined by

$$\eta = \frac{\tau(t)}{\dot{\gamma}(t)}. \tag{2.21}$$

2.4 Characteristic parameters of ^{1}H NMR spectra

2.4.1 Chemical shift

The chemical shift depends strongly on the external magnetic field B_0, which induces circulations in the electron cloud of chemical bonds. Thus, a magnetic moment is created which is oriented in the opposite direction of the excitation field. As a consequence, the local magnetic field at the center of a proton is reduced. This is described by

$$B_{local} = B_0(1 - \sigma) \tag{2.22}$$

with the screening constant σ of the respective proton. The electronegativity of the adjacent atoms or groups have an influence on the chemical shift. In the case of electron-withdrawing groups like -Cl, -OH or -CN the electron density of the chemical bond is decreased. As a consequence the diamagnetic screening is decreased and the chemical shift of the affected proton is increased. Moreover, mesomeric effects can influence the chemical shift, too. Since no unsaturated or aromatic compounds are used, this effect is not discussed here.

Besides the intramolecular effects, the screening constant is also influenced by intermolecular effects. In the case of a close approach of solvent and solute molecule the electron cloud of a proton can be distorted by Van-der-Waals forces. This effect normally influences the chemical shift by up to 0.3 ppm [42]. Furthermore, an amphiphilic molecule, dissolved in a dielectric solvent, induces in its environment an electric field. This electric field changes the shielding of the protons of the molecule. In general, the influence of the electric field on the shielding is high for protons close to the polar group and decreases with larger distances. This effect exhibits an angular dependency and influences the chemical shift by up to ± 1 ppm [42]. Besides, there are other interactions such as hydrogen bonds between the polar head of the dissolved molecule and

the solvent which can influence the chemical shift by up to 0.5 ppm [42].

2.4.2 Line width

For the relaxation of the magnetization vector two relaxation processes exist. They are described by the spin-lattice relaxation time T_1 and the spin-spin relaxation time T_2. Normally, the influence of the spin-lattice relaxation on the line width is below 0.1 Hz [43]. Hence, the observed line width of liquid samples, like micellar solutions, is caused by spin-spin relaxation processes. The line width Δ, shown in figure 2.11, is defined by equation 2.23. The apparent relaxation rate $1/T_2^*$, derived from the measured line width, consists of the spin-spin relaxation rate $1/T_2$ and a term taking the magnetic field inhomogeneity ΔB_0 into account.

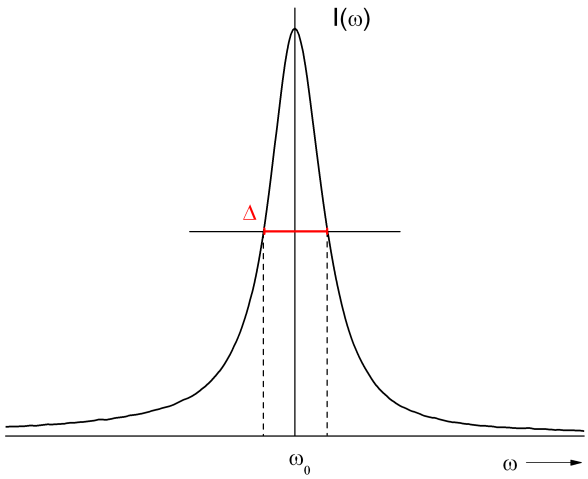

Figure 2.11: *Definition of the line width of a Lorentz signal.*

$$\Delta = \frac{2}{T_2^*} \tag{2.23}$$

$$\frac{1}{T_2^*} = \frac{\gamma \Delta B_0}{2} + \frac{1}{T_2} \tag{2.24}$$

2.4.3 Spin-spin coupling constant

The coupling between protons over three chemical bonds ($^3J_{HH}$) is called vicinal coupling. This coupling was described mathematically by Karplus [42, 44, 45]. He showed that the J values yield detailed information about the dihedral angle between the coupled protons (see fig. 2.12). The magnitude of the J coupling in Hz depends on the dihedral angle and has maximal values for angles of 0° and 180°. For a torsion angle close to 90° a minimum can be found.

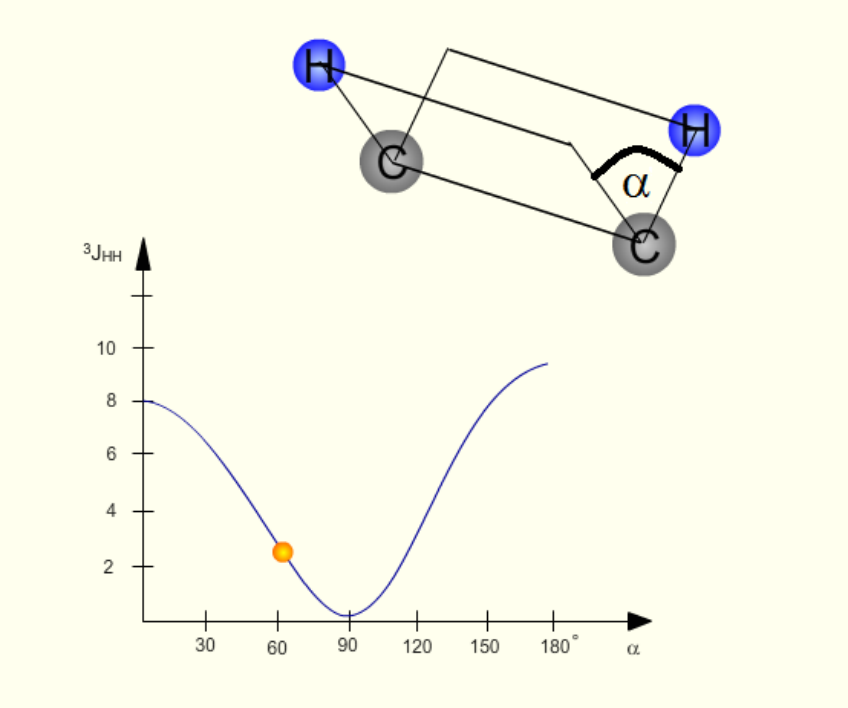

Figure 2.12: *Dependency of the $^3J_{HH}$ coupling constant in Hz on the dihedral angle between the coupled protons. This graphic is taken from [46].*

2.5 Scattering methods

Small-angle X-ray scattering (SAXS) experiments are commonly performed for the investigation of periodic distances of crystals, macromolecular solutions or colloidal dispersions [31, 47]. In partially ordered systems the SAXS experiments can deliver structural information for repeating distances up to 150 nm [47]. During the experiment, the X-ray beam is diffracted by the electrons of the sample. The reflected photons of the X-ray beam interfere. From the interference, which is described by the Bragg equation

$$2d\,\sin\theta = n\,\lambda, \tag{2.25}$$

the repeat distances of periodic structures can be determined. In equation 2.25 d is the repeat distance, θ the glancing angle, λ the wavelength and n any integer. The schematic Bragg reflection is shown in figure 2.13.

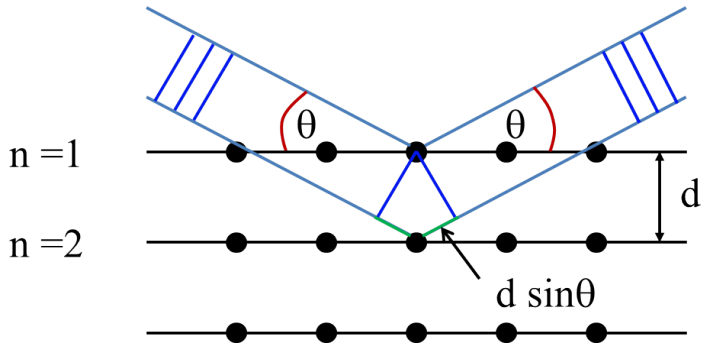

Figure 2.13: *Schematic illustration of Bragg reflection.*

The absolute value of the scattering vector $|Q|$ is defined by

$$Q = \frac{4\pi\sin\theta}{\lambda}. \tag{2.26}$$

To be able to investigate larger distances by small angle scattering techniques, small angle neutron scattering (SANS) can be used. In this case, neutrons are scattered by elastic collisions with the nuclei of the sample.

3 Investigation of aqueous surfactant solutions by ^{1}H NMR spectroscopy

In this chapter the binary surfactant system SDS/D_2O is studied in detail via proton NMR spectroscopy. The concentration dependent influence of the micellization and the micellar growth on the chemical shift, line width and splitting of the α-CH_2 and CH_3 groups of the alkyl chain are investigated. The splittings of the two groups show a non expected behavior. In order to find out if this unusual behavior is typical only for the aqueous SDS system, the splittings of a second aqueous surfactant system (CTAB/D_2O) are investigated.

3.1 System SDS/D_2O

3.1.1 Phase diagram of the SDS/water system

A detailed phase diagram of SDS in H_2O was determined by Kékicheff et al. in the late 80s via DSC measurements [48]. The cmc of the SDS/D_2O system was reported as 7.6 mM [34] which corresponds to 0.2 wt. % SDS. Figure 3.1 shows the phase diagram according to [48]. The part of the diagram, which was investigated during my research via ^{1}H NMR spectroscopy in the temperature range from 30 °C to 55 °C, is marked.

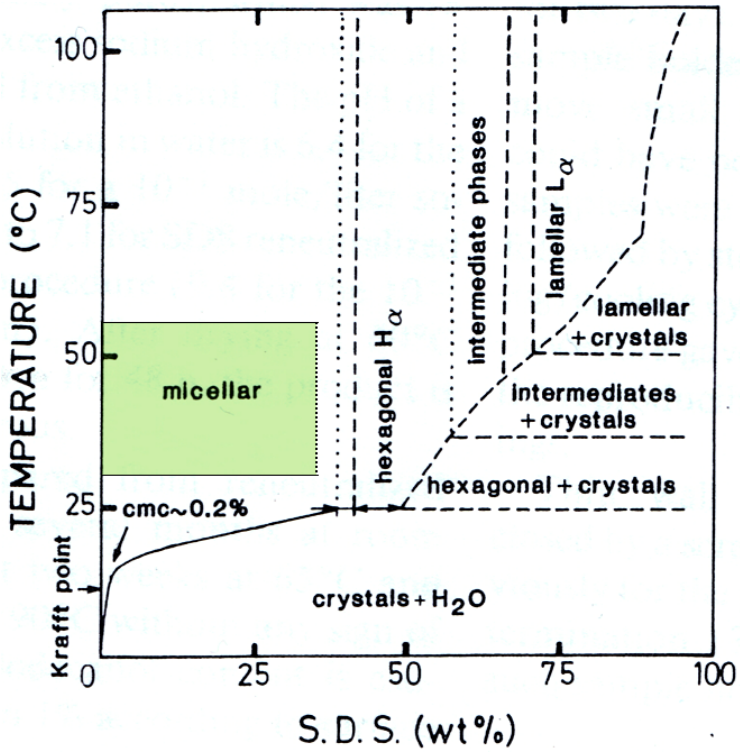

Figure 3.1: *Phase diagram of the SDS/water system taken from [48]. The investigated concentration and temperature range is highlighted. The dotted line, which is added at 35 wt. %, represents the concentration at which the first hexagonal signal could be obtained by ^2H NMR spectroscopy for the SDS/D_2O system.*

For the investigated temperatures, the micellar phase exists, according to the phase diagram, from 0 to 39.4 wt. %. With increasing concentration of SDS transitions into a two phase region, which exists from 39.4 to 42.3 wt. %

consisting of a micellar and a hexagonal phase, and into a hexagonal phase, above 42.3 wt. % SDS, follow. The remaining phases and phase transitions at higher SDS concentrations were not investigated.

Due to the known influence of the exchange of H_2O by D_2O on surfactant solutions, as well as possible contaminations of the chemicals used, small changes of the phase boundaries are expected. Therefore, the samples above 20 wt. % were investigated by deuterium NMR in order to determine the phase transition concentrations. The deuterium NMR spectra obtained are shown in figure 3.2. Below 35 wt. % SDS the ^2H NMR spectra show for all investigated samples an isotropic signal which is characteristic for the micellar phase. At 35 wt. % SDS a doublet, which is characteristic for the hexagonal phase, was detected in addition to the isotropic singlet.

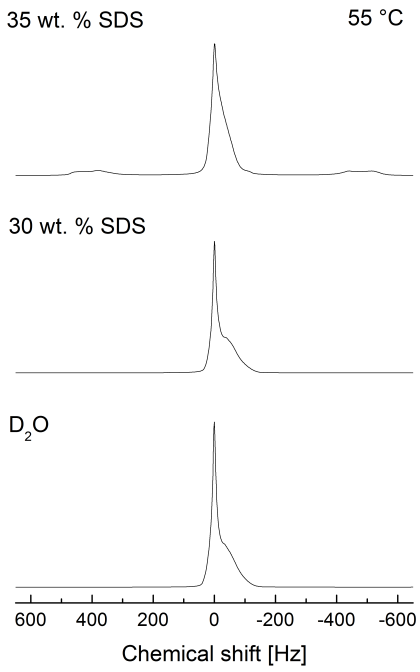

Figure 3.2: *Deuterium NMR spectra of D_2O, 30 wt. % and 35 wt. % SDS at 55 °C.*

If the molar ratio of SDS to water at the transition concentration to the two phase region is equal for H_2O and D_2O, the transition concentration expected

for the system with D_2O is 36.9 wt. %. Experimentally, the transition was found between 30 and 35 wt. % SDS. The upper concentration of this range is shown in the phase diagram as a dotted line at 35 wt. % SDS.

3.1.2 Peak assignment of the ^{1}H NMR spectrum of a micellar sample

Figure 3.3 shows a ^{1}H NMR spectrum of a micellar sample (3 wt. % SDS in D_2O at 30 °C) with peak assignment. The proton NMR spectra of SDS exhibit four signals, which are assigned to the α-CH_2, β-CH_2, CH_3 group and to the rest of the alkyl chain [49, 50]. In the micellar region, where the SDS molecules are very agile, the shape of the α-CH_2 signal is a symmetric triplet while the CH_3 signal is slightly asymmetric. The β-CH_2 group can be seen as a multiplett. The other CH_2 groups of the alkyl chain have nearly the same chemical shift. As a consequence, only one additional peak can be detected.

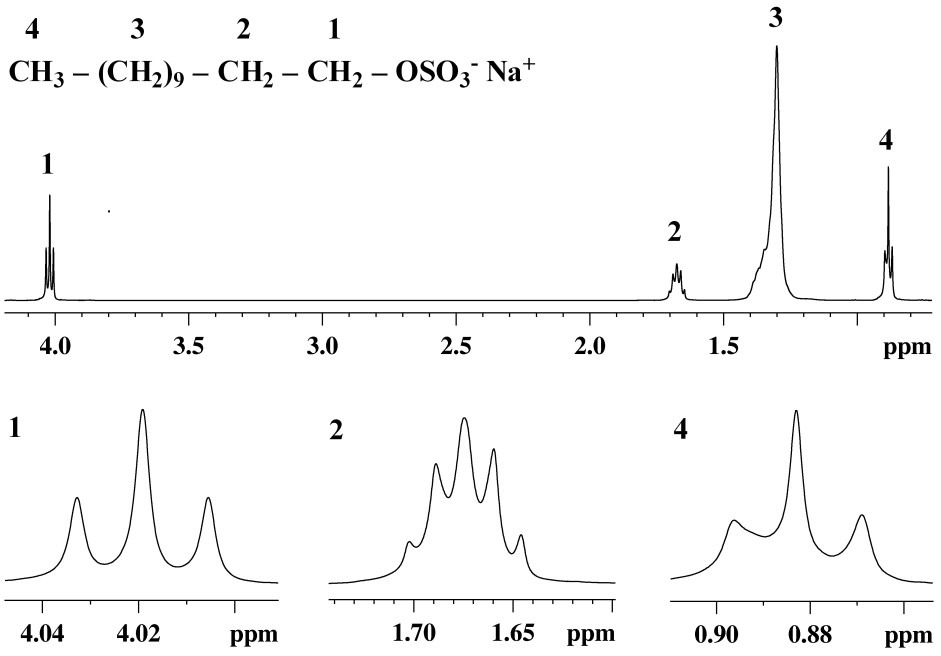

Figure 3.3: *^1H NMR spectrum of 3 wt. % SDS at 30 °C with peak assignment.*

3.1.3 Chemical shift study

Figure 3.4 shows the α-CH_2 and CH_3 signals of SDS at different concentrations at 30 °C. The concentration dependent shift of the signals is conspicuous and can be used for the determination of the cmc [4, 5].

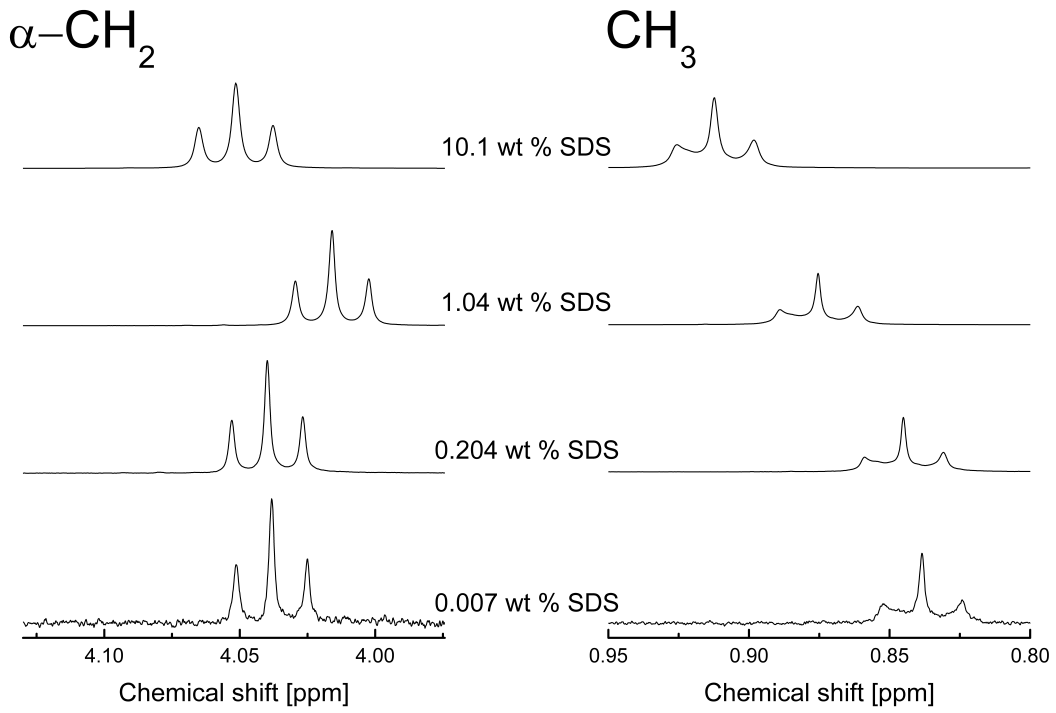

Figure 3.4: *Concentration dependent chemical shift of the α-CH_2 and CH_3 signal of 3 wt. % SDS at 30 °C.*

The behavior of the chemical shift of the SDS/D_2O system was already investigated by Kumar et. al [5] and Barhoum et. al [6]. They subtracted the chemical shift of the methyl group from the chemical shift of the α-CH_2 group ($\delta(\alpha\text{-}CH_2) - \delta(CH_3)$) and plotted the differences versus the concentration. From the publication of Kumar et. al [5], the data of the chemical shift differences were read out manually and are shown in figure 3.5 in addition to the ones obtained for the investigated samples. For the determination of the difference, both signals were fitted by three Lorentzian lines. The chemical shifts of the centered fitted Lorentzian lines were used for the calculation of

the chemical shift difference. It can be seen that the literature values could be reproduced well. The small deviations from the literature are due to the different temperatures and the manual read out process of the literature data.

Below the cmc, the chemical shifts of the individual signals do not vary. Hence, the difference of the chemical shifts is nearly constant. After the micellization the chemical environment of the surfactant molecules changes. For the SDS/D_2O system the change leads to a decrease of the difference of the α-CH_2- and CH_3-signal. Based on this change, the cmc of the SDS/D_2O system can be determined. The disadvantage of this way of data presentation is, that the illustration provides no information about the changes of the chemical shifts of the individual α-CH_2- and CH_3-signals.

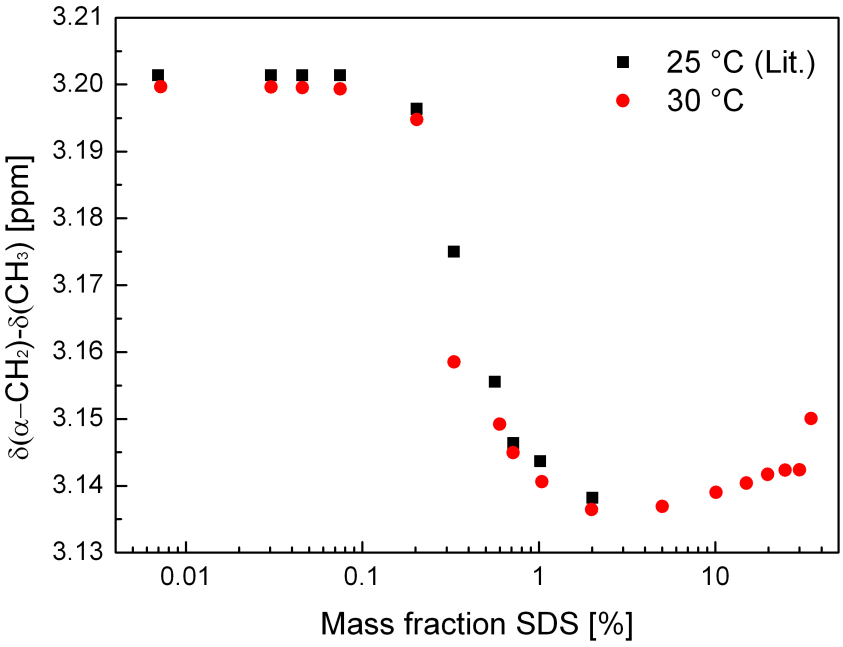

Figure 3.5: *Concentration dependent difference* $(\delta(\alpha{-}CH_2) - \delta(CH_3))$ *of the chemical shift of the* α*-*CH_2 *and* CH_3 *signals. The black symbols are literature values taken from [5].*

To get more detailed information, the relative change of the chemical shifts $\Delta\delta$ of each peak must be considered. To calculate $\Delta\delta$ the initial chemical shift of the signals at 0.007 wt. % is subtracted from the chemical shift at the particular concentration. The results are shown in figure 3.6.

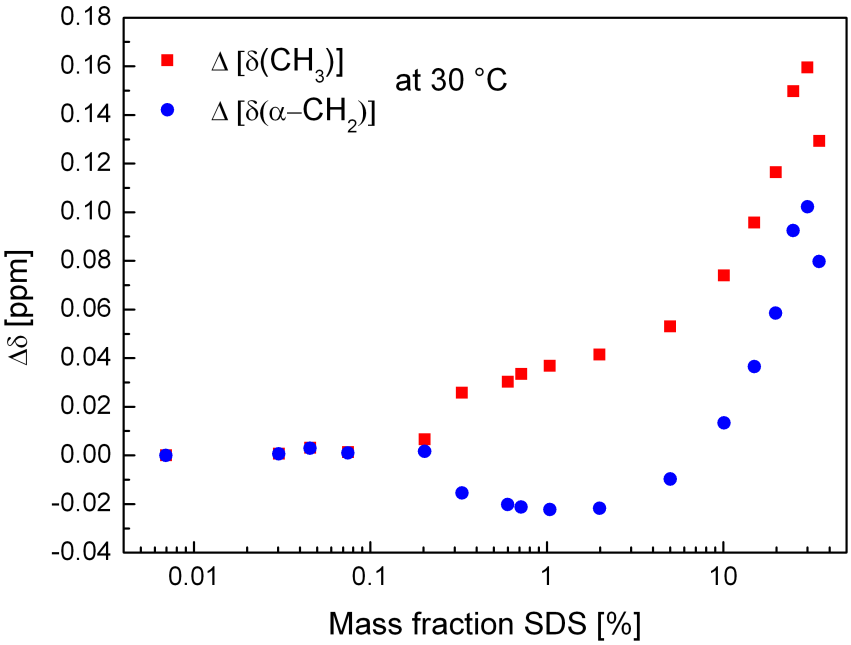

Figure 3.6: *Concentration dependent change of the relative chemical shift. $\Delta\delta$ is calculated by subtracting the chemical shift of the first concentration from the remaining concentrations for the α-CH_2 and the CH_3 signals.*

From 0.007 wt. % SDS to the cmc (0.2 wt. % SDS), nearly no change of $\Delta\delta$ is observed. Above the cmc up to 1.04 wt. %, the α-CH_2 signal is shifted to lower and the CH_3 signal to higher ppm. In other words, the change of the chemical shift of the two signals proceeds in opposite directions. At 1.04 wt. %, there is a shallow minimum of $\Delta\delta$ of the α-CH_2 signal. From 1.99 to 30 wt. % SDS, both signals are shifted in the same direction and the chemical shifts increase strongly. At 35 wt. % both signals are shifted back to lower ppm and the values of $\Delta\delta$ decrease.

Starting at the cmc micelles are formed. This leads to a change in the

chemical environment of the molecules in the micelles. In the case of the CH_3 groups the chemical environment changes from hydrophilic to hydrophobic. As a consequence the chemical shift of the surfactants changes. About the different direction of the change of the chemical shift of the α-CH_2 and CH_3 signal from the cmc to 1.04 wt. % no information could be found in the literature.

The minimum of $\Delta\delta$ of α-CH_2 between 1 and 2 wt. % SDS correlates to the known transition of the micellar shape from spherical to quasi-spherical or ellipsoidal. According to the literature this transition takes place between 1.3 and 2.1 wt. % SDS [49] (determined via spin-spin relaxation rates).

Up to now, no information could be found in the literature for the decrease of $\Delta\delta$ of the α-CH_2 groups from the cmc to the minimum. This decrease as well as the increase above 2 wt. % SDS probably result from conformational changes at the α-CH_2 groups (the conformational changes will be discussed in detail in chapter 3.1.5).

Between 30 and 35 wt. % SDS a phase transition from the isotropic to a two phase region consisting of a micellar and a hexagonal phase takes place. For the sample located in the two phase region, a decrease of $\Delta\delta$ of both groups was observed.

3.1.4 Line width analysis

Another characteristic property of the NMR spectra is the line width at half height, which gives information about the relaxation times of the molecules. The NMR signals of the alkyl chain and α-CH_2 groups at different concentrations are shown in figure 3.7. The line width of the center peak of the α-CH_2 triplet is obtained by fitting it by three Lorentzian lines.

Figure 3.8 shows the line width of the alkyl chain (C_3-C_{11}) and the line width of the center peak of the α-CH_2 signal at 30 °C. Below the cmc the line width of the alkyl chain is constant. With increasing concentration of SDS,

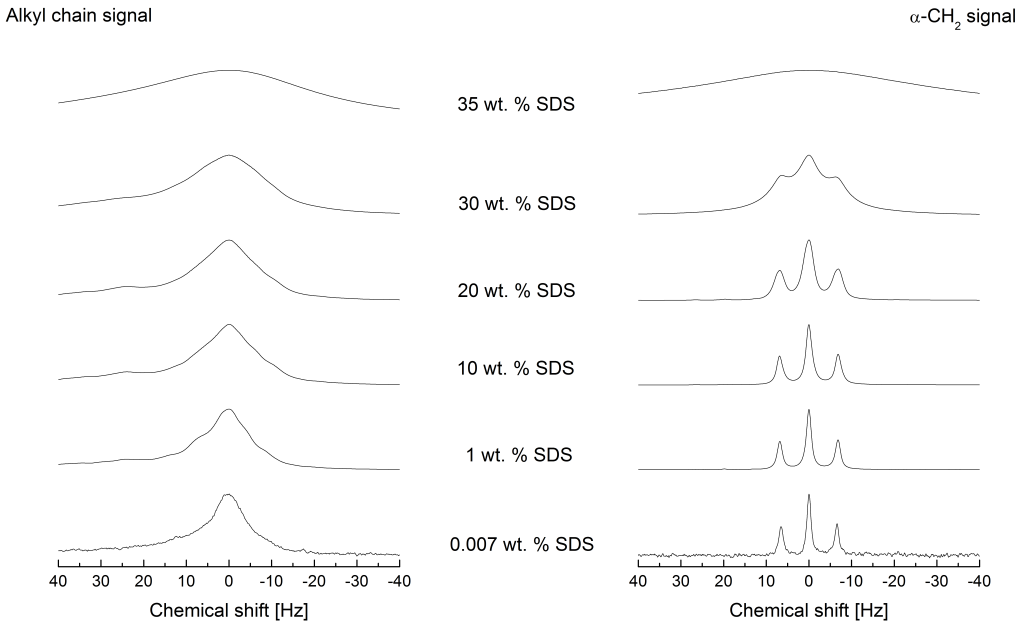

Figure 3.7: *Line broadening of the alkyl chain and α-CH_2 signals with increasing surfactant concentration at 30°C.*

starting at the cmc, the line width increases steadily up to 20 wt. %. From there it increases strongly.

The line width of the center signal of the α-CH_2 signal shows only a slight increase in its value from 0.007 to 20 wt. % SDS. Above 20 wt. % the line width increases strongly, too. At 35 wt. % SDS the triplet is broadened so much that only a singlet is detected. The center peak cannot be fitted exactly. For that reason the data point is missing.

Since the alkyl chain signal is composed of nine hydrocarbon groups, which have quite similar but still different chemical shifts, the signal of the alkyl chain is a superposition of the single signals. Hence, its line width is broader than the line width of the α-CH_2 signal.

The moderate increase of the line widths from the cmc to 20 wt. % might be caused by micellar growth. For large micelles, whose shape differs from spherical, the free rotation is reduced leading to a line broadening. The strong line broadening starting at 25 wt. % SDS is typical for concentrations close

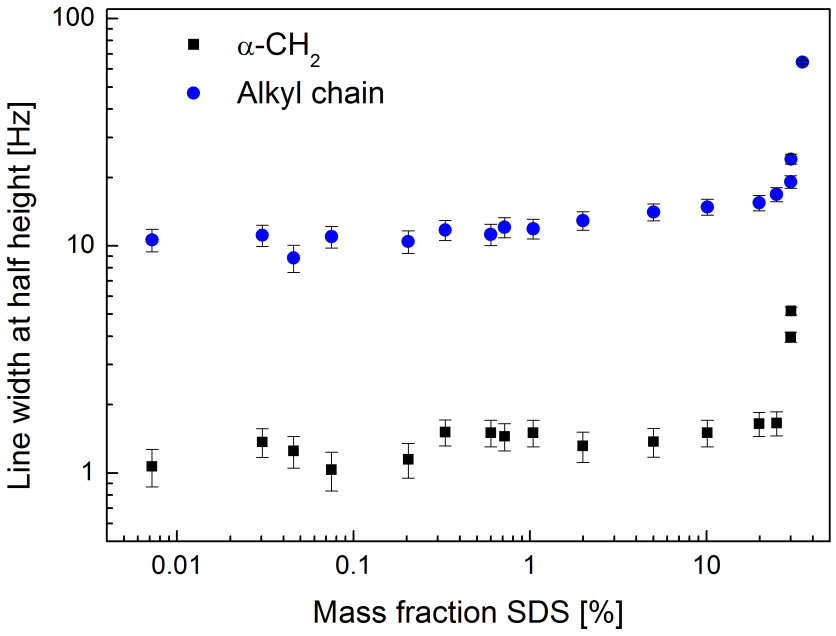

Figure 3.8: *Line width of the alkyl chain and the center peak of the α-CH_2 signal at 30 °C.*

and at phase transitions [7].

3.1.5 Investigation of the splittings of the α-CH_2- and CH_3-signal

Figure 3.9 shows the splittings of the α-CH_2 group at different temperatures versus the mass fraction of SDS. To obtain the value of the splittings the triplet of α_{SDS} is fitted by three Lorentzian lines. Half the distance between the positions of the fitted outer peaks represents the value of the splitting in Hz.

For the interpretation of the splittings it must be considered, that the measured values are weighted and averaged values over the splittings of each α-CH_2 or CH_3 group in the volume contributing to the proton NMR signal. The observed splittings of each group can be approximately calculated by

$$J = x_f \cdot J_f + x_m \cdot J_m \tag{3.1}$$

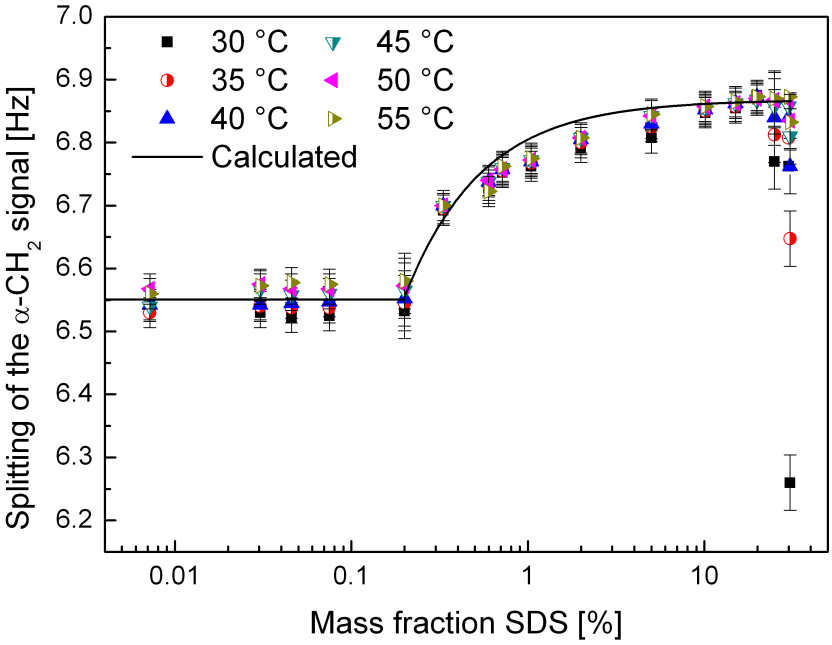

Figure 3.9: *Magnitude of the splitting of the α-CH_2 signal plotted versus the mass fraction of SDS.*

where x_f is the mole fraction of the free surfactant molecules and x_m the mole fraction of the surfactant molecules located in the micelles ($x_m = 1 - x_f$). J_f is taken as the average of the splittings below the cmc and J_m is obtained by extrapolating the splitting to 100 wt. % SDS. The calculated values of the splitting are shown as a solid line in figure 3.9. The deviations from the calculated curve probably result from the influence of changes of the micellar shape on the value of the splitting, which were not considered by the calculation.

At concentrations below the cmc x_m will be zero. Hence, the plotted values of the splittings are an average over all conformations of free surfactant molecules in water. At these concentrations, most of the surfactants will be present in a partly coiled state to reduce the water-hydrocarbon contact [51]. Furthermore entropy effects should prefer the coiled conformation instead of an all trans conformation [51]. Therefore, the molecules below the cmc will favor gauche

conformations.

At concentrations higher than the cmc, the value of the splitting will result from a weighted average of the conformations of the α-CH_2 group of free surfactants and surfactants which are located in micelles. Within the micelles, the molecules get stretched. Hence, trans conformations of the chains become more probable than for the free molecules. This also leads to a higher probability of trans positions of vicinal protons. According to Karplus [44, 45], the trans positions of protons yield higher splitting values than gauche positions (see chapter 2.4.3). Therefore an increase of the splitting at the cmc is expected, which is indeed observed.

At 20 wt. % SDS the value of the splitting reaches its maximal value for the micellar region. At this concentration, approximately 99 % of the surfactant molecules are present in the micelles. At concentrations of 25 and 30 wt. % SDS there is a distinct temperature dependence of the coupling constant, becoming more pronounced with increasing concentration.

Figure 3.10 shows the temperature dependency of the α-CH_2 signals of 30 wt. % SDS at 30, 40 and 55 °C. The measured triplet is shown in black, the fit in cyan and the individual Lorentz peaks of the fit in green, red and blue. It can be seen that the fit accuracy decreases with increasing temperature.

At 35 wt. % SDS, the sample is already in the two phase region consisting of a micellar and a hexagonal fraction. The observed α-CH_2 signal is broadened so much that the splitting is not resolved, and a broad singlet is detected.

In figure 3.11 the splitting of the CH_3 group is shown. To determine the value of the splitting, the asymmetric triplet (see figure 3.3) is fitted by three Lorentzian lines. Its value is defined by the distance between the center peak and the peak at lower frequency.

It can be seen that the splitting is nearly constant up to 20 wt. % SDS. The larger errors at 0.007 wt. % SDS result from a reduced scan number leading

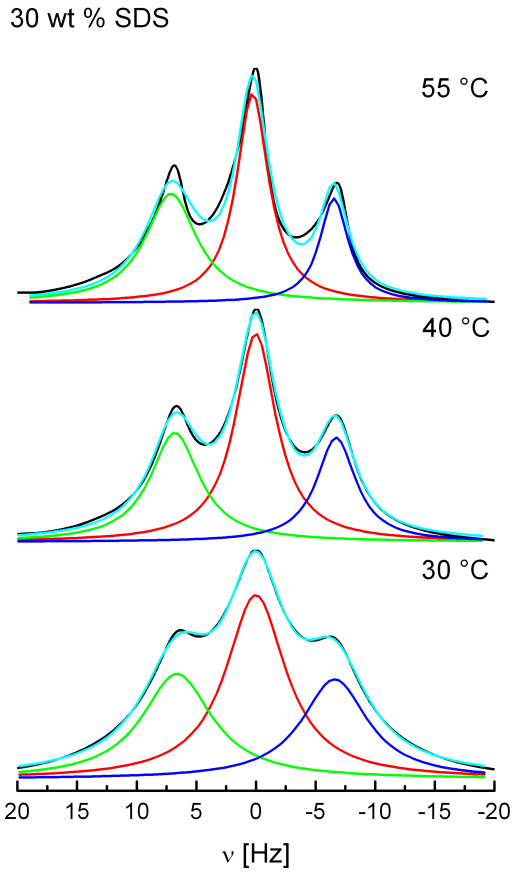

Figure 3.10: *Temperature dependance of the α-CH_2 signal of 30 wt. % SDS at 30, 40 and 55 °C.*

to more noise. Starting at 25 wt. % SDS a temperature dependence of the splitting values can be seen. For 35 wt. % SDS only a broad signal without fine structure is detected.

For the temperature dependent reduction of the splittings of the α-CH_2 and CH_3 group there is up to now no clear explanation. If the change of the splitting would be caused only by conformational changes, the structure of the micellar aggregates would have to undergo a conspicuous change. This change can not be assumed since the micelles are ellipsoidal at circa 2 wt. % and grow with increasing concentration probably to rodlike aggregates. The combination of these aggregates to a hexagonal phase should cause nearly no conformational changes and therefore no change of the splitting. Furthermore, the mentioned

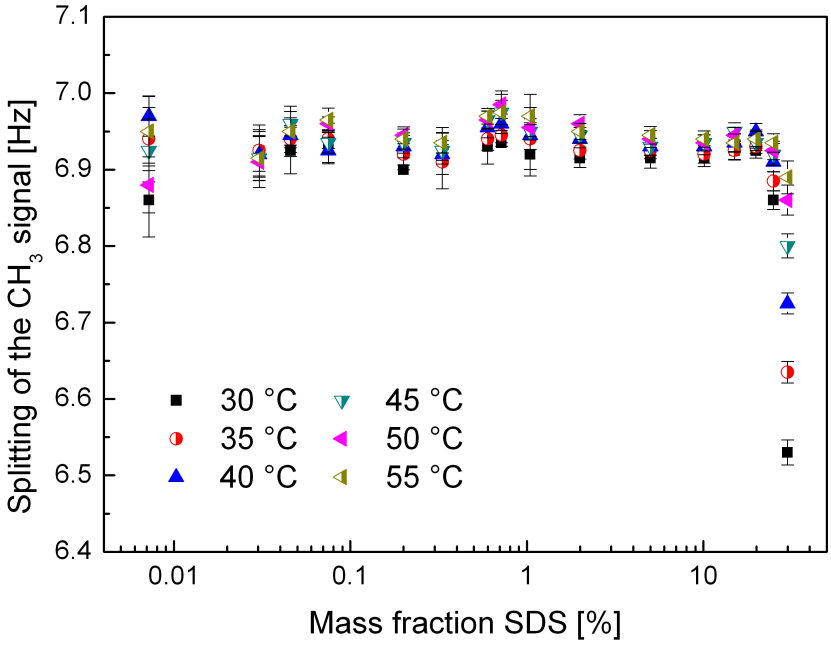

Figure 3.11: *Magnitude of the left splitting of the CH_3 signal plotted versus the mass fraction of SDS.*

changes of the micellar shape should not affect splitting.

A temperature dependency of the $^1J(^{13}C\ ^1H)$ coupling constant was already observed in the late 1970's for plastic phases of oriented solids like *t*-butyl chloride. This compound was investigated in two different solid states and in the liquid phase. It was shown that the decrease of the coupling constant $^1J(^{13}C\ ^1H)$ with increasing temperature is an artifact resulting from a rapid proton spin exchange within the solid phases [52].

Since the change of the splitting is temperature dependent, it could be correlated to the relaxation time T_2, which becomes shorter for decreasing temperatures. In the case of an increased order of the aggregates close to the phase transition, the dipolar coupling could be increased. The influence of this coupling could be decreased by averaging it at higher motions, which is the case at higher temperatures. If the values of the dipolar couplings have the opposite sign than the values of the J coupling constant a decrease of the

observed splitting could be explained.

To check whether the temperature dependent change of the coupling constant is only a phenomenon of the SDS/D_2O system the CTAB/D_2O system will be investigated, too.

3.2 System CTAB/D_2O

Figure 3.12 shows the phase diagram of aqueous CTAB according to Clawson, Holland and Alam [53]. They investigated the concentration range from 16 to 36 wt. % CTAB in H_2O via NMR spectroscopy with spin-1 nuclei (^2H and ^{14}N). In the concentration range from 0 to 16 wt. % the system consists of a micellar isotropic phase for the temperatures shown [54]. I, N, and H denote the isotropic, nematic and hexagonal phases. The dashed lines of the boundaries of the N/H and I/N/H regions are not well defined. The crosses represent experimentally determined values from reference [53]. The cmc of the CTAB/D_2O system is 0.82 mM [34] corresponding to 0.027 wt. % CTAB. The transition from spherical to rod-like aggregates was found by Auvray via X-ray scattering to take place at 25 °C at concentrations below 12 wt. % CTAB for the CTAB/H_2O System [54]. The sequence of structures found by Clawson et al. starts with spherical micelles which change to rodlike micelles at circa 10 wt. % CTAB. Then a nematic liquid crystalline phase (circa 25 wt. % CTAB) and a hexagonal LC phase ($>$ 30 wt. % CTAB) follow. Again, H_2O is replaced by D_2O in the studies presented here.

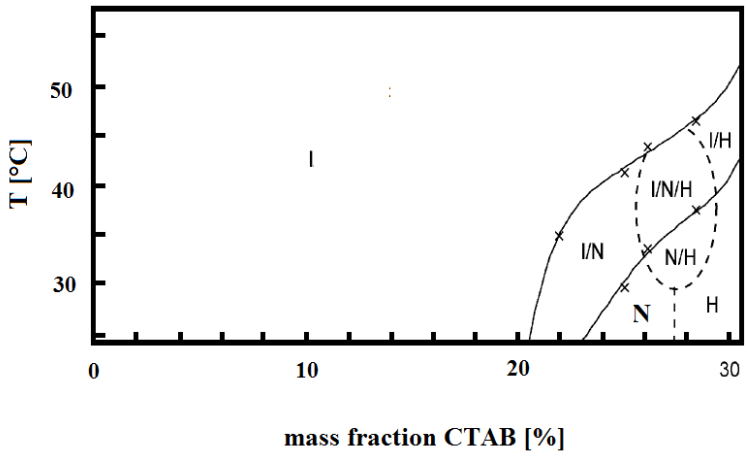

Figure 3.12: *Phase diagram of the binary system CTAB/D_2O. The concentration range from 16 to circa 30.5 wt. % CTAB is taken and complemented according to reference [53].*

A typical micellar ^{1}H NMR spectrum (5 wt. % CTAB at 30 °C) with peak assignment is shown in figure 3.13. It can be differentiated between the CH_3 signals of the headgroup (**1**), α-CH_2 (**2**), β-CH_2 (**3**), a short part of the chain (**4**), the major part of the chain (**5**) and the end CH_3 group (**6**) of the surfactant [55]. The form of the α-CH_2 signal is traditionally attributed to the ^{14}N-^{1}H coupling in addition to the ^{1}H-^{1}H coupling to the β-CH_2 [55]. Another possible explanation has been presented by Cheng. He makes the restricted rotation around the C_α–C_β axis next to the polar head group responsible for the form of the α-CH_2 signal. From this a chemical nonequivalence of the two protons results [56].

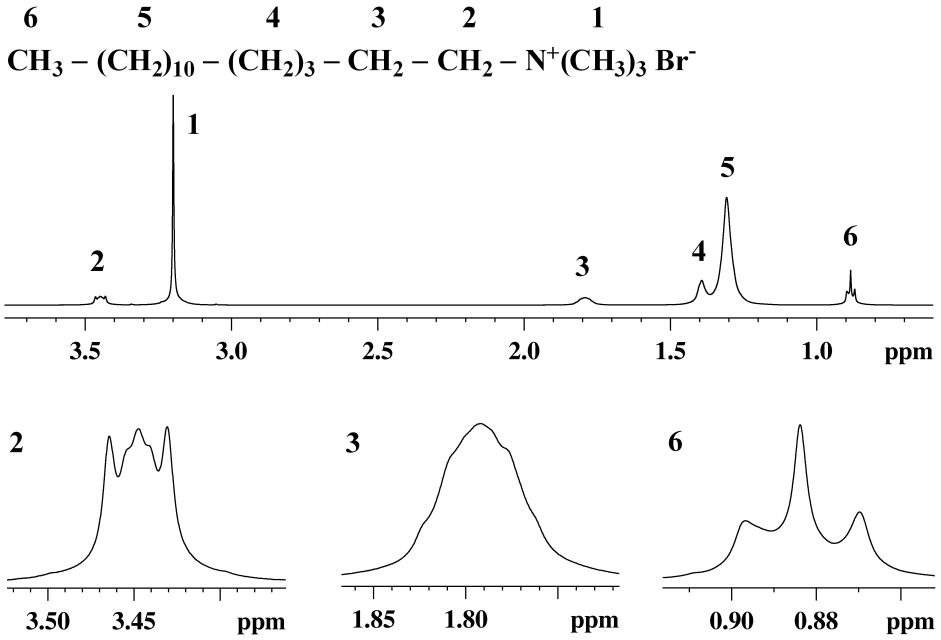

Figure 3.13: *^{1}H NMR spectrum of 5 wt. % CTAB at 30 °C with peak assignment.*

Figure 3.14 shows the change of the chemical shift of the α-CH_2 and CH_3 signal as a function of concentration. For the calculation of the relative change, the chemical shift of the respective signal at 0.003 wt. % was substracted from the one of the other concentrations. Below the cmc (0.027 wt. %) the chemical

shift is nearly constant. Above the cmc the chemical shifts of both groups increase until they reach a nearly constant value. For the CH_3 group this occurs already at a concentration of 0.2 wt. % CTAB. This behavior implies that there is no or only a little change in the chemical environment of the CH_3 group from 0.2 to 5 wt. %. The change of the chemical shift of the α-CH_2 group increases up to 2 wt. % and remains constant up to 5 wt. %.

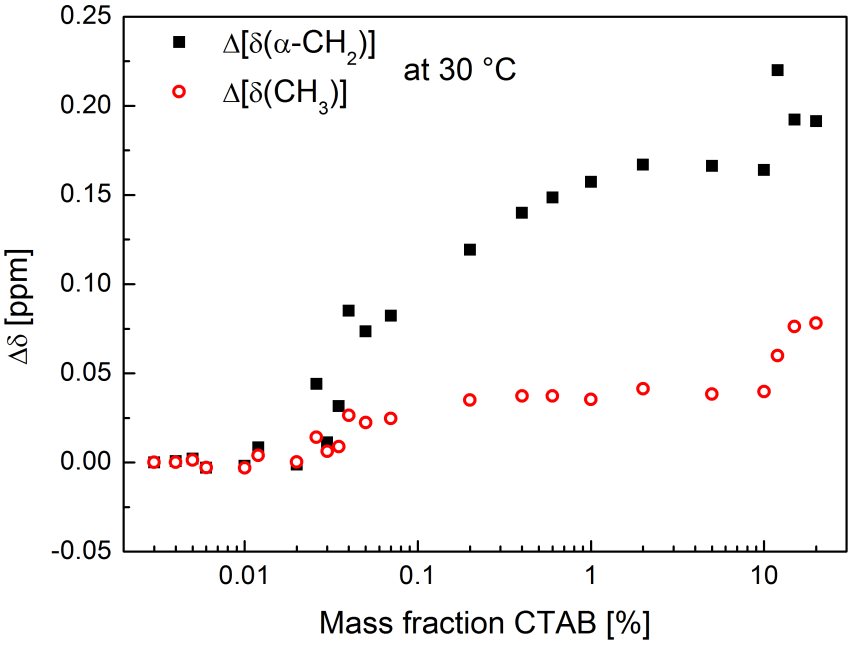

Figure 3.14: *Relative change of the chemical shift of the α-CH_2 and CH_3 group of CTAB at 30 °C.*

The values of $\Delta\delta$ of the α-CH_2 group at concentrations higher than 10 wt. % CTAB contain a large error. From 10 to 12 wt. % CTAB a transition of the micellar shape from spherical to rod-like takes place leading to an increase of $\Delta\delta$. The transition has a strong influence on the viscosity of the samples. The flow behavior of the samples up to 10 wt. % CTAB is comparable with water while the samples at concentrations of 12, 15 and 20 wt. % CTAB are gel-like. This change leads to a line broadening of the proton NMR signals. Starting at 12 wt. % the α-CH_2 and CH_3 signals at 30 °C can only be detected as broad

singlets. Figure 3.15 shows the concentration dependent change of the line shape of the CH_3 signals.

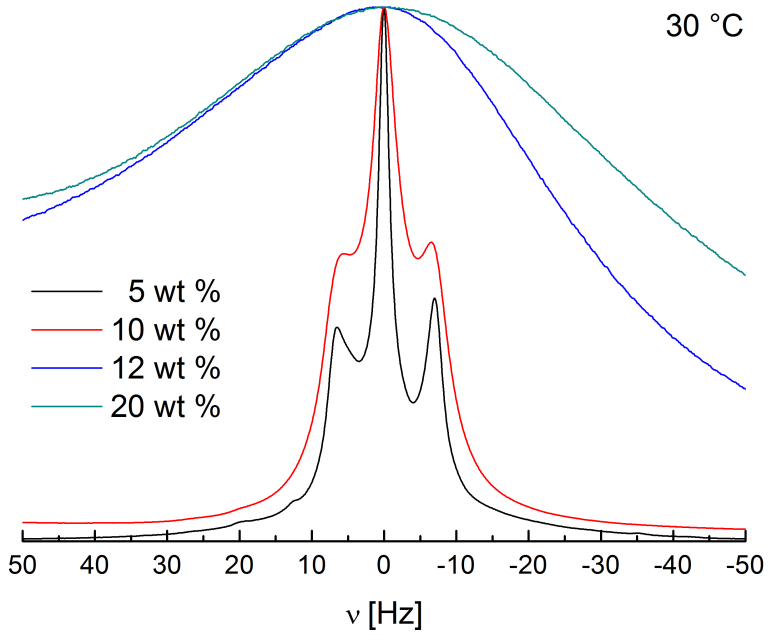

Figure 3.15: *CH_3 signal of CTAB at different concentrations at 30 °C.*

Figure 3.16 shows the difference of the chemical shift of the α-CH_2 and CH_3 signal for different CTAB concentrations. Below the cmc the difference is nearly constant resulting from the constant chemical shifts of the signals. Above the cmc up to 5 wt. % CTAB the value of the difference increases. The increase is due to the increasing chemical shift of the α-CH_2 signal and the nearly constant shift of the CH_3 signal from 0.2 to 5 wt. % CTAB. Above 10 wt. % CTAB the chemical shift of the methyl group increases more strongly than the one of the α-CH_2 leading to a decreasing difference of the chemical shifts.

Figure 3.17 shows the line width at half height of the CH_3 groups located on the ammonium of the surfactant, the alkyl chain as well as the CH_3 group at the end of the alkyl chain. The line widths were obtained in analogy to the

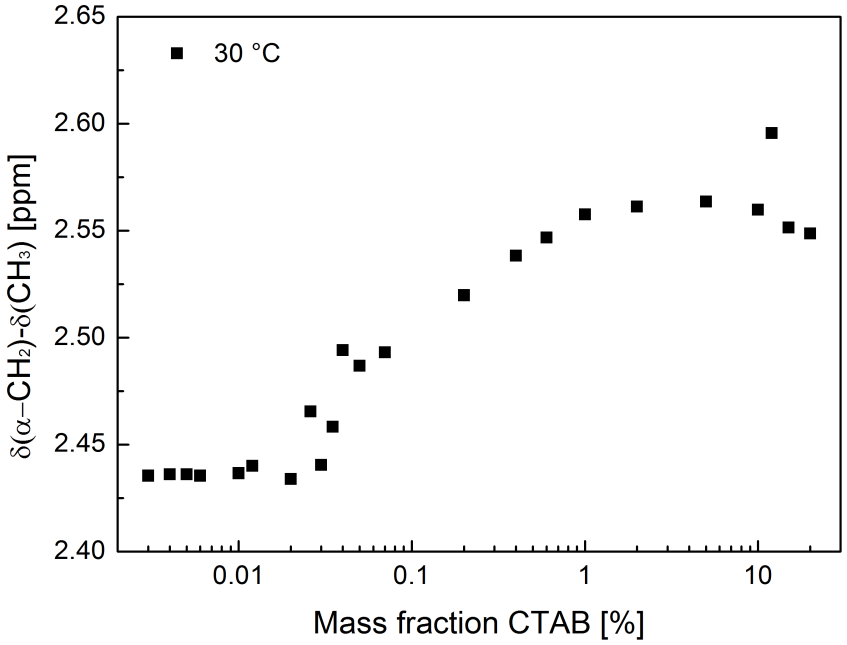

Figure 3.16: *Difference of the α-CH_2 and CH_3 groups of CTAB at 30 °C.*

ones of the SDS/D_2O system. Below the cmc, especially below 0.02 wt. %, the fit of the lineshape is very inaccurate due to the bad signal-to-noise ratio which results from the low concentration of surfactant. For that reason the line width below the cmc is not representative.

Starting at the cmc the line width of the alkyl chain signals increases slightly up to 10 wt. % CTAB. The increase of the linewidth could result from the reduced mobility of the alkyl chains due to the growth of the micelles. Above 10 wt. % the signals become so broad, that they overlap and cannot be fitted. Hence, their linewidths cannot be distinguished.

The line width of the methyl group of the alkyl chain shows the same behavior. Only the signal of the methyl groups located at the ammonium can be fitted at higher concentrations, since they deliver a singlet. Its line width increases slightly up to 2 wt. % CTAB, a little more from 2 wt. % to 10 wt. % and strongly from 12 wt. % to 20 wt. %. The strong increase is due to the increased viscosity of the samples leading to a decreased motion of the aggregates.

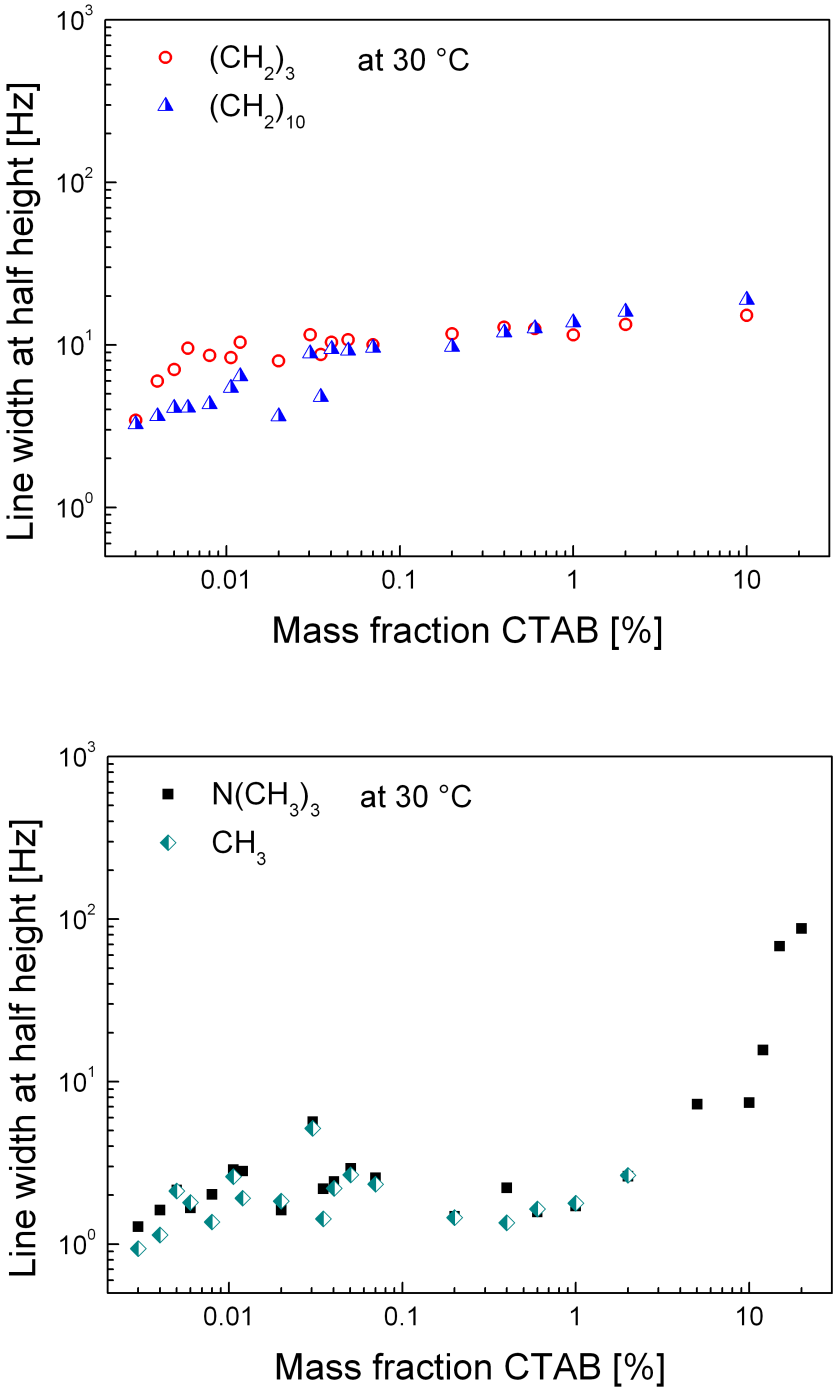

Figure 3.17: *Line width of the alkyl chain signals (top) and the methyl group signals (bottom) at 30°C.*

Additionally to the chemical shift and line width the splittings of the CH_3 signal were investigated, too. Due to the complex shape of the α-CH_2 signal its splittings could not be distinguished. The values of the splittings of the CH_3 signal were determined in the same way as the ones of the SDS/D_2O system. The results are shown in figure 3.18. Below the cmc, the calculation of the splitting is influenced strongly by the bad accuracy of the fit. As a consequence the splitting below the cmc is quite inaccurate.

From the cmc to 2 wt. % CTAB the splitting could be determined with good accuracy. Its value is, like the splitting of the CH_3 signal of SDS, constant over a wide concentration range.

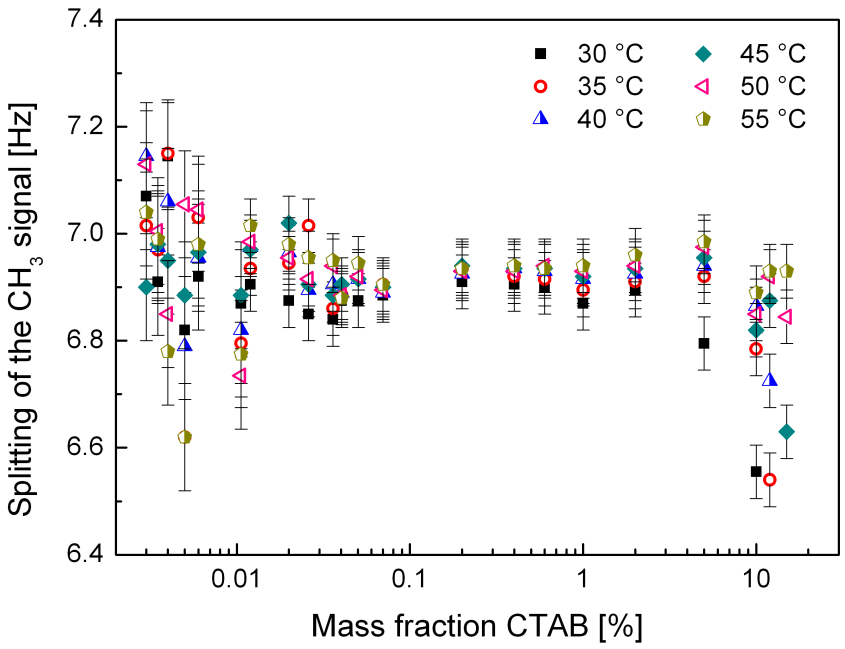

Figure 3.18: *Splitting of the CH_3 signal of CTAB at different temperatures.*

Starting at 5 wt. % CTAB a temperature dependence of the splitting can be seen. To enhance the visibility of the temperature dependency the splittings of the concentrations of 5, 10, 12 and 15 wt. % CTAB are plotted versus the temperature in figure 3.19. The influence of the temperature increases

with increasing concentration. The value of the splitting of 5 wt. % at 30 °C is slightly lower than the ones of the other temperatures. At 10 wt. % a clear deviation from the splittings at other temperatures can be seen. At concentrations higher than 10 wt. % the splitting could not be calculated due to the resolution of the signal (see fig. 3.15). The same behavior occurs for the splitting at 35 °C. Its value decreases tendentially from 5 to 10 wt. % and more distinctly from 10 to 12 wt. % until it cannot be distinguished due to the bad resolution of the signal at 15 wt. %. The splitting at 40 °C shows an analogous behavior. Only the splittings at 55 °C seem to be temperature independent. At 20 wt. % CTAB no fine structure could be detected for all temperatures.

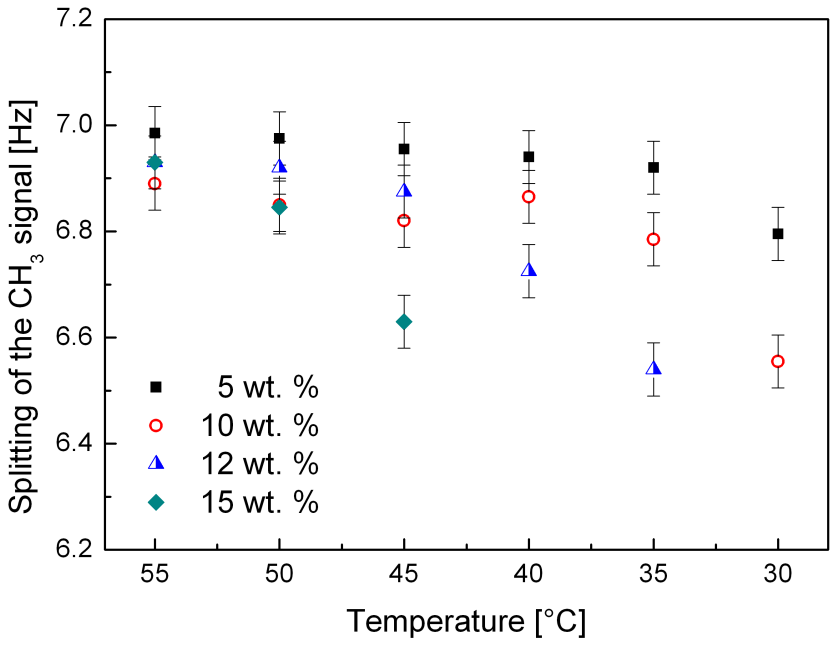

Figure 3.19: *Splitting of CH_3 signal of CTAB versus the temperature for concentrations of 5, 10, 12 and 15 wt. % CTAB.*

It is very unlikely that the temperature dependent change of the values of the splitting results from conformational changes of the methyl groups due to the change of the micellar shape from spherical to rodlike. There is a strong

increase in viscosity leading to a decreased relaxation time T_2. The decreased motion of the micellar aggregates leads again to less effective averaging of the dipolar coupling. By increasing the temperature, the influence of the dipolar coupling decreases and the observed splitting, too.

The investigation of the CTAB/D_2O system shows, that the transition of the micellar shape from spherical to rod-like has a strong influence on the proton NMR spectra. The resolution of the spectra (fig. 3.15), for example, decreases. Furthermore there occurs a change of the relative chemical shift (fig. 3.14) and an increase of the line width at half height of the CH_3 groups (fig. 3.17). Due to the broadening of the NMR signals above 12 wt. %, it is not reasonable to investigate further samples at higher CTAB concentrations (>20 wt. %) via proton NMR spectroscopy. Again, a temperature dependency of the splittiing of CH_3 group was found.

3.3 Conclusions

In this chapter the influence of the micellization and the micellar growth on the chemical shift, on the splittings of α-CH_2 and CH_3 groups of the alkyl chain, and on the line width were studied by proton NMR spectroscopy for the SDS/D_2O and CTAB/D_2O systems.

For the CTAB/D_2O system the values of the change of the chemical shift $\Delta\delta$ of α-CH_2 and CH_3 signals increased from the cmc with increasing concentration. In the case of the SDS/D_2O system, the value of $\Delta\delta$ of the CH_3 group increased steadily, starting from the cmc, while $\Delta\delta$ of the α-CH_2 group decreased. At 1.04 wt. % $\Delta\delta$ of the α-CH_2 group had a minimum. From 1.04 wt. %, $\Delta\delta$ increased steadily with increasing surfactant concentration.

The increase of the chemical shift of the CH_3 group results from the change of the chemical environment. The change of the chemical shift of the α-CH_2 group probably results from conformational changes.

Furthermore, the splittings of the α-CH_2 and CH_3 groups were investigated. For the splitting of the α-CH_2 signal of the SDS/D_2O system a concentration dependency was found. This could be explained well by a change of conformations, which changes affects the value of the splitting (according to Karplus). Additionally, a temperature dependence of the splitting occurred for the α-CH_2 and CH_3 groups of both systems at concentrations close to the phase transition from the micellar region to a lyotropic liquid crystalline mesophase. This dependency seemed to be not related to a change of the J coupling but to a direct dipole-dipole coupling caused by an increasing order of the larger aggregates and/or an increasing viscosity of the samples.

4 Aqueous gel forming ternary systems containing surfactant and fatty alcohol

In this chapter, a series of samples with a constant amount of water of 97 wt. % and a varying ratio of sodium dodecyl sulfate to cetyl alcohol with a total mass fraction of 3 wt. % are investigated. The focus lies on the determination of the structure of emulsions which are able to form gels. Additionally, attempts are made to determine correlations between structure and emulsion properties. The influence of small changes of the processing parameters as well as the influence of the alkyl chain length of the alcohol on the emulsion properties are investigated, too.

4.1 System

For the investigation of the ternary system consisting of cetyl alcohol (CA)/ sodium dodecyl sulfate (SDS)/water, a series of samples is examined. The phase diagram (according to [2]) is shown in figure 4.1. The investigated samples are marked by crosses in the phase diagram. The water content of the samples is kept constant at 97 wt. % while the ratio of SDS to CA is varied. The gel-phase region exists, according to the literature, for samples with a molar ratio of CA/SDS greater than one [2, 57]. In the case of lower ratios, the samples are either mixtures of the gel phase and alcohol crystals, which is called coagel, or micellar solutions [2,57]. In order to reduce the ^{1}H NMR signal of water in the spectra of the J series, D_2O was used for sample preparation. The exchange of H_2O by D_2O as well as contaminations of the used chemicals can have an influence on the phase behavior and the phase boundaries. Hence, the actual phase boundaries can differ from those shown in the phase diagram. The assignment of the investigated samples to the appropriate phases will be discussed in the following chapters.

For the sample preparation the desired amounts of surfactant, alcohol and water were weighed into vials with a height of 55 mm, a diameter of 27 mm and a wall thickness of 3 mm. The three components were mixed with a magnetic stirrer using a stirring cross with a length of 10 mm at 70 °C at a stirring rate of 1000 rpm for 24 hours. After mixing, the samples were stored at room temperature. Table 4.1 lists the composition of the J series in weight percent. The mass fraction γ of the samples is defined as

$$\gamma = \frac{m_{\mathrm{SDS}}}{m_{\mathrm{SDS}} + m_{\mathrm{CA}}} \tag{4.1}$$

where m_{SDS} and m_{CA} are the masses of SDS and CA, respectively.

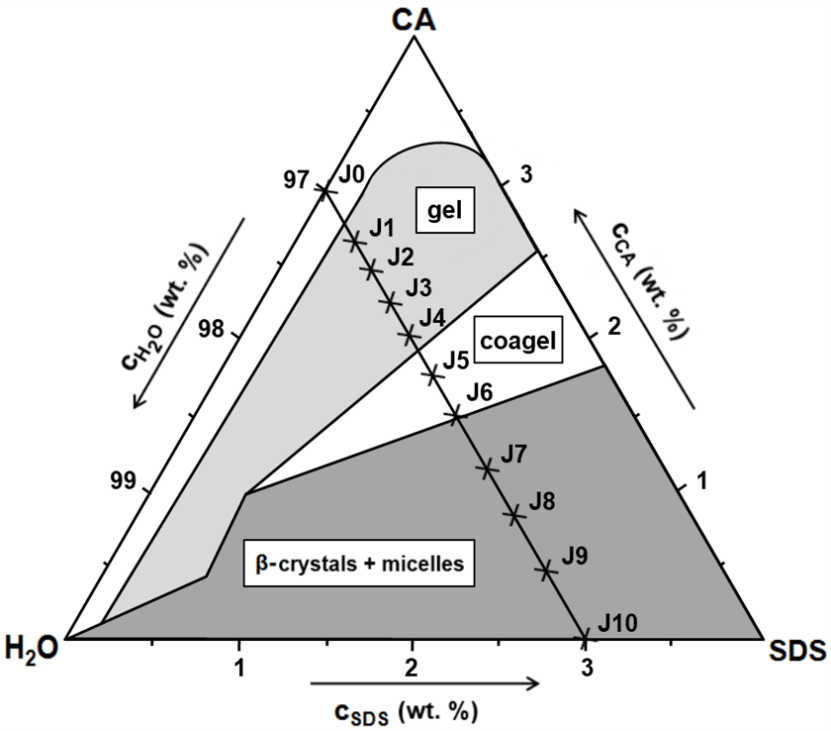

Figure 4.1: *Phase diagram of SDS/CA/water in the highly diluted area [2] with samples of the series labeled "J".*

Table 4.1: *Sample information of the J series.*

Sample	J0	J1	J2	J3	J4	J5
SDS [wt. %]	0.0	0.3	0.5	0.7	0.9	1.2
CA [wt. %]	3.0	2.7	2.5	2.3	2.1	1.8
D_2O [wt. %]	97.0	97.0	97.0	97.0	97.0	97.0
γ	0.00	0.10	0.17	0.23	0.30	0.40
n(CA)/n(SDS)	-	10.70	5.97	3.89	2.77	1.78

Sample	J6	J7	J8	J9	J10
SDS [wt. %]	1.5	1.8	2.1	2.8	3.00
CA [wt. %]	1.5	1.2	0.9	0.2	0.00
D_2O [wt. %]	97.0	97.0	97.0	97.0	97.0
γ	0.50	0.60	0.70	0.93	1.00
n(CA)/n(SDS)	1.19	0.79	0.51	0.09	0.00

4.2 Macroscopic appearance

In figure 4.2 photographs of the samples J1 (high CA content) to J10 (pure SDS) are shown. The pictures were taken 50 days after sample preparation. There are large differences in the macroscopic appearance of the samples. Sample J0 is an unstable dispersion of alcohol, separating into a D_2O phase with white solid alcohol floating on the surface (not shown in fig. 4.2). The samples J1 to J8 show either a complete (J1–J6) or partial (J7–J8) white shimmering turbidity. The shimmering property is an indication of periodic structures in the range of the wavelength of light. Sample J1 is highly viscous and gel-like with a high percentage of non-dissolved solids. The viscosity decreases with increasing amount of SDS. Sample J5 has only a slightly increased viscosity compared to the solvent. One week after the preparation, the samples J7–J8 phase separate into a clear phase and a white one of lower density. The fraction of the clear phase increases from sample J7 to J8. Samples J9 and J10 are clear and colorless solutions. After shaking sample J9 exhibits streaming birefringence.

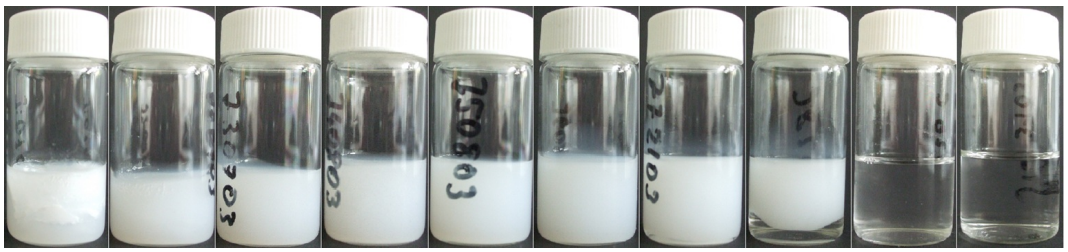

Figure 4.2: *Samples J1 (left) to J10 (right) 50 days after preparation.*

4.3 DSC

The thermograms of the samples J0 to J10 and of the pure solids (SDS and CA) were recorded at a heating rate of 5 K/min in the temperature range from 20 °C to 70 °C. From each prepared stock mixture three DSC samples were taken, which were measured four times. The measurements were performed between one day and ten days after the sample preparation. The peaks of the first measurement of a pan show nearly the same shape as the ones of the following measurements. But their peak temperature is in contrast to the second up to fourth measurement of the same pan not reproducible and up to 4 °C lower. For that reason, the first of the four measurements has not been included in the analysis of the signals. From the heating curves the peak temperature of the signals were determined (as described in appendix 7.2.1) and the results averaged. In figure 4.3, the peak temperatures are plotted against the mass fraction γ. The standard deviation of the averaged peak temperatures is below 0.5 °C and smaller than the size of the symbols.

Solid CA with a purity of 95 % shows two signals in the investigated temperature range (see figure 7.18). The first is located at 41.5 °C and is assigned to the transition from the orthorhombic (β) to the hexagonal (α) crystal form. The second signal is at 48.7 °C and corresponds to the melting point of the crystalline alcohol. In figure 4.3 both values are shown by dotted lines. The peak assignment is according to the literature [2, 58].

Goetz and El-Aasser investigated CA with a purity of 99 % at 2 K/min. For the peak temperatures of the $\beta-\alpha$ transition they found a temperature of 42 °C and for the melting point a temperature of 53 °C [2]. Additionally, a number of other values has been reported in the literature [58–62]. They were obtained via different methods (differential scanning calorimetry [58], differential thermal analysis [59], equilibrium spreading pressure [60], microscopy (heating) [61], glass capillary [62]) and vary from 39.5 °C to 44.6 °C for the $\beta - \alpha$ transition

and from 47 °C to 53 °C for the melting point.

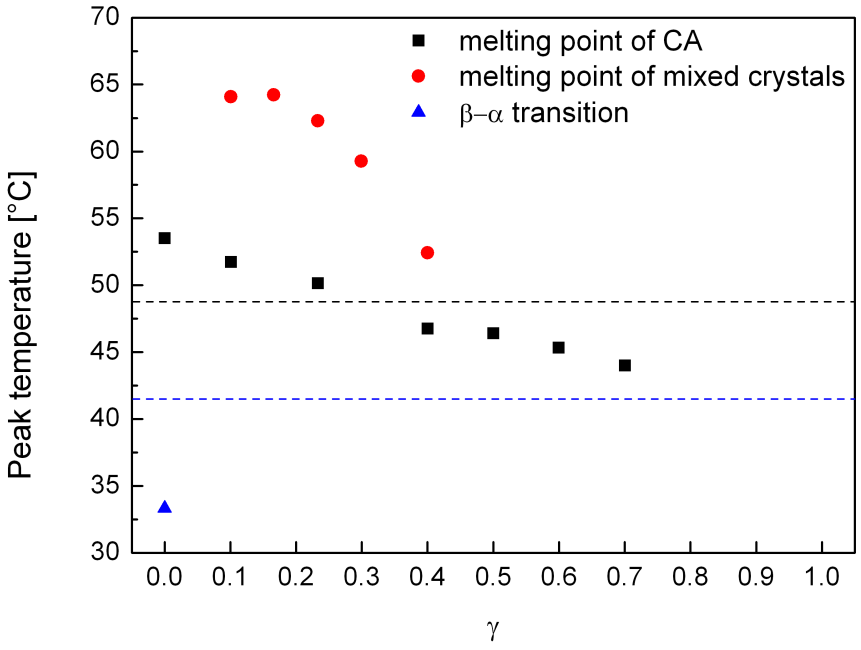

Figure 4.3: *Peak temperatures of the DSC signals of the J series. The dotted lines represent the melting point (48.7 °C) and $\beta - \alpha$ transition (41.5 °C) temperature of pure CA.*

From the literature [2, 58, 63] it is known that the addition of water to pure CA increases the temperature range in which the hexagonal crystal form exists and decreases the $\beta - \alpha$ transition temperature. It is also known that the addition of mixtures of SDS and water to CA lower the transition temperature below room temperature [2]. This behavior can clearly be seen in figure 4.3. All samples containing SDS in addition to water and CA show no peak above 20 °C for the $\beta - \alpha$ transition. In the case of J0 (97 wt. % of D_2O and 3 wt. % of CA) there is a $\beta - \alpha$ transition signal, whose peak temperature (33.34 °C) is significantly lower than that one of the pure alcohol (41.5 °C).

After the addition of water to CA (sample J0) the melting point of cetyl alcohol increases from 48.7 °C to 53.5 °C. This effect is already known in the literature. An increase of the melting point to a temperature between 50.8 °C [59]

and 52.1 °C [62]. This can be explained by consideration of the crystalline structure of cetyl alcohol. α crystals can accommodate water molecules between the planes of the alcohol OH groups, thus creating additional hydrogen bonds [58]. This leads to a swelling of the α form and as a consequence to a change in the molecular arrangement of the crystalline form. To melt the hydrated alcohol more heat is required to break the hydrogen-bonded network.

Furthermore it is known that the addition of water to an alcohol mixture consisting of 1-hexadecanol (CA) and 1-octadecanol in a ratio of 3:2 leads to an increase of the melting point from 47.5 °C to 54 °C (determined by DSC cooling measurements) [58]. This could also influence the melting point of J0 since the main impurity of cetyl alcohol is 1-octadecanol [58].

With increasing amount of SDS and decreasing amount of CA the melting temperature decreases until the melting peak disappears completely. Unfortunately, it could not be determined if the melting point corresponds to pure CA or CA with small amounts of SDS. The slope of the peak temperatures indicates that the signal corresponds to pure CA while the slope of the enthalpies (figure 7.19) indicates that the signal refers to mixed crystals. The melting point disappears above $\gamma = 0.7$ when a ratio of SDS to CA is reached which is sufficient to solubilize the non water-soluble cetyl alcohol. In this case, the compounds are completely dissolved and no melting point signal is detected.

Goetz and El-Aasser investigated mixtures consisting of CA and SDS that contained no water. They found that the composition of the mixtures had nearly no influence on the $\beta-\alpha$ transition but a strong influence on the melting point, which increased by almost 20 °C in a sample consisting of 24 wt. % SDS and 76 wt. % CA. They concluded that mixed crystals of SDS and CA are formed only above the $\beta - \alpha$ transition.

The thermograms of the samples located in the gel region measured by Goetz and El-Aasser showed only one increased melting point signal at ap-

proximately 70 °C. This peak is attributed to mixed crystals [2]. This type of signal (although at lower temperatures) was found for the samples J1 to J5. In the case of samples J1 and J3 an additional signal whose melting temperature corresponds approximately to the melting temperature of pure CA was found. This additional peak can be explained either by a ripening process, since the samples were measured up to ten days after the preparation, or to a less effective sample preparation than the one used by Goetz and El-Aasser. Since the precipitated white solids were not investigated separately it cannot be determined if they are composed of pure CA or CA with small amounts of SDS.

Based on the DSC results, the samples can be assigned roughly to the phases of the ternary phase diagram. Samples J10 and J9 are pure micellar solutions without alcohol crystals. J1 to J4 are clearly located in the gel phase. For the samples J5 to J8 the assignment is more difficult. Sample J5 could be in the gel but also in the coagel region. The DSC curves of sample J5 deliver very broad signals with a small intensity. Additionally, the melting temperature of the mixed crystals is very low. Hence, the sample seems to be within the transition region from gel to coagel. Samples J6 to J8 seem to be in the micellar region with additional crystals.

4.4 ^{1}H NMR spectroscopy

During the heating and cooling process in the temperature range from 30 to 70 °C, all samples were examined via ^{1}H NMR spectroscopy. The temperature was changed in steps of 5 °C. Information about the instruments used are given in chapter 7.2. All ^{1}H NMR spectra of the ternary system SDS/CA/D_2O show a temperature-dependent change in the chemical shift. Figure 4.4 illustrates the temperature dependence of sample J10 for a temperature cycle from 30 to 70 °C and back. It can be seen that the line shapes of the signals are reproducible and the change of the chemical shift is reversible.

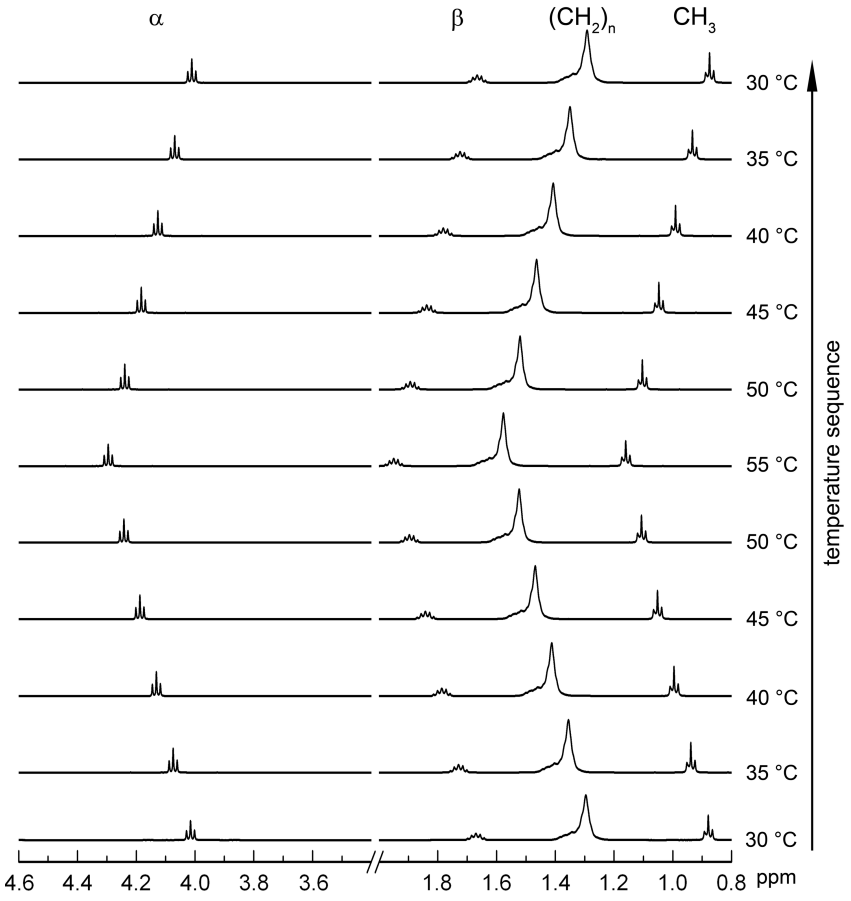

Figure 4.4: *Temperature dependent shift of ^1H NMR signals of sample J10 (3 wt. % SDS).*

Due to the reversibility, it can be concluded that the samples do not undergo permanent temperature dependent changes. The change of the chemical shift is due to the temperature dependence of the resonance frequency of HDO [64], which is used as lock signal.

For the analysis of the lineshapes of the ^{1}H NMR signals the spectra are plotted in figures 4.5 and 4.6 at 30 °C and 70 °C, respectively. The signal intensities of the spectra were normalized by dividing them by the maximum intensities of the alkyl chain signals. Sample J0 (3 wt. % CA) is not shown because the alcohol did not dissolve in water and thus no NMR signal could be detected. In the appendix (section 7.4.2.1) enlarged signals, except the alkyl chain signal, are shown. The chemical shift of the water signal (not shown) at 30 °C and 70 °C is set to a constant value for all temperatures leading to a change of the chemical shifts of the other signals, since they are referred to the temperature-dependent resonance shift of water.

The signals of the α- and β-CH_2 groups of SDS and the α-CH_2 signals of CA at 30 °C, starting at J10 for the SDS signal and at J9 for the CA signal, are well resolved and have a fine structure. With increasing amount of cetyl alcohol, the signals broaden until they cannot be detected without an intensive zoom at sample J5 for SDS and at J4 for CA. Starting with sample J9 the β-CH_2 signals of CA are broadened and cannot be seen anymore at sample J4. The signal of the CH_3 group of SDS behaves like the α_{SDS} signal with the difference that it remains visible at all sample compositions. The CH_3 group of CA behaves like the α_{CA} signal. In relation to the water signal (not shown), the alkyl chain signals of CA and SDS decrease in its peak height with increasing amount of alcohol. As a consequence of the decreasing signal intensity and the normalization of the spectra, the noise of the measurements becomes visible. In the gel region (J1–J4) the alkyl chain signal is strongly reduced. Especially the alkyl signal of J1 is a superposition of a narrow peak and a very broad

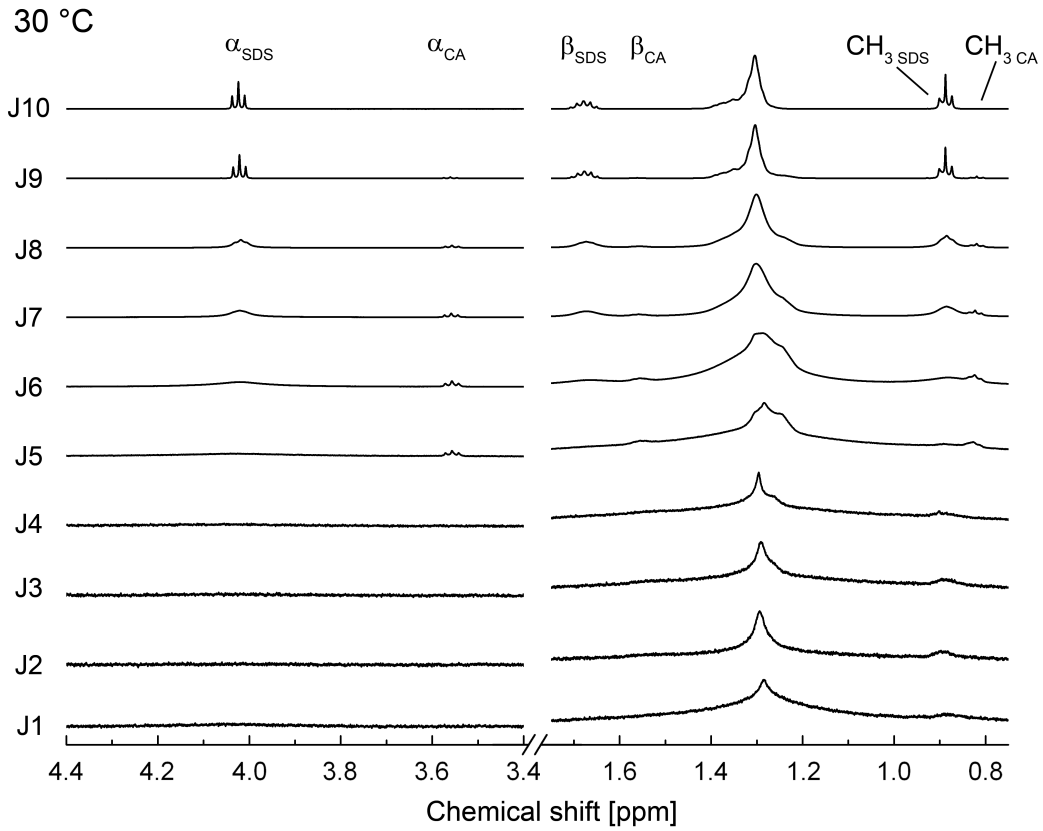

Figure 4.5: ^1H *NMR spectra of the samples J1 to J10 at 30 °C.*

signal. In the coagel region the narrow part of the alkyl chain signal becomes broader. The signal shape suggests that there are at least two signals which are not completely resolved. With increasing amount of SDS, the alkyl chain signal becomes narrower (J7–J10).

The comparison of the spectra leads to the conclusion that only the spectra of the samples J10 and J9 show J multiplets of SDS. Comparison with the DSC results shows a correlation. The samples J10 and J9 are the only samples which do not show a melting point (see fig. 4.3). This means that the components are completely dissolved. The other samples contain a solid fraction which melts at temperatures higher than 40 °C.

Like the signals of the α- and β-CH_2 groups at 30 °C, the α- and β-CH_2 groups at 70 °C (figure 4.6) starting at J10, are well resolved and have a fine structure. With increasing amount of cetyl alcohol the signals broaden until

they can not be detected for samples J6 and J5. From sample J4, the α- and β-CH_2 signals of cetyl alcohol reappear but are broadened. No significant difference in the behavior of the CH_3 groups at 30 °C and 70 °C is observed. The alkyl chain signal in the micellar region is rather narrow. With increasing amount of CA, the signal becomes broader (coagel region). In the gel region the width of the alkyl chain signal decreases with decreasing viscosity (J1 to J4).

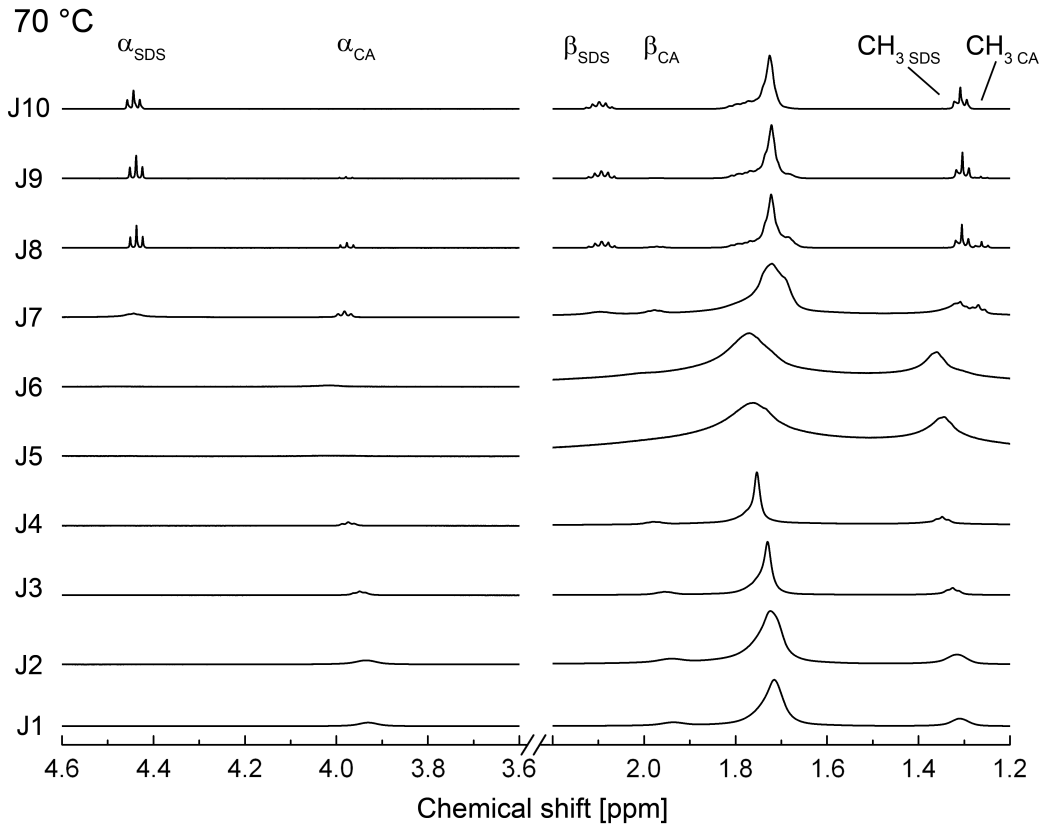

Figure 4.6: *^1H NMR spectra of the samples J1 to J10 at 70 °C.*

The differences in the signal shapes can be explained by different relaxation times, which depend on molecular dynamics. Fast isotropic motion results in long T_2, which corresponds to high resolution and sharp peaks (see chapter 2.4.2). It occurs, for example, for molecularly dispersed molecules or small micelles. The broadening of the signals due to addition of cetyl alcohol indicates a decreasing mobility of the molecules as a consequence of the growth of the

aggregates. If the amount of cetyl alcohol in the SDS/CA/D_2O-System, with CA having a smaller head group than SDS, is increased, the radius of curvature increases. As a consequence, the small spherical micelles change their shape to elliptical or cylindrical micelles [65], which can grow to extended lamellae. The molecules of the larger aggregates with a reduced motion have a short T_2, so that the signals get broadened.

Based on the proton NMR spectra, a more exact assignment of the samples to the regions of the phase diagram can be made. The spectra of J1 to J4 confirm the assignment of the samples to the gel region and the ones of the samples J10 and J9 to the micellar region. According to the spectra of J5 and J6, both samples can be assigned to the coagel region. The samples J7 and J8 are micellar solutions with additional crystals.

From the NMR spectra, more information than just the assignment of the samples to different phases of a phase diagram can be obtained. The intensity of characteristic signals can be determined and compared to the one of reference samples with known concentration. The deviation between the signal intensities of sample and reference corresponds to the undissolved amount of the investigated compound. This was tried for the alcohol and surfactant signals, but it became apparent, that this method does not work in this case.

To determine the fractions of mobile SDS and CA, the integrals of the α-signals of the proton spectra were calculated. To obtain the reference signal intensities of the samples with the maximum concentration, the integrals of the α-CH_2 signal of SDS in D_2O and of 1-hexadecanol in fully deuterated tetrachloroethane were determined and normalized to 1. Since the signals of the α-CH_2 groups of SDS and CA, respectively, results from the summation of all groups in the investigated volume, with each group yielding the same contribution to the total signal, the normalized intensity of the α-CH_2 signals expected for completely dissolved and mobile molecules is a linear function

of the composition given by γ. The measured integrals of the α-CH_2 signals of the samples J1 to J10 are also normalized to the corresponding reference intensity. This was done for the investigated temperatures of 30, 55 and 70 °C.

The measured normalized integrals of the α-CH_2 groups of SDS and CA at 30 °C are shown in figure 4.7 a) in addition to the theoretical intensities (CA: black line, SDS: red line). It can be seen that the optically clear micellar samples J10 and J9 almost show the expected behavior in contrast to the turbid samples J8 to J5, which differ strongly. The gel samples J4–J1 provide no signal. By raising the temperature to 55 °C (fig. 4.7 b)) the deviation of the signals of the α-CH_2 groups of SDS from the expected value increases while the deviation of the α-CA signal decreases. Since the temperature of 55 °C is above the melting point of pure cetyl alcohol, J1 to J4 provide signals, too. By further rise of the temperature to 70 °C (fig. 4.7 c)) the values of the normalized integrals of the samples J10–J5 are similar to the ones at 55 °C. This can be explained by the DSC results: 55 °C is already above the melting points, which could be detected for the samples J10 to J5. The signal intensities of the gel samples increase strongly. The reference intensities are hardly reached. The deviation from the reference intensity increases with decreasing amount of solids, which were present before the heating process.

To illustrate the lack of signal intensity in a more descriptive way, figure 4.8 shows the percentage deviation of the integrals of α_{CA} from the reference intensities at 70 °C. The hatched bars represent the normalized reference values. At a weight fraction of 1.0 the sample contains no alcohol, hence, no alcohol signal can be detected. At $\gamma = 0.0$, the sample is composed of 97 wt. % D_2O and 3 wt. % CA, which means that the intensity of the integral is maximal. The deviation of sample J9 ($\gamma = 0.93$) is within the error range so that a maximal value can be expected.

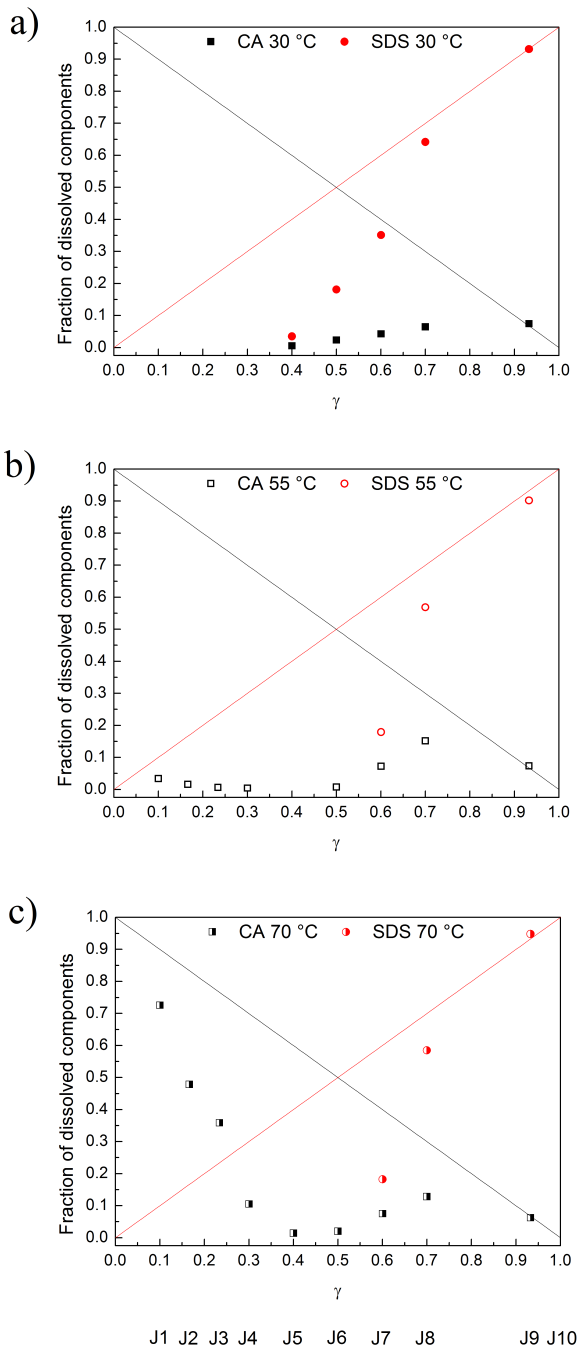

Figure 4.7: *Integrals of the α-CH_2 signals of SDS (red symbols) and CA (black symbols) of the J series at different temperatures (a) 30 °C, b) 55 °C, c) 70 °C). The diagonals represent the reference intensities of the integrals. The error of the data points amounts to* ± 0.5.

A possible explanation for the missing signal intensity even at 70 °C is the ageing of the samples which leads to solid amounts which are precipitated over time. The highest amount of solids can be found in sample J1 and decreases with increasing amount of SDS. In the spectrometer, the samples are heated to 70 °C where all solids should be molten. The lack of signal intensity could be explained by a temperature within the sample differing from the expected temperature and being below the melting point of the mixed crystals. Furthermore, it must be considered that the alcohol molecules of the molten crystals have the lowest density of the three components and will be found therefore mainly in the upper volume of the sample. As a consequence, the active volume from which the signal is detected is not representative for the whole sample.

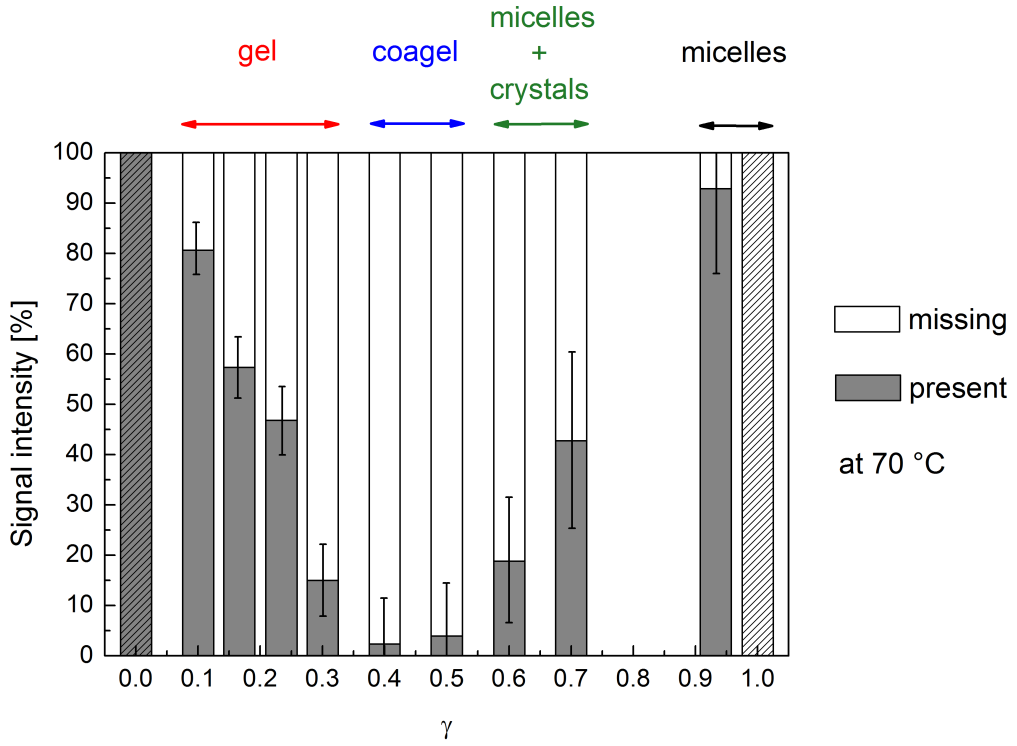

Figure 4.8: *Percentage deviation of the α_{CA} integrals from the expected signals at 70 °C.*

The samples, which consist of micelles and crystals (J8 and J7), phase separate visually into a clear and a turbid phase, leading to an alcohol-rich and

an alcohol-poor region. To illustrate the phase separation in the investigated region the samples were photographed in the depth measuring device of Bruker at 70 °C. The black bar of the 5/8 mm receive coils represents the region of the NMR tube which is measured (figure 4.9).

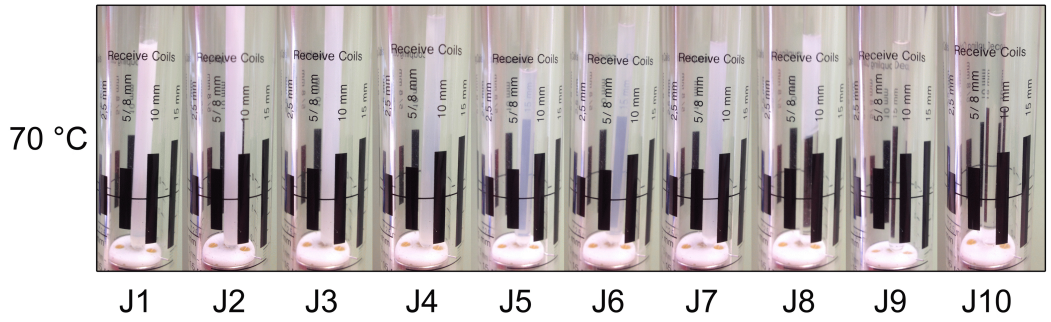

Figure 4.9: *Samples of the J series photographed at 70 °C in the depth measuring device of Bruker. The black bar of the 5/8 mm receive coil represents the position of the volume which is measured by the NMR spectrometer.*

Before measuring the samples, they were shaken by a vortex mixer. The determined signal intensities of the mixtures show a large deviation from the reference intensities. In addition to the mixture of sample J8, the clear and the turbid phase were separated and NMR spectra of the two parts were measured. The calculated ratio of the α-signal integrals ($\alpha_{\mathrm{SDS}} : \alpha_{\mathrm{CA}}$) is 12.7 : 1 for the clear and 2.9 : 1 for the turbid part. The mixture has a ratio of 3.6 : 1. The clear part of sample J8 takes circa 40 % of the whole sample volume. Calculating the ratio of the mixture from the ratios of the separated fractions ($0.4 \cdot 12.7 + 0.6 \cdot 3.6$) yields 6.82 : 1, which differs clearly from the measured one. Possible explanations for the deviaton of the ratios might be that the two parts were separated at a time at which the phase separation was not completed or concentration gradients within the separated parts were present.

It can be concluded, that it was not possible to determine the mobile fraction of surfactant and fatty alcohol of the investigated emulsions by the explained method due to phase separation, coexisting phases or inhomogeneous distri-

bution of the molecules. Despite, it could be shown that there is a large temperature dependent increase of the mobile fraction of the alcohol signal of the gel samples which is in agreement with the results of the DSC measurements.

4.5 Cryo-TEM

To get a visual impression of the structures of the aggregates, cryo-TEM pictures were captured. In figure 4.10 one of eighteen cryo-TEM pictures of gel sample J3 is shown. The contrast and brightness of the cryo-TEM picture were modified in order to make the structures recognizable in the printed image. Furthermore, the contours of the aggregates have been traced using image analysis software (Photoshop) are shown in the lower figure. The cryo-TEM pictures show unilamellar, multilamellar and multivesicular vesicles (UV, MV, MVV). Additionally, larger plate-like structures, which extend over several micrometers, can be seen. The platelets can result from vesicles with diameters exceeding the sample thickness of about 1 μm, which have collapsed during sample preparation. All aggregates show dark boundary lines with a thickness of less than 10 nm.

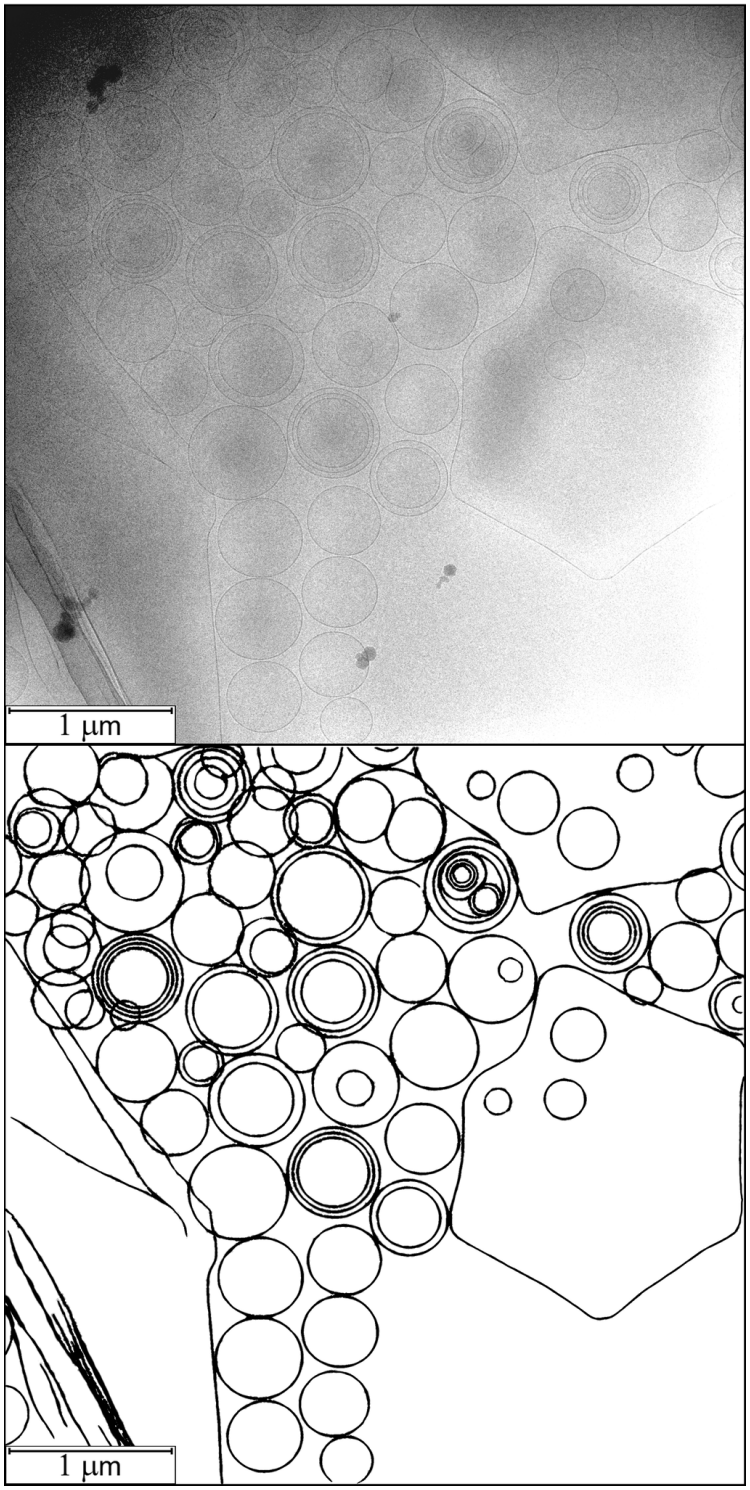

Figure 4.10: *Top: Cryo-TEM image of the gel sample J3. Bottom: Reproduction of the structures seen by cryo-TEM using Photoshop.*

All eighteen pictures have been analyzed statistically. The results are shown in figures 4.11 to 4.13 and summarized in table 4.2. The abundance of the different vesicle types (UV, MV, MVV) shows a ratio of 638 : 239 : 26 or 1.00 : 0.37 : 0.04 (fig. 4.11 a)). For the 239 multilamellar vesicles, the number of bilayers of each vesicle were counted. In figure 4.11 b) the ratio between vesicles with two, three, four, five and six bilayers is illustrated. The total number of this ratio is 161 : 50 : 26 : 0 : 2, normalization delivers proportions of 1.00 : 0.31 : 0.16 : 0.00 : 0.01.

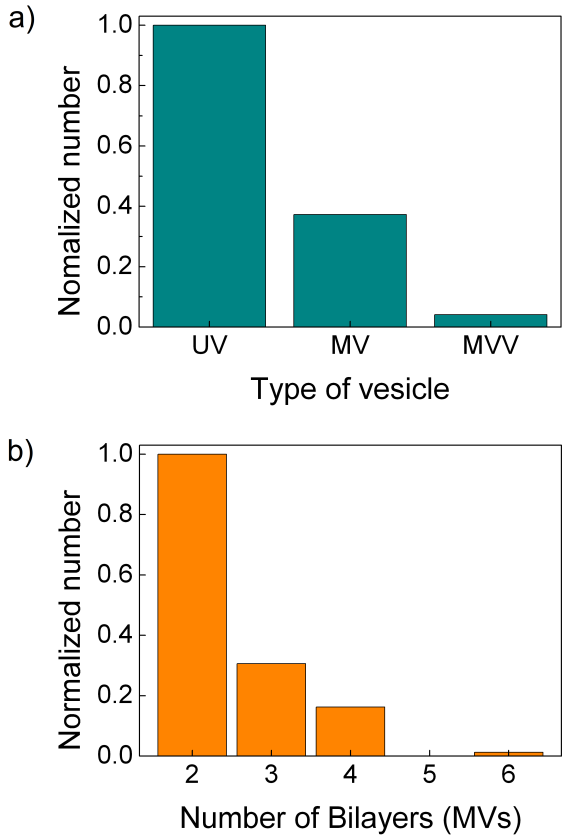

Figure 4.11: *Statistical evaluation of the vesicles: type and number of bilayers in the case of MVs.*

Figure 4.12 shows the distribution of the vesicle diameters of the different vesicle types. The most frequent UV diameters are between 200 and 400 nm (fig. 4.12 top), and the most abundant MV diameters between 300 and 500 nm (fig. 4.12 middle). The MVV show most frequently diameters between 500 and

700 nm (fig. 4.12 bottom). The average diameters of uni- and multilamellar vesicles are 0.33 and 0.43 μm, respectively. Multivesicular vesicles are even larger with an average diameter of 0.65 μm. The average overall diameter is 0.368 μm.

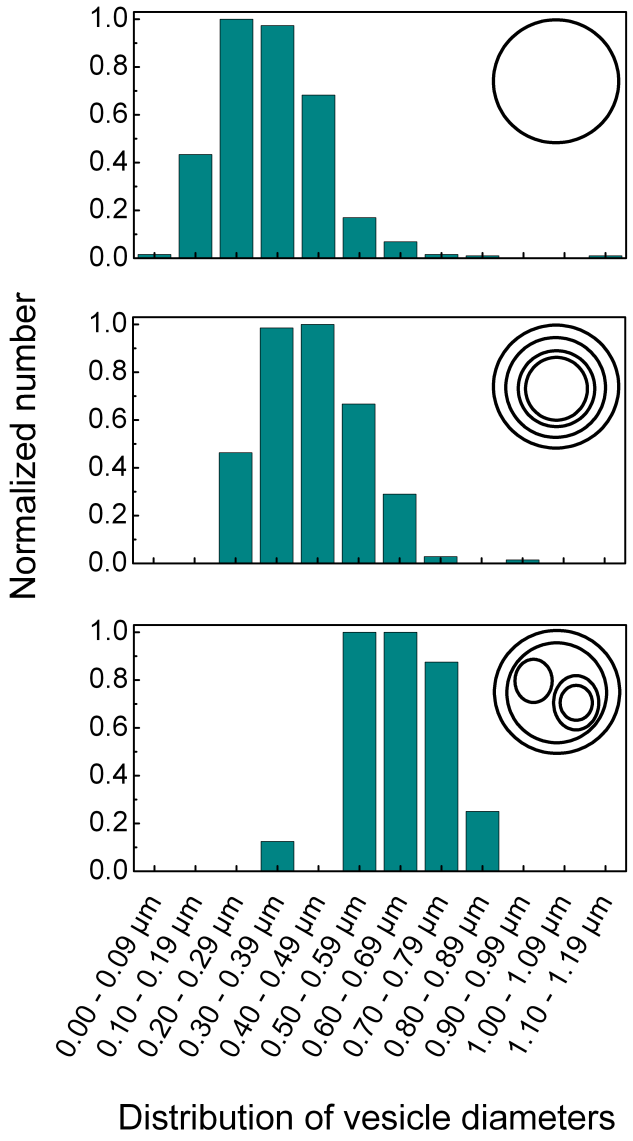

Figure 4.12: *Distribution of the vesicle diameters. Top: unilamellar vesicles; Middle: multilamellar vesicles; Bottom: multivesicular vesicles.*

For the 239 multilamellar vesicles the distances between adjacent bilayers were analyzed. The results are shown in figure 4.13. The most frequent dis-

tance is between 20 and 59 nm and the average distance is 61.14 nm.

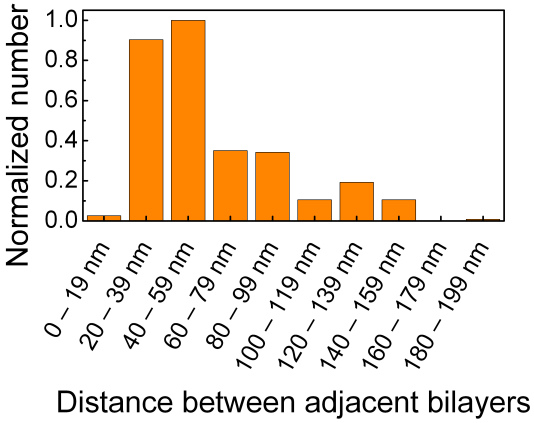

Figure 4.13: *Distance between two adjacent bilayers in multilamellar vesicles.*

Table 4.2: *Results of the quantitative analysis of the cryo-TEM pictures of sample J3.*

vesicle type	total number	ratio	average diameter
UV	638	1.00	0.33 μm
MV	239	0.37	0.43 μm
MVV	26	0.04	0.65 μm

Average diameter of all vesicles	0.368 μm
Average distance between two adjacent bilayers of a MV	61.14 nm

In figure 4.14, a cryo-TEM picture of sample J9 is shown which shows predominantly flat long aggregates with a length of several μm and a width of about 0.4–1.2 μm. These structures sometimes show Bragg reflections of crystalline regions at some orientations (not shown in fig. 4.14). Since no aggregates could be detected by optical microscopy and light diffraction the temperature behavior of the sample below 20 °C was investigated. This was done to find out at which temperature crystals are formed. Figure 4.15 shows the photographs which were taken.

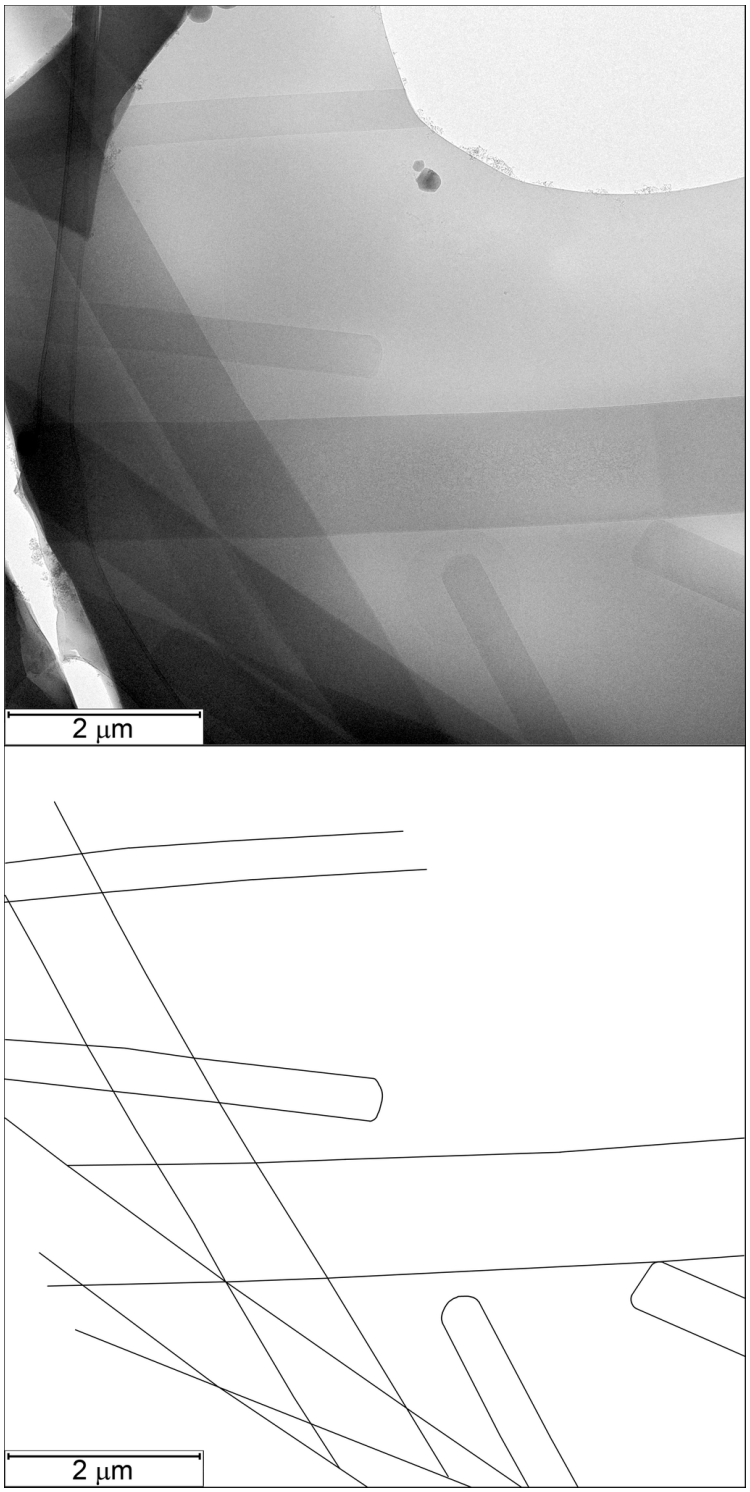

Figure 4.14: *Top: Cryo-TEM image of the gel sample J9. Bottom: Reproduction of the structures seen by cryo-TEM using image analysis software.*

After one hour at 10 °C the sample became slightly turbid. Over a storage time of nine hours first crystals could be detected with the naked eye. The amount of crystals increased (11 h) and they are deposited at the bottom of the vial (25 h). After 25 h at 10 °C the sample was stored at 20 °C. It can be seen that 10 h at 20 °C are not sufficient for dissolving the precipitated crystals. Even after 69 h at 20 °C there is still a phase separation between a clear and a milky phase.

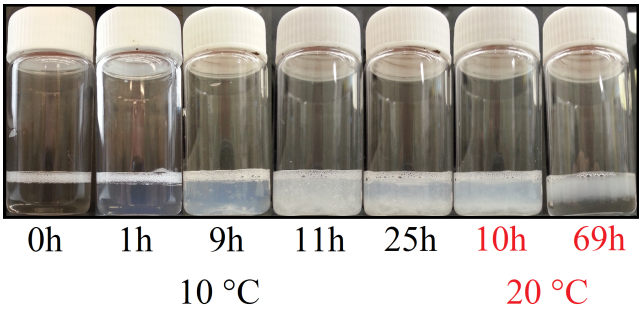

Figure 4.15: *Temperature dependent macroscopic appearance of sample J9.*

The precipitation of crystals results from storing the sample below the Krafft temperature. The exact value of the Krafft temperature was not determined. The exposure of the samples to temperatures of 10 °C less for an extended time probably occurred during the shipping of the samples in winter from Paderborn to Berlin by Deutsche Post. Since the operator of the cryo-TEM instrument did not know that the sample should be clear and homogeneous, he could have measured the sample with precipitated crystals. In this case, the observed flat, long aggregates with Bragg reflections, which are typical for crystals, could be explained.

Figure 4.16 shows one of the cryo-TEM images of the coagel sample J6. Deformed and broken vesicles as well as plate-like structures can be detected.

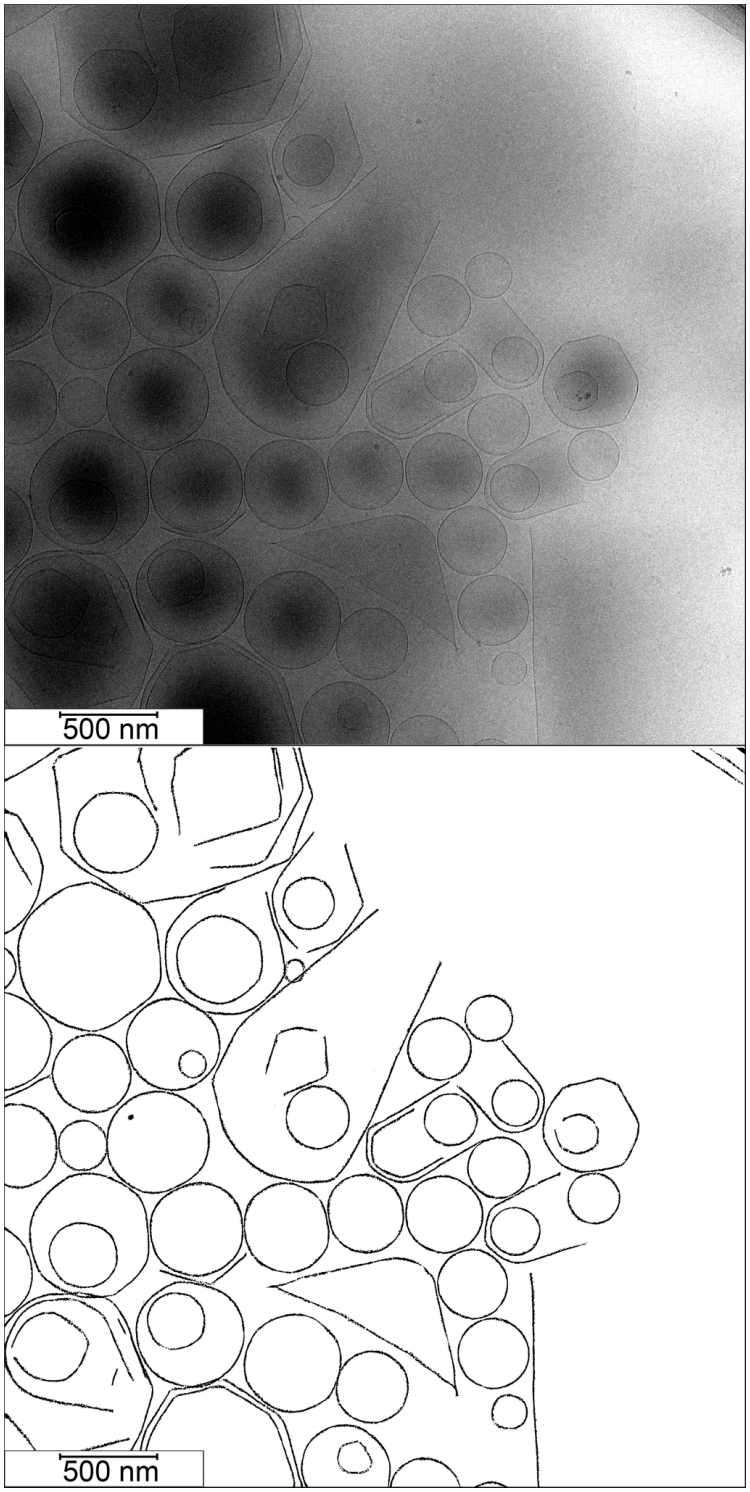

Figure 4.16: *Top: Cryo-TEM image of the gel sample J6. Bottom: Reproduction of the structures seen by cryo-TEM using image analysis software.*

The distribution of the unilamellar vesicle diameters of the coagel sample shown in figure 4.17 is comparable to the one of sample J3. The ratio of uni- to multilamellar vesicles increases nearly by a factor of five to 1 : 0.075. The ratio of the number of vesicles with two or three bilayers decreases to 1 : 0.13. No multivesicular vesicles could be detected. The results of the cryo-TEM analysis are listed in table 4.3. The obtained diameters and ratios have to be interpreted carefully since the cryo-TEM pictures of sample J6 have a lot of dark shadows at the center of the vesicles. Hence, it is possible that some layers could not be detected and included in the analysis.

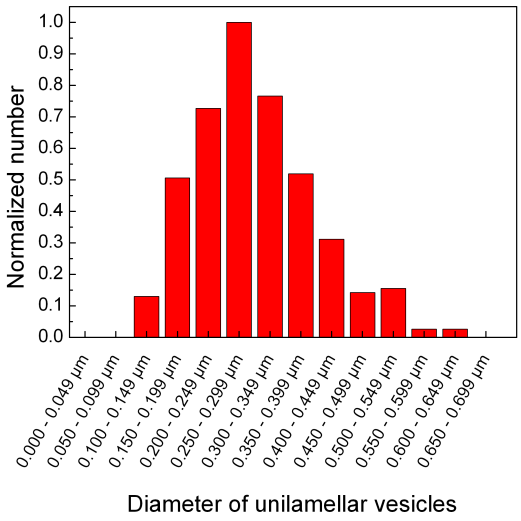

Figure 4.17: *Diameter distribution of unilamellar vesicles of sample J6.*

Table 4.3: *Results of the quantitative analysis of the cryo-TEM pictures of sample J6.*

vesicle type	total number	ratio	average diameter
UV	332	1	0.302 μm
MV	25	0.075	0.454 μm
UV+MV	357		0.338 μm

4.6 SANS

For the determination of the structures of the aggregates of the J series V-SANS experiments (very small angle neutron scattering [66]) were performed. In figure 4.18 the scattering curves of the gel samples J1–J4 can be seen. To enhance the correlation peaks at higher Q values the scattering curves are shown in figure 4.19 in a Kratky plot.

At smaller Q values the scattering curves show a Q^{-2} behavior. This occurs for vesicular structures, if the thickness of the bilayer is much smaller than the radius of the D_2O core of the vesicle [67]. As a consequence, the scattering of the shell becomes identical to the scattering of an extended sheet [67]. At Q values larger than 0.18 nm^{-1} the scattering curves of sample J1 and J2 start to drop off with a slope smaller than Q^{-4}. This slope indicates that the interface between the bilayer and D_2O is rough, since the Q data do not follow the Porod power law, which is characteristic for sharp interfaces [67–69]. The range of the Q^{-2} behavior is limited at high Q values by the overall diameter of the vesicles and varies inversely with it [67].

All gel samples show a pronounced shoulder between 0.07 and 0.22 nm^{-1} which can be interpreted as a smeared correlation peak caused by periodic lamellar structures. The resolution of this peak is influenced by the number of regularly stacked scattering planes. Another factor, which influences the shape of the lamellar correlation peak is the size distribution of the lamellar distances in a vesicle since different lamellar distances result in correlation peaks with different peak positions. Looking at the cryo-TEM picture (figure 4.10) and the analysis (figure 4.13) of sample J3 confirms that such a distribution of lamellar distances could also be a cause for the broad correlation peaks. In the case of J3 the lamellar correlation peak corresponds to a periodic distance of 39.3 nm. This size is consistent with the lamellae distances determined by the cryo-TEM analysis.

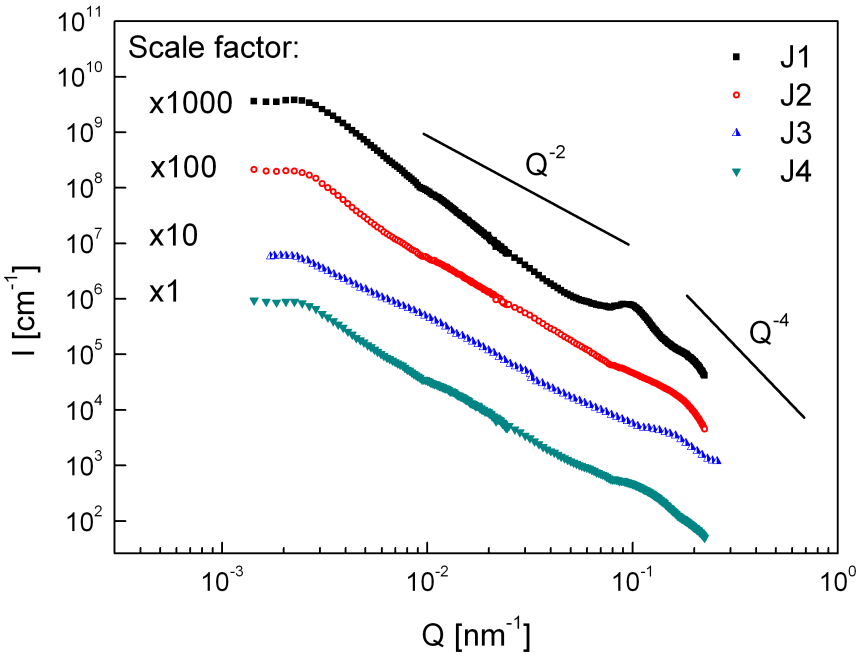

Figure 4.18: *V-SANS scattering curves of the gel samples.*

There is no obvious trend in position or shape of the correlation peak. This may be due to the fact that the structure of the samples depends on the mechanical influences during the sample preparation. The applied protocol of sample preparation does not ensure a homogeneous mechanical strain all over the sample volume in the vial. For this reason the size and shape of the aggregates cannot be controlled. As a consequence there are strong fluctuations of the structure from sample to sample and no information on a relationship between sample composition and the distance of the lamellae in a vesicle can be deduced.

In addition to the lamellar correlation peak, a very weak shoulder can be seen between $0.9 \cdot 10^{-2}$ and $2.5 \cdot 10^{-2}$ nm^{-1} in figures 4.18 and 4.19. This Q range corresponds to distances between 0.25 and 0.67 μm. The position of the shoulder may match the most frequent vesicle diameters of the diameter distribution. For sample J3 this assumption is consistent with the results of

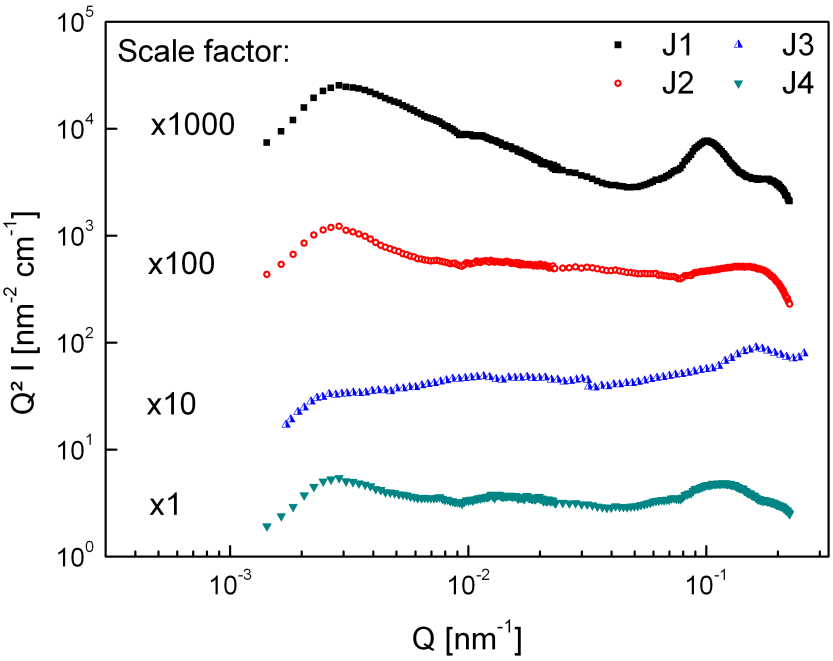

Figure 4.19: *Kratky plot of the scattering curves of the gel samples.*

the cryo-TEM analysis (see figure 4.12).

A third correlation can be seen close to the beginning of the scattering curves. It is between $1.8 \cdot 10^{-3}$ and $2.6 \cdot 10^{-3}$ nm^{-1} indicating distances on the micrometer length scale between 2.42 and 3.49 μm. This signal could match the distances between the centers of the vesicles. According to the cryo-TEM pictures of sample J3 a typical distance between two vesicles is circa 1 μm. The deviations of the distances between the aggregates of the cryo-TEM pictures from the ones determined by V-SANS could result from the sample preparation for the cryo-TEM measurements. During that, a large amount of solvent is removed by the blotting procedure. As a consequence the distances between the vesicles decrease.

4.7 SAXS

To detect even smaller structures of the J series, small and wide angle X-ray scattering (SAXS, WAXS) experiments were performed at room temperature. Unfortunately, the WAXS experiments of samples J2, J3 and J9 showed only the background signal of the sample holder. This is probably due to the fact, that only a thin film could be measured by the diffractometer. As a consequence, there are, due to the high water content of 97 wt. %, not enough crystals which would contribute to the WAXS signal. In contrast to the WAXS measurements, the SAXS experiments worked well. Before measuring the phase separated samples, they were mixed by shaking them by hand.

Each sample of the J series was measured three times by SAXS. The data obtained were reproducible. Figure 4.20 shows one of the measured scattering curves for each of the gel samples J1 to J4 at room temperature. The scattering curves of samples J5 to J10 are shown in chapter 7.4.3. The average peak positions are shown in figure 4.21. The standard deviation of most peaks is smaller than the size of the symbols. In the other cases error bars are added. 2θ is twice the glancing angle (see chapter 2.5). It can be seen that all samples which contain SDS and CA show at least two peaks (black and blue symbols). The first peak at lower Q values is quite broad and often shows a shoulder. The peak positions obey the relationship of 1:2. This ratio is typical for lamellar structures [3, 31, 70]. The periodic distance d between the scattering planes is calculated by using the Bragg equation (eq. 2.25). The results are shown in table 4.4.

From the cryo-TEM pictures of sample J3 it is known that only the boundary lines of the aggregates, with a thickness smaller than 10 nm, are in the appropriate size range of the distances found. Additionally, micelles as well as alcohol crystals, which were not detected by cryo-TEM, could be in this dimension.

Table 4.4: *Spacing between the scattering planes calculated by the Bragg equation.*

γ	0.10	0.17	0.23	0.30
$d(n{=}1)$ [nm]	4.45 ± 0.02	4.51 ± 0.08	4.63 ± 0.22	4.46 ± 0.01
$d(n{=}2)$ [nm]	4.14 ± 0.19	4.41 ± 0.01	4.43 ± 0.02	4.39 ± 0.03

γ	0.40	0.50	0.60	0.70
$d(n{=}1)$ [nm]	4.75 ± 0.02	4.19 ± 0.05	4.05 ± 0.03	3.93 ± 0.04
$d(n{=}2)$ [nm]	4.36 ± 0.40	4.04 ± 0.04	3.99 ± 0.03	3.94 ± 0.02

γ	0.93	1.00
$d(n{=}1)$ [nm]	3.89 ± 0.01	3.88 ± 0.04
$d(n{=}2)$ [nm]	3.89 ± 0.02	3.91 ± 0.02

The thickness of two extended CA molecules is around 4.5 nm [3]. This size is consistent with the determined periods of the alcohol rich samples. With increasing amount of SDS (C_{12} alkyl chain) and decreasing amount of CA (C_{16} alkyl chain) the measured distances decrease. For sample J10 (3 wt. % in D_2O) the calculated bilayer thickness is circa twice the elongated SDS length, which is approximately 1.9 nm [71].

At room temperature samples J1 to J8 contain crystals, according to the DSC results. The measured distances and the lamellar structure probably correspond to the crystals. The additional signals of sample J7 and J8 give evidence of two crystalline species and are consistent with the phase separation of the samples.

A possible explanation for the presence of peaks in the clear micellar samples J9 and J10 might be ageing of the samples or evaporation of the solvent during the measuring process.

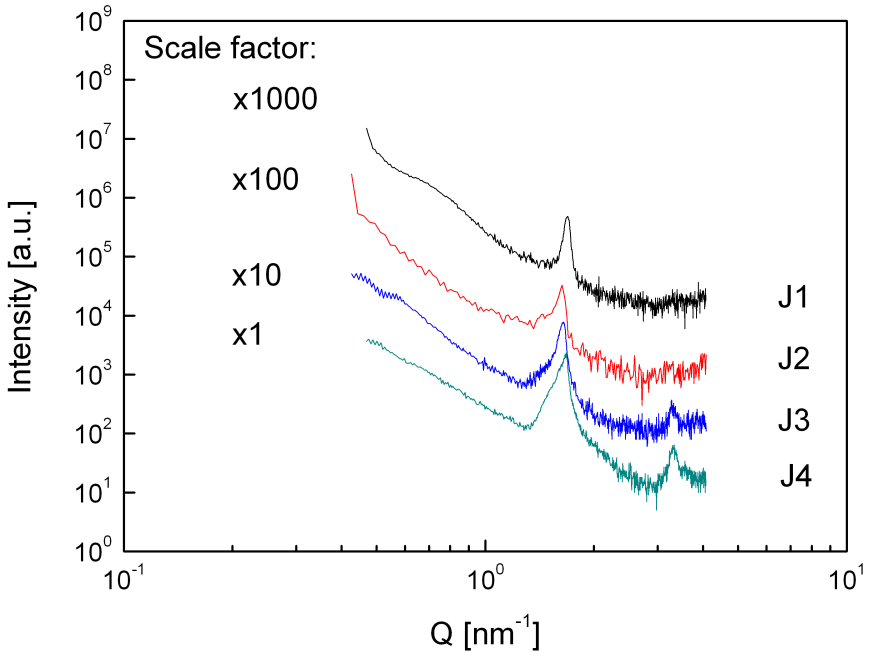

Figure 4.20: *SAXS scattering curves of gel samples J1 to J4 at room temperature.*

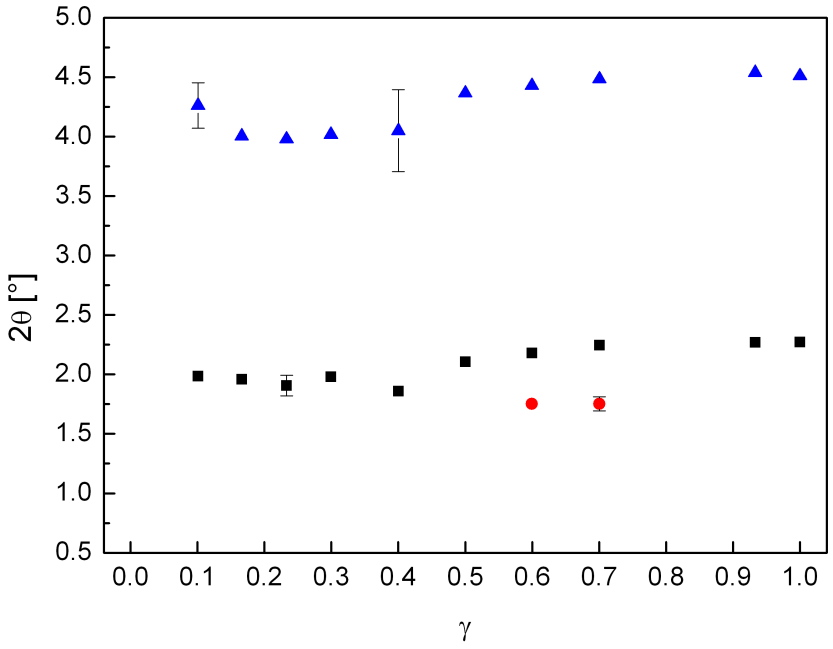

Figure 4.21: *Peak positions of the SAXS signals.*

4.8 ^{1}H diffusion NMR

The diffusion NMR measurements were carried out on a 200 MHz NMR spectrometer at a temperature of 30 °C. A pulsed-gradient spin echo sequence with trapezoidal magnetic field gradients was used as described in chapter 2.2. The gradient strength g was increased from zero to the maximum value in 32 steps. For each of the 32 spectra 16 scans were accumulated. The variables τ, Δ, δ and ϵ of a series of measurements were specified before the measurement and kept constant for the series. For analyzing the Fourier transformed spectra they were exported from TopSpin and imported into Origin 8G. The water signals were integrated using Origin 8G. The integrals of a series of measurements have been normalized to the integral with the highest value.

Figure 4.22 shows the 32 ^{1}H spectra of sample J10 for different gradient strengths at a constant Δ. The signal intensity of the HDO signal, which decays much faster than the surfactant signals, is enlarged. For the quantitative analysis the integrals of the HDO signal were determined.

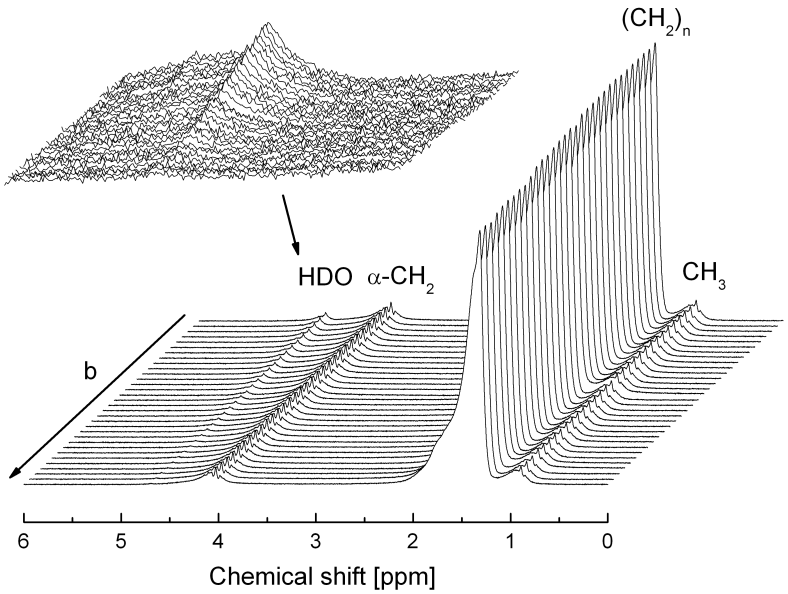

Figure 4.22: *^{1}H NMR measurement on sample J10 for $\Delta = 50$.*

In figure 4.23 one of the data sets of sample J10 and its fit are shown. Obviously, the data show a monoexponential decay which implies that only one diffusion coefficient exists. The accuracy of the fit is quite good as it is for all other monoexponential data sets, too.

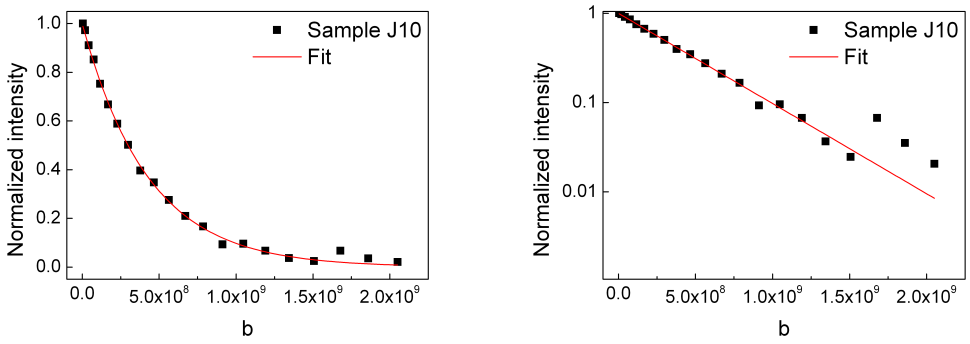

Figure 4.23: *Integrals of the water signal of sample J10 for different values of b as defined by equation 2.5 with linear (left) and logarithmic intensity scale (right).*

The proton NMR spectra of sample J1 are shown in figure 4.24. Due to the high viscosity and therefore the low mobility of the aggregates, only the HDO signal was detected. The experimental data of gel sample J1 (fig. 4.25) clearly differs from the monoexponential behavior. For fitting the data the existence of two diffusion coefficients was assumed. One represents the diffusion coefficient of free water and the other one of water which is trapped in or between vesicles. The accuracy of the biexponential fits is worse than the monoexponential fits but it increases with decreasing amount of cetyl alcohol.

In figure 4.26 the measured diffusion coefficients of all samples for different times Δ are illustrated. For the samples with only one diffusion coefficient the values of the diffusion coefficient are independent of Δ which is typical for free diffusion. The diffusion coefficients of the samples in the micellar region are consistent with the literature value of pure HDO which is between $2.14 \cdot 10^{-9}$ and $2.43 \cdot 10^{-9}$ m^2s^{-1} at 25 °C [72]. With increasing amount of CA the coefficient decreases due to the occurrence of larger aggregates like alcohol

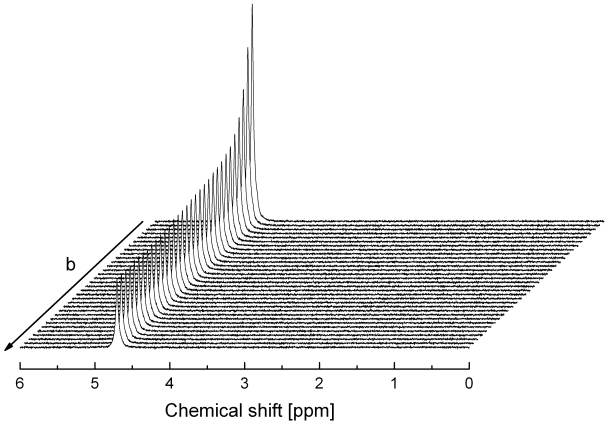

Figure 4.24: *^1H diffusion NMR spectra of sample J1 for different experimental settings (values of b).*

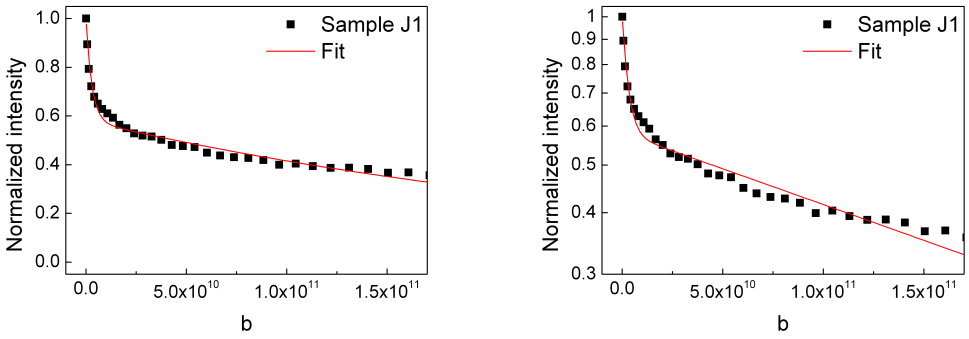

Figure 4.25: *Integrals of the water signal of sample J1 for different values of b as defined by equation 2.5 with linear (left) and logarithmic intensity scale (right).*

crystals for the samples J8–J7 or vesicular structures for samples J6–J1 which hinder the diffusion of the free water.

In the gel and coagel region, there are two diffusion coefficients, which differ significantly from each other in their value. The faster one corresponds to the self diffusion coefficient of free water. The deviation from the reference value of the free water diffusion coefficient may be due to the poor fit accuracy. The slower diffusion coefficient corresponds to the diffusion of restricted water embedded in confining structures. In this case the distance traveled by the diffusing species depends on size and shape of the confining geometry and the measured apparent diffusion coefficient may depend on the time between the

gradients. In the experiments performed the diffusion time was changed in a range in which not every water molecule diffuses far enough to feel the effects of restriction. For that reason, the diffusion coefficient depends on Δ [39].

In the case of sample J6 it is difficult to say if there are two diffusion coefficients or not. According to the cryo-TEM pictures, the sample contains vesicular structures. But in comparison to the gel structures the vesicles are smaller and often broken. Hence, the amount of restricted water is smaller. The biexponential fit delivers diffusion coefficients which are very close to each other (with a difference between 3 and 6 %) and the fraction of slowly diffusing water is very low. Furthermore, it is possible to fit the experimental data in a monoexponential way.

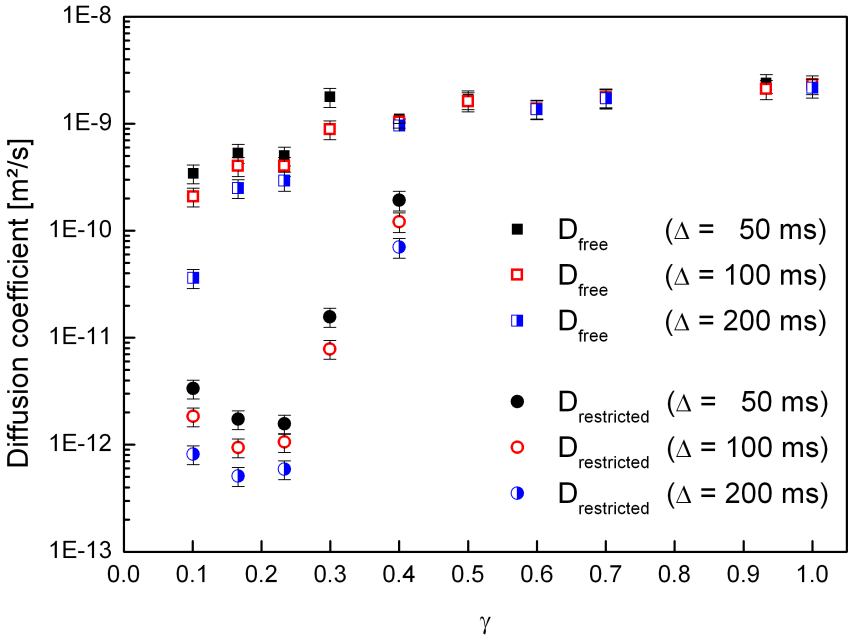

Figure 4.26: *Diffusion coefficients of free and restricted water for the samples of the J series for different diffusion times.*

In figure 4.27 the fraction of the free and restricted water molecules is illustrated. Starting at J1 the amount of restricted water decreases with decreasing amount of cetyl alcohol. That means that the size of the vesicles or the num-

ber of vesicles decreases with decreasing amount of alcohol since the amount of trapped water decreases. Furthermore, it could be the case that the vesicles are filled with solids (dark areas in the center of the vesicles of the cryo-TEM image of sample J6).

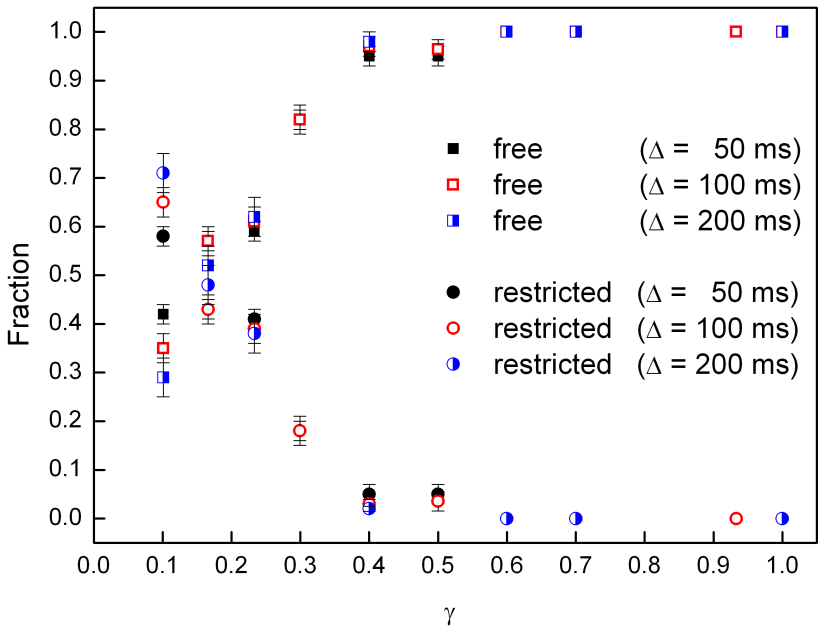

Figure 4.27: *Fractions of free and trapped water distinguished via exponential fits.*

4.9 Rheology

To get information about the mechanical properties of the samples rheological measurements were performed. For samples J1–J8 an amplitude sweep experiment was performed at 30 °C in order to find the linear viscoelastic regime. The deformation was changed from 0.01 to 15 % at an angular frequency of $\omega = 10$ Hz. Before the actual measurement the sample was presheared with a shear rate of 1 s^{-1} for 5 minutes. The preshearing is necessary to create a uniform starting situation since the samples underwent different shearing forces during the filling of the shear cell. Figure 4.28 shows a typical data set from sample J1. The behavior of the elastic modulus (G'), the loss modulus (G'') and the loss tangent or damping factor (tanδ) can be seen. The linear viscoelastic regime is marked by the dotted rectangle.

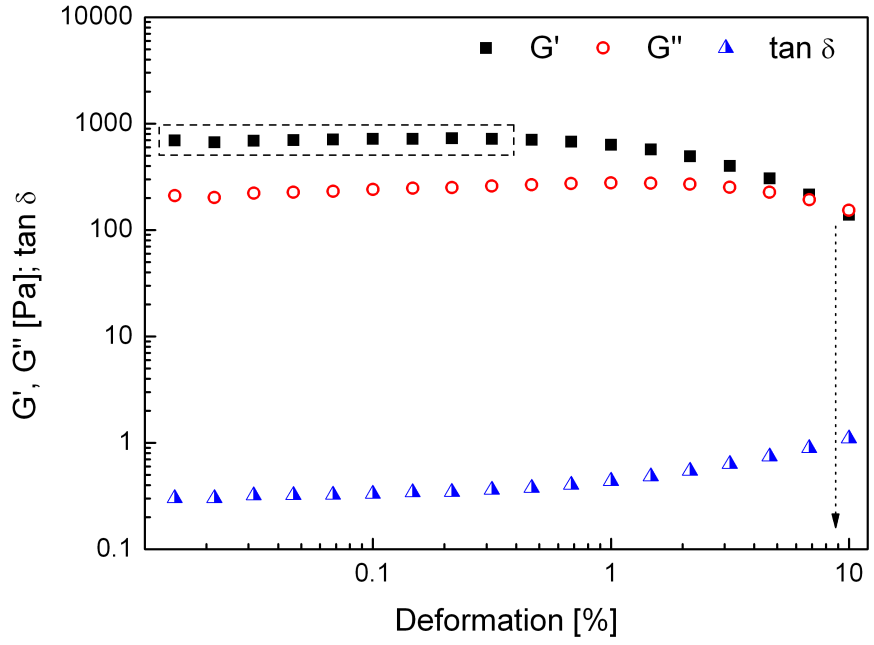

Figure 4.28: *Amplitude sweep of sample J1 at 30 °C.*

The amplitude sweep measurements of samples J2 and J6, which were not presheared, show an increase of G' and G'' at the beginning of the experiment

before they reach a constant value (see figures 7.42 and 7.46 in chapter 7.4.5).

For all investigated samples the value of G' was larger than G'' in the linear viscoelastic range. This implies that the stored energy dominates over the dissipated energy, which is a typical property of a viscoelastic gel [41]. Outside of the linear viscoelastic regime the mechanical stress is high enough to change the structure of the samples irreversibly. In this case the elastic modulus decreases. The critical deformation can be defined as the intersection of the G' and G'' curves ($tan\ \delta = G''/G' = 1$) [3, 41] and is denoted by the arrow in figure 4.28 for sample J1.

The critical deformation data are listed in table 4.5. They decrease tendentially with increasing amount of SDS. Sample J4 is the only one that does not follow this trend. No information could be found for its high critical deformation. Since only one amplitude sweep experiment was performed for each sample, the denoted errors represent the distance between the critical deformation and the adjacent data points of the measurement data. Since a decrease of the cross over point indicates a decrease in the elastic properties of a material [3] the elasticity of the samples will decrease with increasing SDS.

Table 4.5: *Critical deformation* ($tan\ \delta = G''/G' = 1$).

Sample	Crit. deformation [%]
J1	8.47 ± 1.55
J2	10.97 ± 3.00
J3	9.32 ± 2.50
J4	14.70 ± 5.00
J5	8.29 ± 1.00
J6	4.06 ± 0.60
J7	3.16 ± 0.60
J8	2.15 ± 0.60

In figure 4.29 the linear viscoelastic range of samples J1–J8 is illustrated. Because of the low density of measured data points the upper and lower limit of the end of the linear viscoelastic range are shown. The exact value is between them. It is obvious that the range of the linear viscoelastic region decreases

with increasing amount of SDS.

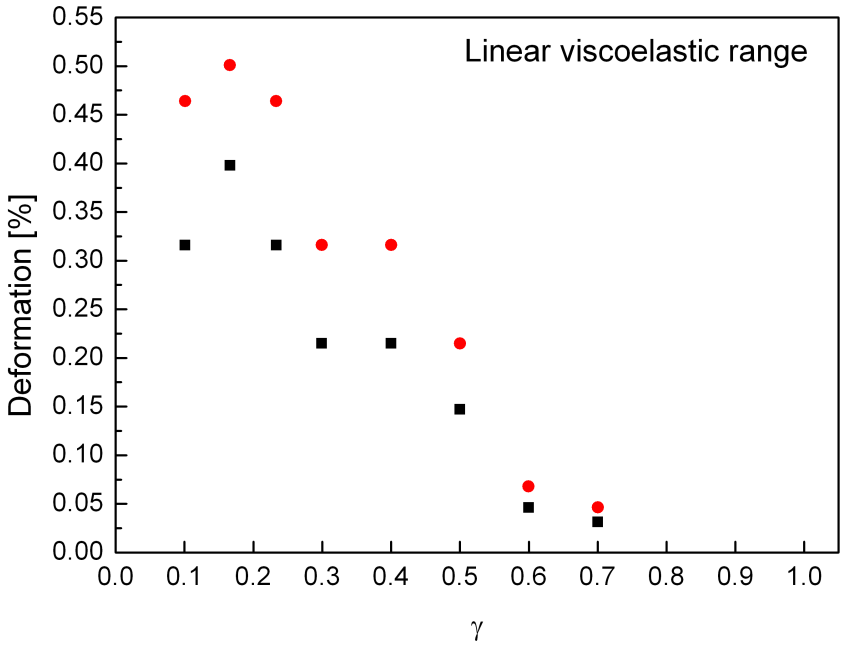

Figure 4.29: *Linear viscoelastic range at 30 °C. The red circles represent the upper limit and the black squares the lower limit of the limit of the linear viscoelastic range.*

The results of the amplitude sweep measurements show that the extension of the linear viscoeleastic region and the required deformation for breaking the network structure are higher for low SDS amounts. Hence, network structures of samples with more SDS would break down much more easily upon exposure to mechanical stress like vibrations.

Frequency sweep experiments were performed for samples J1 to J6. Each of the samples was measured three times. The deformations used are listed in table 4.6. For each measurement a new sample was brought onto the plate of the cone-and-plate geometry. Before running the frequency sweep the samples were presheared for 5 min at a shear rate of 1 s^{-1}.

The values of G', G'' and the complex viscosity η^* averaged over the three measurements of sample J1 are shown in figure 4.30. The error bars represent

Table 4.6: *Deformation values used for the frequency sweep measurements.*

Sample	J1	J2	J3	J4	J5	J6
Deformation [%]	0.3	0.2	0.2	0.2	0.1	0.1

the standard deviations of the data points. It can be seen that the values of G' are higher than the ones of G'' and that both moduli increase slightly with increasing frequency. The complex viscosity decreases with increasing frequency, which is typical for a viscoelastic solid [73]. At angular frequencies above 200 s^{-1} the inaccuracy of the measured data points increases since these frequencies are close to the limit of the instrument. The behavior of the G' and G'' modulus, as well as the behavior of the complex viscosity η^*, of sample J1 can be observed for the samples J2 to J6, too. The gels show only a weak dependency on the frequency. This behavior is typically for solid-like materials. Hence, the gels behave like viscoelastic solids.

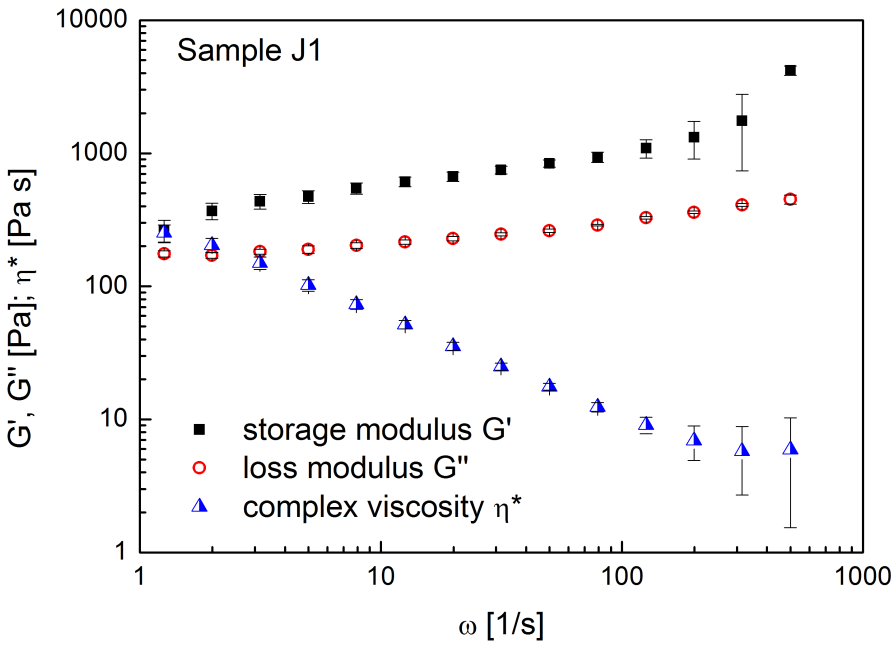

Figure 4.30: *Frequency sweep of sample J1 at 30 °C.*

To compare the elastic modulus of the samples J1 to J5, frequency sweep experiments were carried out again three times for a deformation of 0.2 %. The experimental data were averaged. Figure 4.31 shows the values of the elastic modulus of the samples at different angular frequencies. The G' values of sample J1 and J2 are nearly the same. From J2 to J4 there is a slight decrease of G' indicating a loss in the rigidity of the samples, whereas sample J5 shows higher G' again.

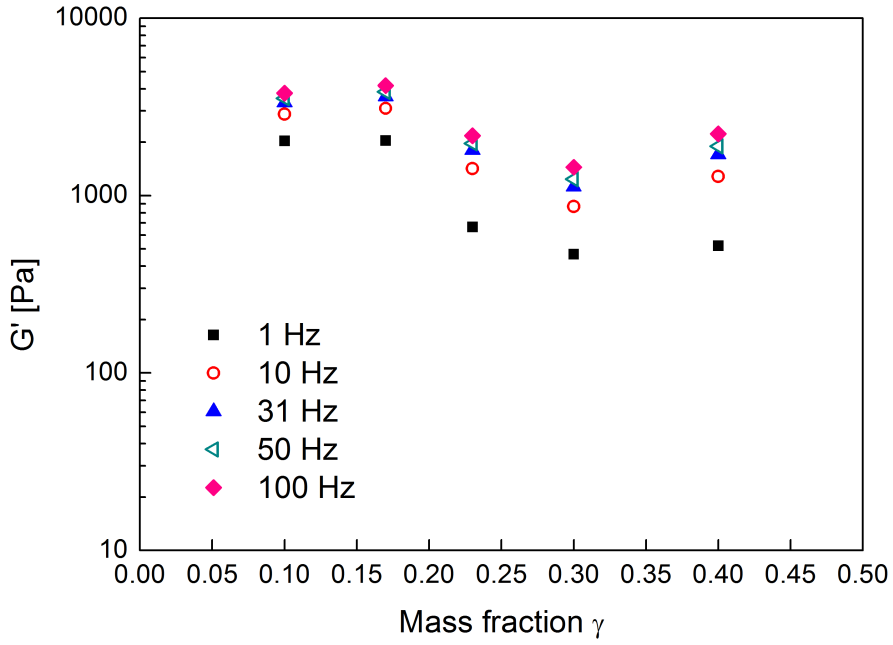

Figure 4.31: *G' modulus at different angular frequencies against the mass fraction γ.*

4.10 Investigation of sample ageing via ^{13}C NMR experiments

The ageing of the gel samples of the J series could be detected visually after 2 to 3 weeks. This ripening process is already known for lyotropic liquid crystalline systems containing fatty alcohols, surfactants and water [2, 74]. According to [74] the process can start directly after the sample preparation.

For the investigation of the ripening process, sample J1 was measured repeatedly over a period of 50 days at constant conditions by ^{13}C-CP MAS NMR spectroscopy. The cross polarization (CP) requires that the observed carbon nuclei have a non-vanishing dipolar coupling with protons. For the investigated sample, this is only the case for solid components which may result from poor mixing or precipitation due to ageing.

Figure 4.32 shows the ^{13}C NMR spectra which were recorded by a ^{13}C-CP MAS experiment at a rotation frequency of 1 kHz. It is assumed that the alkyl chains exist in crystalline aggregates with an all-trans conformation. In this case, the chemical shift of the methyl groups of the alkyl chains is, according to [75], 33.4 ppm. For that reason, the alkyl chain signal is set to that chemical shift. It can be seen in figure 4.32 that there is an increase of the signal intensities of the solid components during the ripening process.

The relative signal intensity of the alkyl chain over time is shown in figure 4.33. The signal intensity increases steadily from the day of preparation to the 16th day after preparation. Then, the intensity increases strongly between day 16 and 20. From day 20 to 50 the solid fraction shows nearly no further increase.

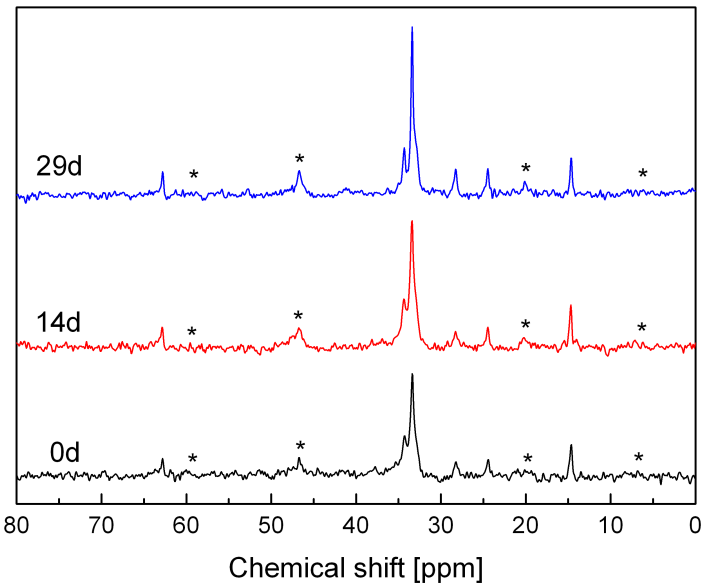

Figure 4.32: *^{13}C-CP MAS NMR spectra recorded at a rotation frequency of 1 kHz directly after the preparation, as well as 14 days and 29 days after the sample preparation. The stars indicate spinning sidebands.*

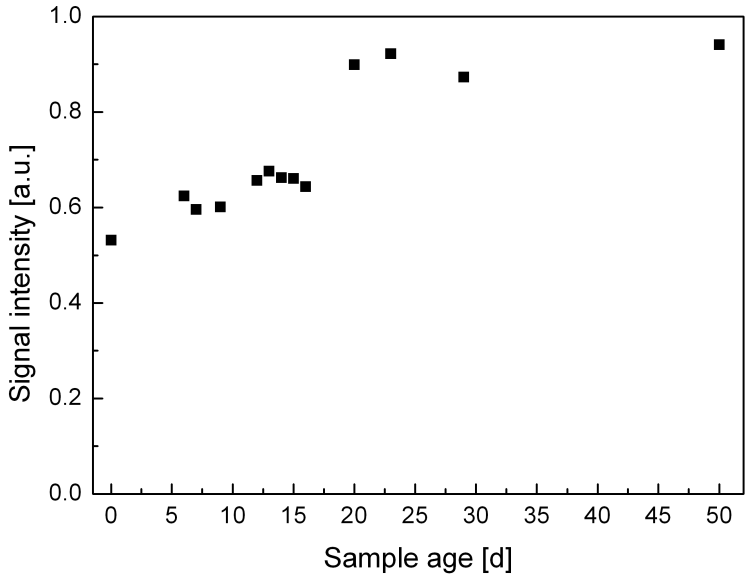

Figure 4.33: *Time-dependent change of the signal intensities of the main peak of the alkyl chains.*

4.11 Influence of processing parameters

For the investigation of the influence of processing parameters, the samples of the J series were prepared in different ways. The stirring rate was reduced from 1000 rpm to 800 rpm for one and 500 rpm for another series of samples. For a third series the solid compounds were heated to 70 °C in closed vials. During this process they were mixed with a stirring rate of 100 rpm. Then the melt was cooled down to room temperature. This melting and cooling process was performed three times before water was added to the solids. After the addition of water, the mixture was stirred for 24 hours at 70 °C at 1000 rpm. All samples of the three series were investigated via ^{1}H NMR spectroscopy. Unfortunately, the samples prepared in new ways delivered the same signal shapes and signal intensities as the samples of the J series. Since nothing changed in the NMR spectra, no further measurements were performed.

4.12 Influence of the alcohol chain length

The alcohol chain length was changed from 16 (cetyl alcohol, CA) to 14 (myristyl alcohol, MA) to investigate the chain length influence on the emulsion properties. The samples were prepared in the same way as the samples of the J series and the same sample compositions were used (see table 4.7). Due to the lower molar mass of MA, the molar ratio of alcohol to SDS changes. In particular for the lower samples of the series n(MA)/n(SDS) is considerably larger than n(CA)/n(SDS).

Table 4.7: *Sample information of the J14 series.*

Sample	J14-1	J14-2	J14-3	J14-4	J14-5
SDS [wt. %]	0.3	0.5	0.7	0.9	1.2
MA [wt. %]	2.7	2.5	2.3	2.1	1.8
D_2O [wt. %]	97.0	97.0	97.0	97.0	97.0
γ	0.10	0.17	0.23	0.30	0.40
n(MA)/n(SDS)	12.10	6.75	4.40	3.13	2.02

Sample	J14-6	J14-7	J14-8	J14-9	J14-10
SDS [wt. %]	1.5	1.8	2.1	2.8	3.00
MA [wt. %]	1.5	1.2	0.9	0.2	0.00
D_2O [wt. %]	97.0	97.0	97.0	97.0	97.0
γ	0.50	0.60	0.70	0.93	1.00
n(MA)/n(SDS)	1.34	0.89	0.58	0.10	0.00

The micellar samples J14-10 and J14-9 are clear and homogeneous. J14-8 shows a phase separation into a clear and turbid phase while samples J14-7 to J14-1 are completely turbid. Samples J14-1 to J14-4 show a significantly higher viscosity than the gel samples of the J series. This is probably due to the higher amount of alcohol molecules.

All samples of the J14 series were investigated via DSC. The experiments were performed in same way as the ones of the J series (chapter 4.3). The results are shown in figure 4.34. The standard deviation of the averaged values is smaller than the used symbol size.

The results are analogous to the DSC results of the J series. The differences

are the lower peak temperatures for the melting points of the mixed crystals and myristyl alcohol as well as the shape of the heating curve of pure MA, which shows only one broad peak at 38.6 °C in the temperature range from 20 °C to 70 °C (added as dotted line to figure 4.34). The DSC curves of pure MA are shown in figure 7.20. Again, it could not be determined if the lower melting point corresponds to pure alcohol or alcohol with small amounts of SDS.

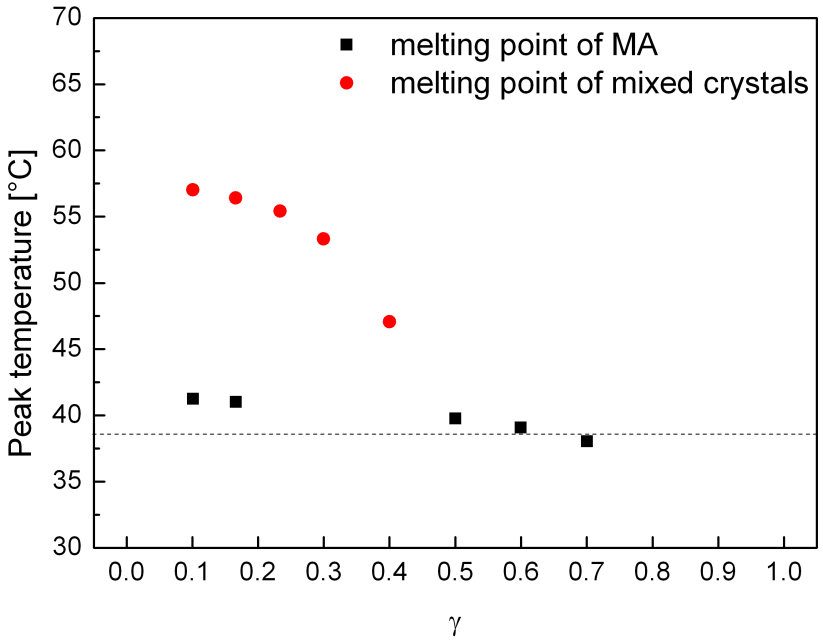

Figure 4.34: *Peak temperature of the DSC signals of the J14 series.*

According to the literature [76, 77], the alkyl chain of 1-tetradecanol exists from 13 °C to 30 °C in the orthorombic (β) state. Above 39 °C the alcohol is molten. Between 30 °C and 39 °C there are different conformational changes of the alkyl chain: orthorhombic to monoclinic ($\beta - \gamma$) at 33 °C, orthorhombic to hexagonal ($\beta - \alpha$) at 38.2 °C and monoclinic to hexagonal ($\gamma - \alpha$) at 38.5 °C.

The reason for the missing $\beta - \gamma$ transition signal of the investigated alcohol sample may be its small enthalpy (1.8 kJ/mol) and/or impurities of the alcohol.

The broad peak of the DSC curve is due to the resolution of the instrument and probably corresponds to the melting signal of MA (38 °C according to the data sheet), the $\beta - \alpha$ transition and the $\gamma - \alpha$ transition.

The ^{1}H NMR spectra of the J14 series at 30 °C are shown in figure 4.35. The spectra of the micellar and coagel samples look like the spectra of the respective samples of the J series (J14-10 like J10, J14-9 like J9, J14-8 like J8, J14-7 like J7, J14-6 like J5). The gel samples of the J14 series show significantly broader peaks with less signal intensity than the peaks of the gel samples of the J series. The peak broadening confirms the visual impression of a higher viscosity of the J14 gels. Probably, the higher viscosity is due to the better chain length matching of surfactant and alcohol, which increases the stability of the aggregates [3, 78].

With increasing temperature, the resolution and the signal intensities of the NMR spectra of the J14 series increase as in the case for the J series. The chemical shift of the water signal (not shown) at 30 °C and 55 °C is not constant for all spectra leading to a change of the chemical shifts of the other signals, since they are referred to the chemical shift of water. The signals of the spectra of the J14 series are shown in more detail in chapter 7.4.2.2.

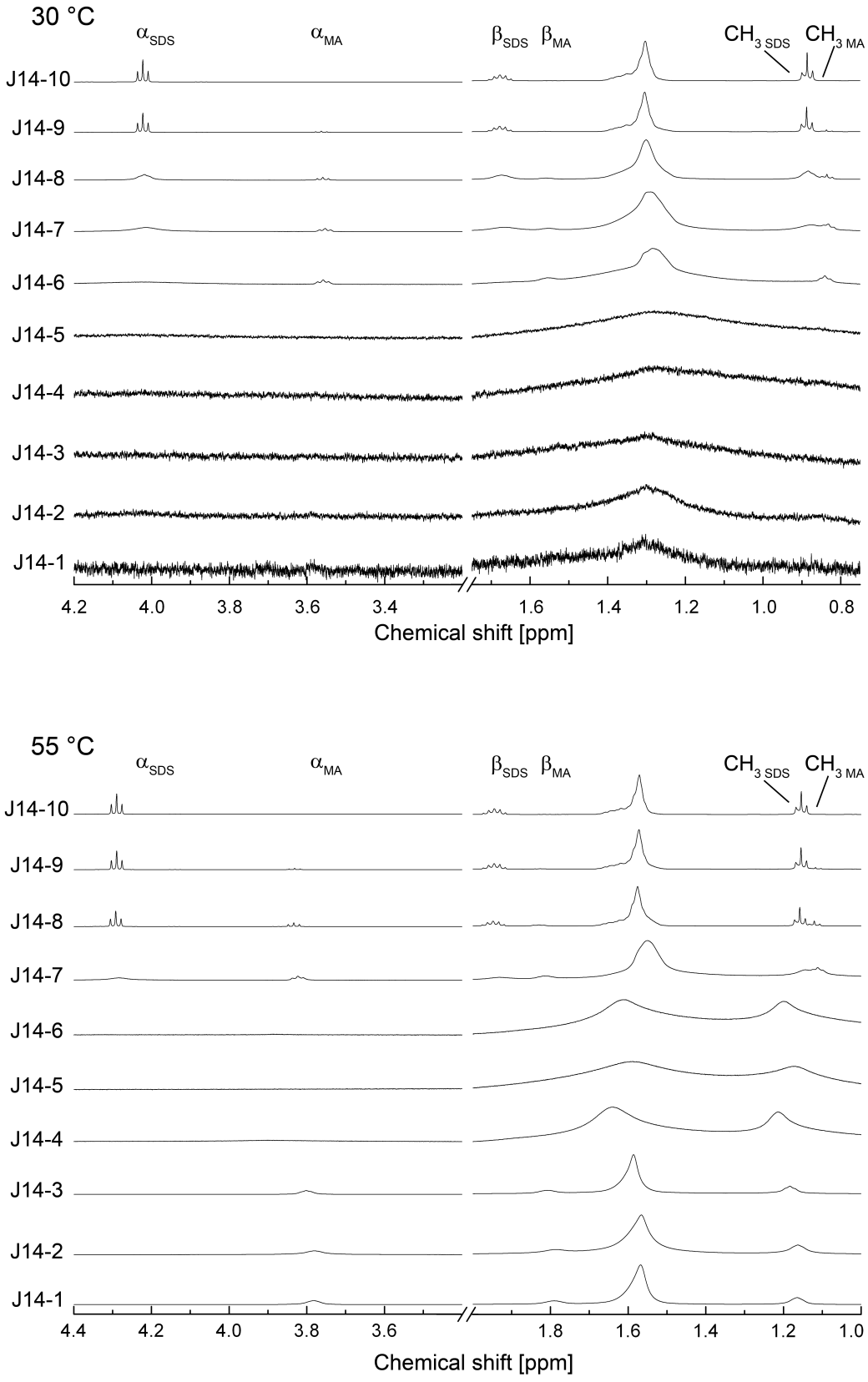

Figure 4.35: *^1H NMR spectra of the J14 series at 30 °C and 55 °C.*

Based on DSC and NMR results the samples of the J14 series can be assigned to the micellar, coagel and gel region. Samples J14-10 and J14-9 are located in the micellar region according to the sharp resolved NMR signals and absence of DSC signals. J14-8 and J14-7 are in the micellar region with additional alcohol crystals. The NMR spectra of these samples still have a high resolution but show no fine structure for the SDS signals. The DSC curves show a melting point signal of myristyl alcohol. The DSC curve of sample J14-6 shows a low melting point peak but no high one for mixed crystals. The occurrance of this peak has been found to be characteristic for the gel region. The NMR spectrum shows a broad alkyl chain signal indicating at least two not completely resolved signals on top of a very broad one. Therefore, sample J14-6 is assigned to the coagel region. The NMR spectra of samples J14-5 to J14-1 yield very broad signals with low intensity and the DSC curves show the melting point signal of mixed crystals at high temperature. Hence, the samples are assigned to the gel region.

4.13 Conclusions and Outlook

By use of ^1H NMR spectroscopy and differential scanning calorimetry, and according to the macroscopic appearance, the samples of the J series could be assigned to the gel, coagel and micellar region of the phase diagram of Goetz and El-Aasser.

Samples J10 and J9 are in the micellar region. They are clear and homogeneous, show no DSC peaks and well resolved NMR signals with well resolved J multiplets. J8 and J7 seem to be micellar solutions when freshly prepared, but show DSC signals, which refer approximately to the melting temperature of CA. The samples phase separate within one week after preparation into a clear and a turbid phase. Below the melting point these samples show NMR signals without fine structure. Above the melting point the spectrum of J8 looks like the spectra of J10 and J9 while the NMR signals of J7 show only a partial fine structure. Samples J6 and J5 are completely turbid and located within the coagel region consisting of a mixture of the gel phase and crystals. The NMR spectra are very broad and the signal shapes suggest that there are two not completely resolved signals. Both samples have a melting peak signal in the DSC curves corresponding to CA or CA with small amounts of SDS. Additionally to this peak, sample J5 shows a peak due to the melting of mixed crystals consisting of SDS and CA. The gel samples J1 to J4 show DSC signals for the melting of mixed crystals and some of them, depending on the age of the sample, a melting point of CA. The samples show a shimmering white turbidity, indicating periodic structures in the range of the wavelength of light. In the NMR spectra at 30 °C they deliver only broad signals with low intensities for the alkyl chain and the CH_3 group of SDS. Above the melting temperature of the mixed crystals, the signal intensity is much higher, the line width smaller and more NMR signals can be detected.

The structure of gel sample J3 was visualized via cryogenic transmission

electron microscopy. The pictures show unilamellar, multilamellar and multivesicular vesicles (UV, MV, MVV). The averaged diameters of the vesicle types are 0.33 μm, 0.43 μm and 0.65 μm for UV, MV and MVV, respectively. The average overall diameter is 0.65 μm and the average distance between two adjacent bilayers of a MV is 61.14 nm. The ratio between the abundance of the vesicle types in total numbers is 638 : 239 : 26.

The coagel J6 shows deformed and broken vesicles as well as plate-like structures. The average diameters are 0.30 μm and 0.45 μm for UV and MV, respectively. No MVV could be found. The average overall diameter is 0.34 μm.

The scattering curves of the very small angle neutron scattering experiments of the gel samples J1 to J4 show a Q^{-2} behavior, which is typical for vesicular structures, whose layers are much smaller than the radius of the core of the vesicle. They show a correlation peak, caused by lamellar structures, which confirms the distance between two adjacent bilayers of the multilamellar vesicles distinguished by cryo TEM analysis. Additionally, a broad shoulder can be seen in the scattering curves referring to the diameter distribution of the vesicles.

The vesicular structures could be confirmed via diffusion NMR spectroscopy, too. The gel and coagel samples yield two diffusion coefficients referring to the isotropic motion of free water and the restricted motion of water molecules trapped in vesicles. The amount of water trapped in vesicles decreases with increasing amount of SDS. That means, that the size of the vesicles or the number of vesicles decreases. Samples J7 to J10 show only the self diffusion coefficient of water.

The rheological amplitude sweep experiments show for samples J1 to J8 that the elastic modulus G' is larger than the loss modulus G'' within the linear viscoelastic range. Hence, the stored energy dominates over the dissipated energy. This behavior is typical for viscoelastic solids or gels. The deformation

at which G' and G'' have the same value decreases with increasing amount of SDS indicating a decrease in the elastic properties.

Additionally, frequency sweep experiments were performed for the gel samples J1 to J4 and the coagel samples J5 and J6. It was found that G' is higher than G'' and increases slightly with increasing frequency. The complex viscosity of the samples decreased with increasing frequency. The decrease of the complex viscosity and the weak dependency of the dynamic moduli on the frequency is typical for solid-like materials.

To investigate the influence of the processing parameters, the stirring rate during the sample preparation was reduced. No changes in the signal shapes and signal intensities could be detected in the ^{1}H NMR spectra of the samples prepared at stirring rates of 800 rpm and 500 rpm. Melting and cooling down the solid compounds three times before adding water and preparing the mixture at a stirring rate of 1000 rpm had no influence on the spectra, too. Since there was no change in the NMR spectra, the samples were not characterized via other methods. Further ideas which could be tried in future are: preparing the samples at a lower temperature, which is still above the melting point of pure cetyl alcohol or using a ultrasonic bath instead of a magnetic mixer or stirring the samples during the cooling process.

Exchanging cetyl alcohol by myristyl alcohol has a large influence on the viscosity of the gel samples. The increased viscosity leads to broadened signals with lower signal intensities in the proton NMR spectra. Using DSC and NMR results, the samples were assigned to the micellar, coagel and gel region. For the two systems large similarities were found.

5 Construction of a ^{1}H rheo NMR shear cell

In the case of the highly diluted SDS/CA/D_2O system, the remaining anisotropy of the water is not sufficient to obtain structural information via ^{2}H NMR spectroscopy. Therefore, *in situ* ^{2}H NMR spectroscopy under shear, which has been applied to lamellar liquid crystals [79, 80], cannot be used in this case. However, proton NMR, which has been shown to be a sensitive probe of changes in the phase structure (see chapter 4.4) can be used to detect shear-induced changes. For this purpose a proton rheo-NMR probe needs to be build. An almost complete proton probe, which was assembled from a Bruker probe kit (by M. Kanlosh, University of Freiburg) was available. To complete the probe the transmitter/receiver coil and the mechanics of the sample/rheo geometry had to be built. The construction of the coil is aggravated by the fact that no information about the electric components used was available. In this chapter the construction of the rf coil and the shear cell is described as well as the adjustment of the probe. First measurements on a thermotropic liquid crystal demonstrate its performance.

5.1 Fundamentals concerning saddle coils

A saddle coil consists of two identical parts, which are wound around a cylinder, which is oriented along the z-direction (parallel to the static magnetic field, see figure 5.1). The magnetic field created by the coil is oriented perpendicular to the cylinder axis. In 1970 Ginsberg and Melchner reported on the optimal geometry of a saddle coil to produce a uniform magnetic field [81]. The optimal coil has an angle Φ of 120.76 ° for a height-diameter-ratio of $h/d = 1.6554$ [81].

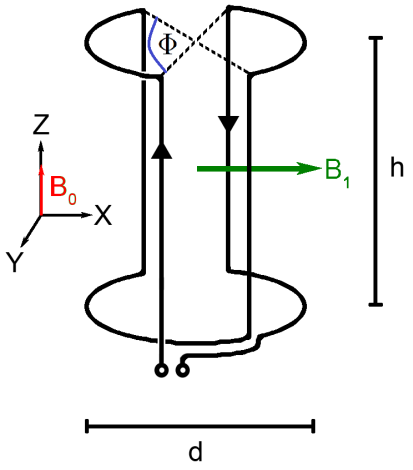

Figure 5.1: *Schematic illustration of a saddle coil.*

According to Salmon et. al [82], the geometry presented by Ginsberg and Melchner yields only a local uniformity of the magnetic field at the coil center. To improve the geometry they calculated three parameters, which depend on the angle Φ, for a simplified model coil with a diameter of 25.6 cm. The calculations were performed for different wire diameters. They assumed in their calculations that the four parallel sections of the coil do not interfere with each other. The calculated parameters are the non-uniformity of the field, which is the root mean square deviation relative to the mean field value, the peak-to-peak homogeneity, which is the difference between maximum and minimum values, expressed in percentage of the field at the coil center, and

the relative uniformity which corresponds to the percentage areas which have a field deviation within ±5 % relative to the center field. From the calculation results that there is no common optimal angle for the three parameters (non-uniformity: 130°, peak-to-peak homogeneity: 135°, relative uniformity: 125°). Additionally, they found that the optimal angle is nearly independent of the wire diameter [82].

5.2 Coil geometry

The space which is available for the coil is limited by the shell of the probe and the position of the homogeneous magnetic field B_0 of the NMR spectrometer. In the present case, the height of the coil is limited to 40 mm. The construction and geometry of the coil are illustrated in figure 5.2 a). To stabilize the coil, it is wound around a hollow cylinder. The wall thickness of the cylinder (2.5 mm) is limited by the diameter of the screws (thread 1.6 mm) used to fix the cylinder to the bottom of the geometry. The lowest turn of the coil begins 6 mm above the cylinder bottom. To simplify the winding of the coil, its geometry is grooved into the wall of the hollow cylinder. The grooves have a depth and width of 1 mm. The distance between the center of the upper cutting and the upper edge of the hollow cylinder is 4 mm. Hence, the resulting coil height is 30 mm. According to Ginsberg and Melchner, the diameter of the coil should be 18.1 mm for an angle of 120.76 °. For such a small diameter, the assumptions of Salmon et al. are not fulfilled. Hence, their criteria for the optimum angle will not be considered.

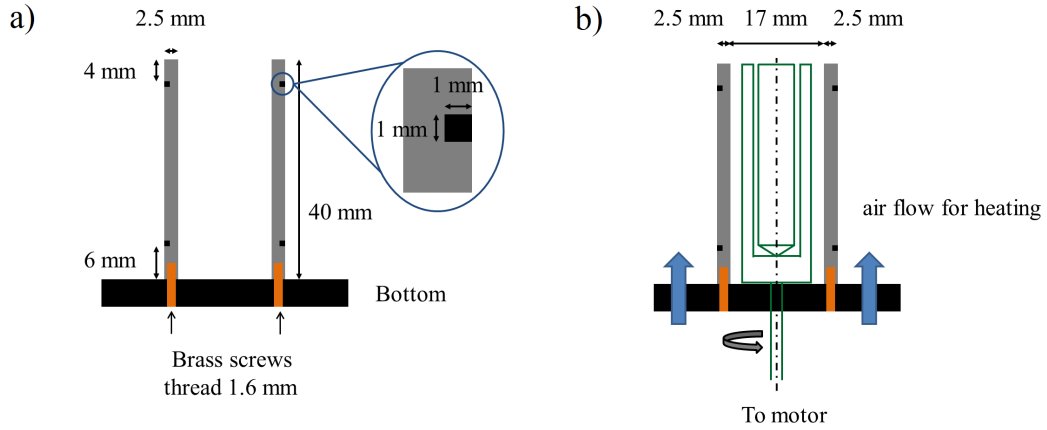

Figure 5.2: *Schematic illustration of the contruction of the coil.*

Since a shear unit shall be installed within the hollow cylinder (see figure 5.2 b)), a gap between the hollow cylinder and the rheo unit must be planned. Furthermore, the rheo unit should have enough space for a sufficiently high

sample volume. For that reason, the inner diameter of the hollow cylinder is set to 17 mm and the outer diameter to 22 mm. Therefore, the diameter of the saddle coil is, depending on the wire thickness, between 20 mm and 22 mm the resulting h/d ratio is 1.5 for 20 mm and 1.36 for 22 mm instead of 1.6554. According to Ginsberg's and Melchner's considerations these ratios are still good for angles between 120.0 and 121.0 ° [81]. Figure 5.3 shows the hollow cylinder, made of glass fiber-reinforced Teflon, with a saddle coil with one winding, which is wound from silver-plated copper wire with a thickness of 1 mm.

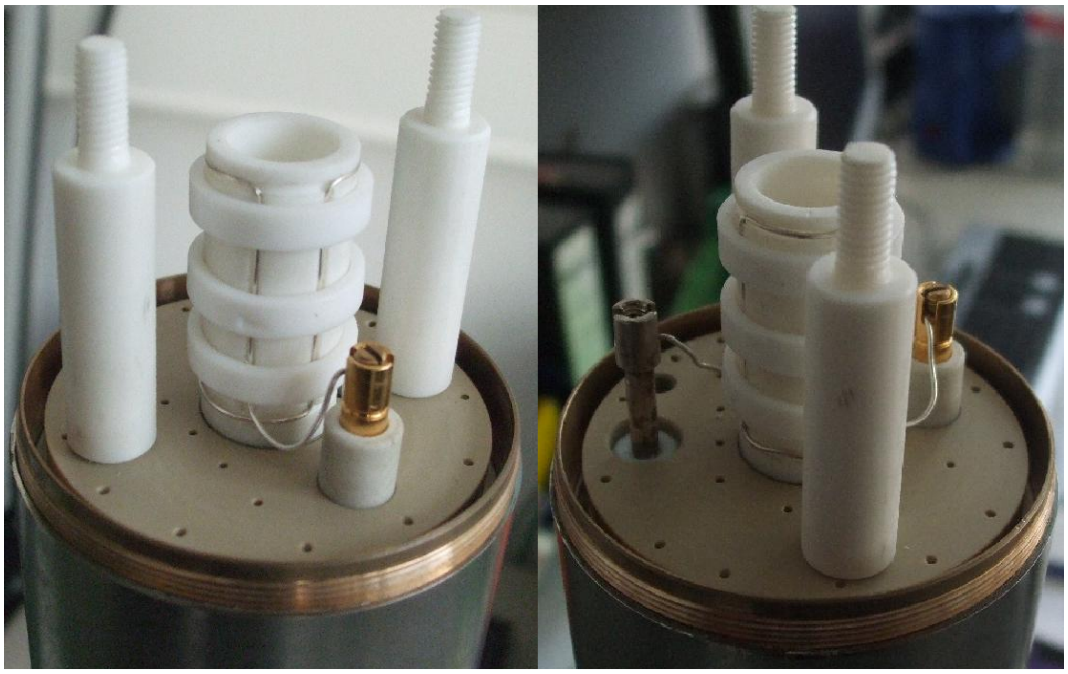

Figure 5.3: *Home-built saddle coil geometry.*

Figure 5.4 shows the resonance signal of the empty ^{1}H-rheo probe, detected by a scalar network analyzer, outside of the NMR magnet at room temperature. Once it has been ensured that the coil can be tuned to the required resonance frequency, the pulse length of the coil has to be adjusted. For the pulse calibration distilled water was used. As pulse sequence, a simple pulse followed by acquisition was chosen. In figure 5.5 the magnitude of the first value of the FID is plotted against the pulse lengths for saddle coils with dif-

ferent wire diameters. If it was possible, the signal intensities were fitted by sine functions. It can be seen that the pulse length of a 90° pulse becomes shorter for increasing wire diameters.

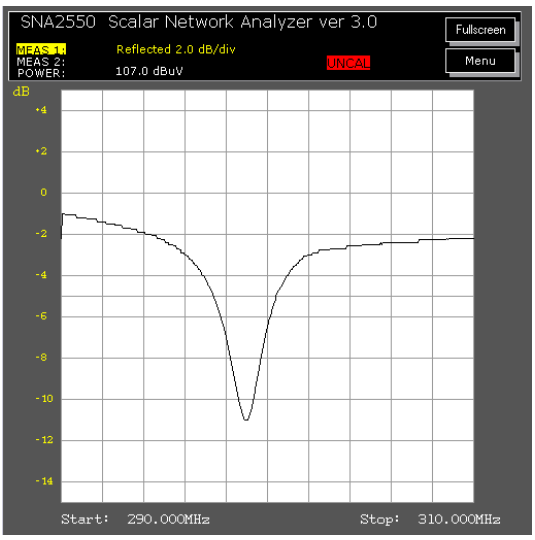

Figure 5.4: *Resonance signal of the ^1H-rheo probe at room temperature at circa 299.8 MHz.*

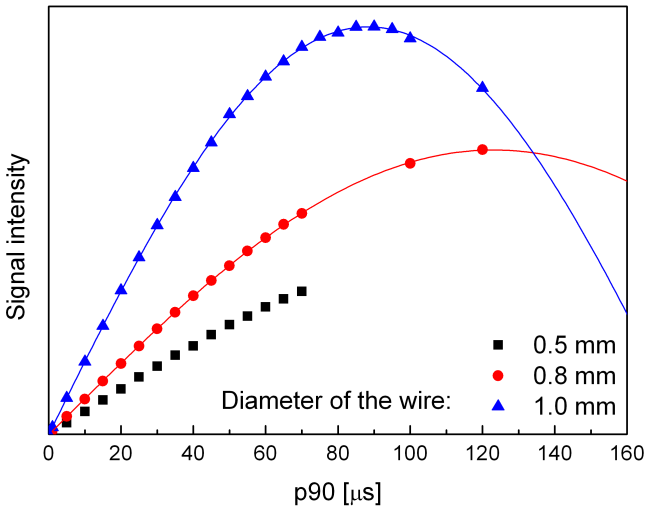

Figure 5.5: *Signal intensities as a function of pulse lengths for three saddle coils with different wire diameters and only one winding.*

The p90 pulse length dependency on the thickness of the wire is due to the skin effect. The skin depth decreases with increasing frequencies [83]. The skin effect leads to an increase of the effective resistance of the conductor. To

compensate the influence of the skin effect the surface of the conductor has to be increased. At high frequencies this can be done using litz wire, which consists of multiple twisted or woven thin insulated strands [83].

To reduce the p90 pulse length litz wire is used. Furthermore, the coil geometry was changed, since the magnetic field homogeneity can be increased strongly at the coil center by an increase of the number of active conductors [84]. Figure 5.6 shows the construction sketch of the improved saddle coil.

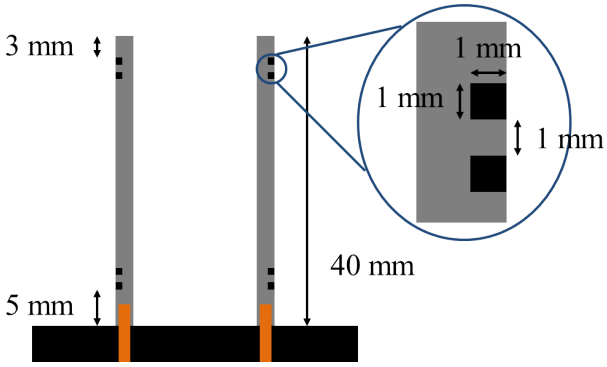

Figure 5.6: *Construction sketch of a saddle coil geometry with two windings.*

The constructed saddle coil geometry with two windings and its pulse length calibration measurements are shown in figure 5.7. Each data point of the two measurement series in figure 5.7, performed on different days, represents the average value of three to five measurements. The error bars illustrate the standard deviation of the mean. The p90 pulse length of the probe is not clearly defined since a plateau of the intensities from 20 to 35 μs is found. For the experiments which will be presented in chapter 5.4 a p90 pulse length of 30 μs was used.

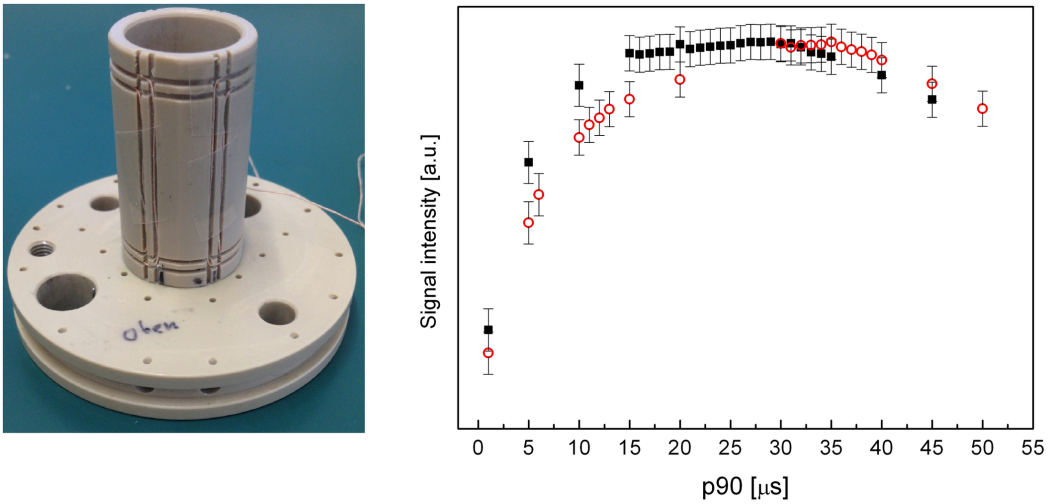

Figure 5.7: *Left: Saddle coil geometry with two windings. Right: Signal intensities as a function of pulse lengths.*

5.3 Rheo geometry

As a first shear unit a conicylinder geometry, which is a combination of the classical couette and a cone-plate geometry, is used. Figure 5.8 shows the rheo elements made of PEEK and a schematic illustration of the rheo unit. The geometry is constructed in a way that the outer cylinder is rotated during the experiments. The inner radius of the shear geometry is $R_i = 5.25$ mm and the external radius is $R_e = 6$ mm. Hence, the ratio of the radii is according to eq. 2.10 $\delta_{CC} = 1.1429$. The angle of the cone is 5° (0.0873 rad).

This shear unit is used as a prototype, since δ_{CC} is larger than 1.0847. Furthermore, the angle of five degree is not in agreement with the construction regulation (eq. 2.15). An angle of $\alpha = 5°$ corresponds to the radii ratio $\delta_{CC} = 1.0914$. As a consequence, the resulting shear rates within the annular and the conical gap will differ from each other. In the case of a rotational speed of 0.83 min^{-1} the shear rate within the annular gap is $\dot{\gamma}_{CC} = 1\ s^{-1}$ and the shear rate within the conical gap is $\dot{\gamma}_{CP} = 0.66\ s^{-1}$.

The final shear unit should have the ratio $\delta_{CC} = 1.0847$. To achieve this ratio R_i becomes enlarged to 5.53 cm. The corresponding angle is $\alpha = 4.648°$. This geometry is currently under construction.

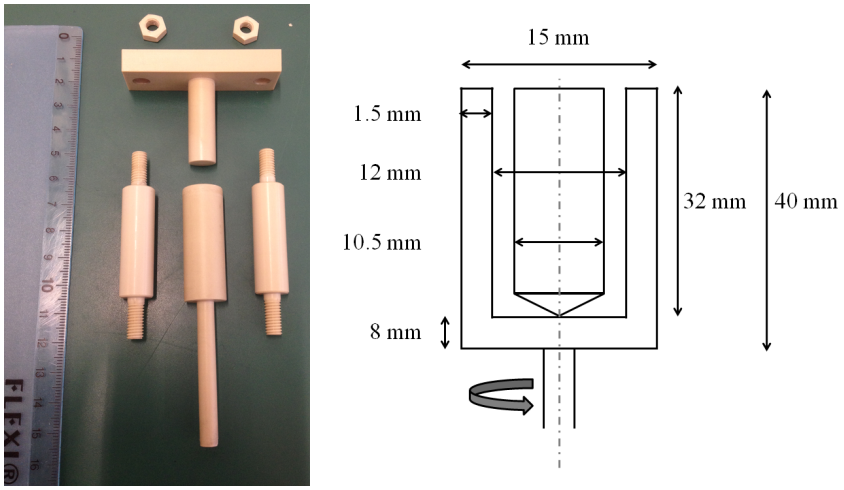

Figure 5.8: *Rheo geometry used for the measurements.*

5.4 Measurements

At first, the resolution of the probe and the background ^{1}H signal from the shear cell have to be determined. For this purpose, proton spectra of distilled water and the empty sample geometry were measured. Figure 5.9 shows the measured spectra.

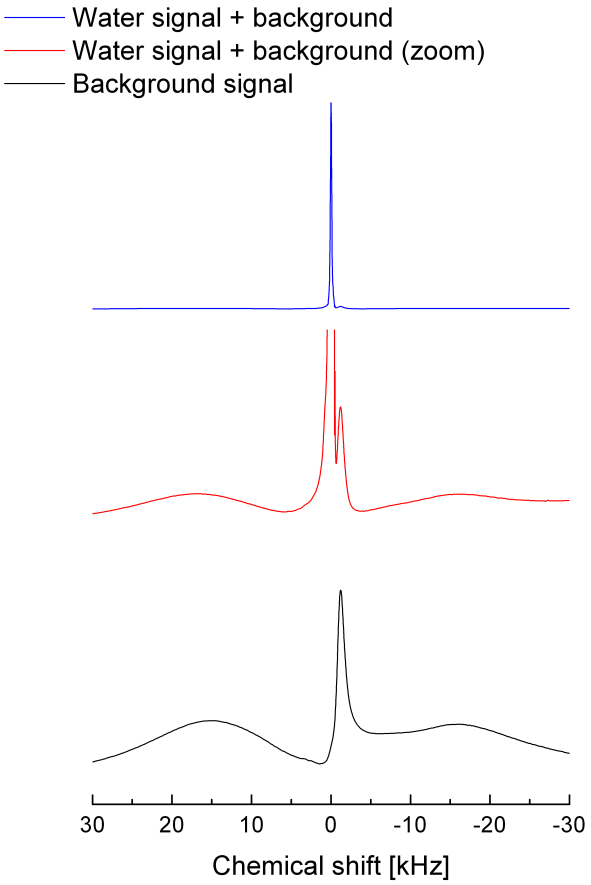

Figure 5.9: *Spectrum of distilled water measured with the new ^1H rheo NMR probe (top, middle). Additionally, the background signal of the probe is measured and illustrated (bottom)*

The empty geometry has a broad doublet with a narrow singlet in the middle as background signal. This background can still be observed in the ^{1}H spectrum of water in addition to the water singlet. The intensity of the background signal is much smaller than the signal of water. Hence, the broad doublet cannot be detected without a zoom and the singlet of the background

signal appears as a small peak close to the water peak in the ^{1}H spectrum of water. The line width of the water singlet is circa 185 Hz.

To check the temperature control of the probe the thermotropic liquid crystalline mixture E7, which shows a phase transition from nematic to isotropic at approximately 61 °C [85], is measured by NMR spectroscopy.

Figure 5.10 illustrates the temperature dependency of the proton spectra of E7. In addition to the background signal of the ^{1}H rheo-NMR probe, spectra within the nematic and isotropic phase, as well as a spectrum of the nematic to isotropic phase transition, are shown. The spectra of the nematic phase show broad signals, which are due to the dipolar interactions in the nematic phase. The doublet, which can be seen in the spectra, proves the alignment of the liquid crystal in the magnetic field. With increasing temperature the line width of the signals and the doublet splitting decrease. This behavior is due to a decrease of the molecular order. In the isotropic phase, characteristic sharp peaks can be detected.

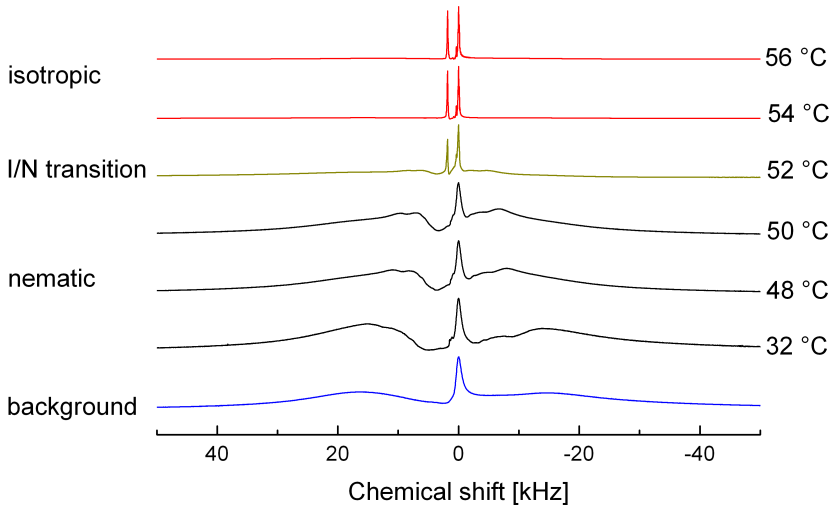

Figure 5.10: *Temperature dependence of the ^{1}H NMR spectra of the liquid crystal composition E7.*

All spectra are normalized by dividing the intensities by the highest one. For the spectra of the nematic phase, the sharp peak of the background signal obtains the highest signal intensity. In the isotropic phase, the height of the background signal is very small in comparison to the one of E7 and is no longer seen.

Figure 5.11 shows the isotropic spectrum of E7 at 56 °C and figure 5.12 the temperature dependent change of the outer splitting of the nematic doublet.

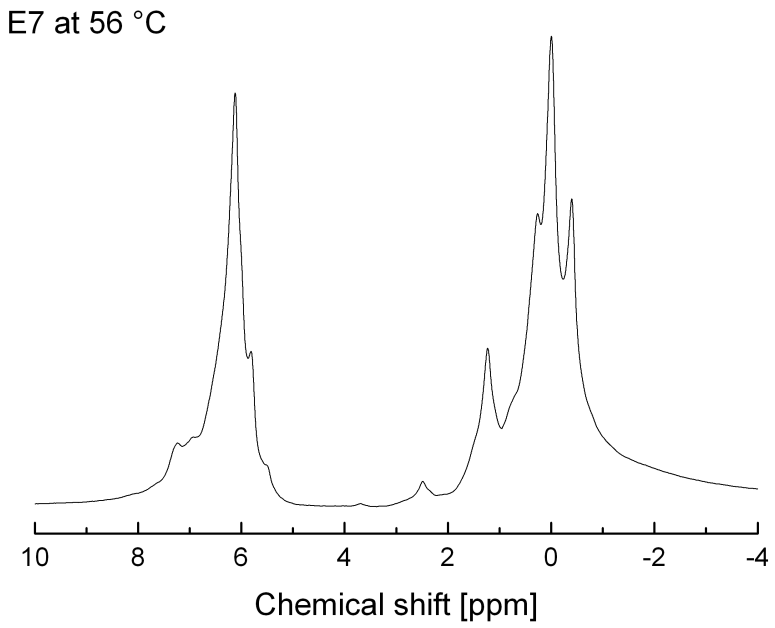

Figure 5.11: *Isotropic proton NMR spectra of E7 at 56 °C*

According to the NMR spectra, the nematic to isotropic phase transition takes place between 52 °C and 54 °C. Hence, the phase transition temperature is lower than the ones described in the literature (61 °C, [85]). Probably, this reduction is due to impurities resulting from lubricants used during the production of the shear cell. Furthermore, the small gap between the hollow cylinder of the coil and the shear cell (see fig. 5.2 b)) may lead to partial thermal insulation. Hence, the temperature within the shear cell might be lower than the temperature measured with the sensor outside of the coil.

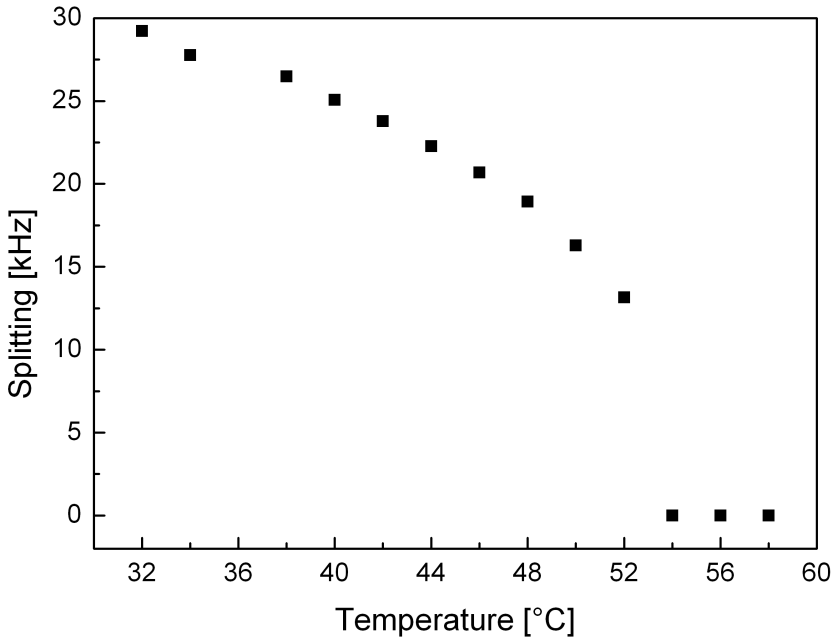

Figure 5.12: *Temperature dependent change of the proton spectra splitting of E7.*

Furthermore, the micellar solution J9 and the gel sample J1 were measured with the new probe. Figure 5.13 shows the high resolution proton spectra (black) and the spectra obtained by the proton rheo probe (red) at 40 °C. The peak assignment is analogous to figures 4.5 and 4.6. Despite the lower resolution of the proton spectra of the ^{1}H rheo probe, different signals can be recognized and assigned. Nevertheless, the high resolution spectra are very helpful for the peak assignment.

The temperature dependent increase of the signal intensity and resolution of the proton spectra of sample J1 is shown in figure 5.14. It can be seen that the ratio of HDO to the signal at 1–2 ppm, composed of alkylchain, β- and CH_3 signals, decreases strongly above the melting point of the mixed crystals, which occur in sample J1 (see fig. 4.3, DSC results). This behavior is already described in section 4.4.

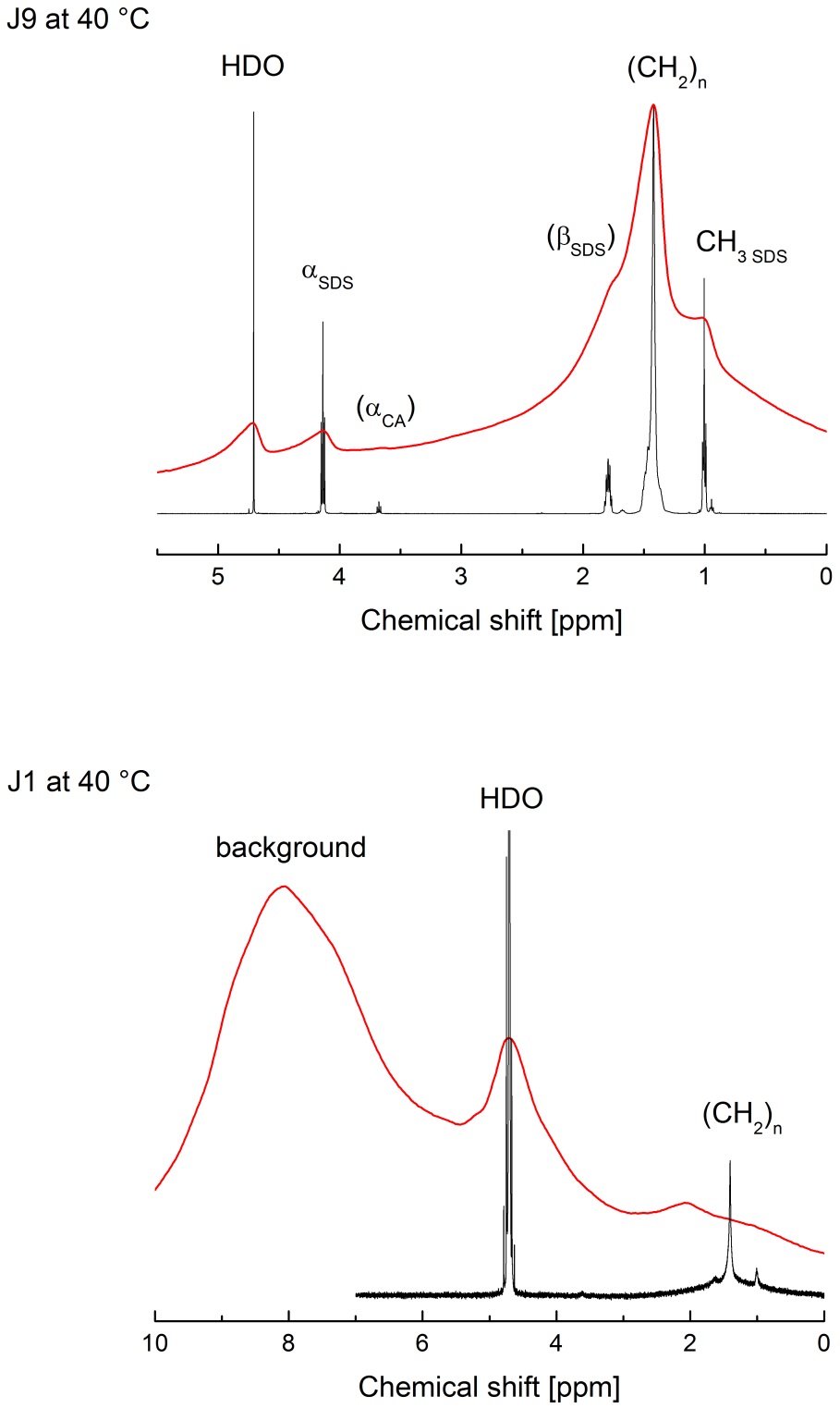

Figure 5.13: *Comparison of the spectra of samples J9 and J1 measured with the new proton rheo probe and the high resolution spectra.*

Next, sample J1 is investigated at a shear rate of $\dot{\gamma}_{\mathrm{cc}} = 1\ \mathrm{s}^{-1}$ within the annular gap and $\dot{\gamma}_{\mathrm{cp}} = 0.66\ \mathrm{s}^{-1}$ within the conical gap. However, no changes of the proton spectra could be found during eight hours of shearing.

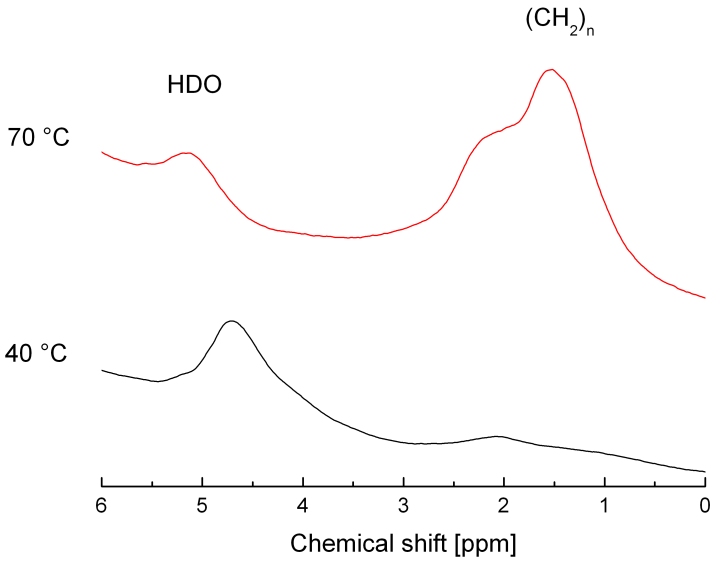

Figure 5.14: *Temperature dependency of sample J1.*

5.5 Conclusions and Outlook

In this chapter the construction of the saddle coil and shear cell geometry were described. Based on the proton spectra of the liquid crystal mixture E7, micellar sample J9 and gel sample J1 it was shown that the probe works.

However, there are a few things that should be revised and tested. For an enhanced temperature control, holes should be bored in the hollow cylinder of the coil, so that there is an exchange of air between the gap between hollow cylinder and shear cell and the volume outside of the gap. Furthermore, the shear cell which is under construction at the moment should be installed. Then, the possibility of subtracting the background signal from the spectra, which is not trivial because it requires proper phasing of the spectra, should be explored. Besides, a system with known shear-induced changes of orientation or structures can be investigated for further testing of rheo-NMR with protons. For example, a homogeneous lamellar sample could be investigated under shear. The resulting alignment of the lamellar aggregates should have an influence on the line width of the signals of the proton spectra.

6 Summary

The investigation of the surfactant/water system SDS/D_2O has shown, that the splittings of the α-CH_2 groups of the proton spectra are concentration dependent. This dependency can be explained by conformational changes. However, the temperature dependency of the splittings of the α-CH_2 and CH_3 groups of the SDS/D_2O and CTAB/D_2O systems close to the phase transition from the micellar region to a lyotropic liquid crystalline mesophase seems not to be related to a change of the J coupling. Probably the splitting is influenced by a temperature-dependent direct dipole-dipole coupling caused by an increasing order of larger aggregates and/or an increasing viscosity of the samples.

Furthermore, it was found that the relative change of the chemical shift $\Delta\delta$ of the α-CH_2 and CH_3 groups of SDS proceeds in opposite directions at concentrations between the cmc and approximately 2 wt. %. Above 2 wt. % both $\Delta\delta$ are shifted in the same direction. The behavior of the relative changes of the chemical shift was partially explained by influences of the chemical environment and conformational changes of the α-CH_2 group. In the case of CTAB the α-CH_2 and the terminal CH_3 group show shifts of the same sign over the full concentration range as soon as micellization starts.

By addition of cetyl alcohol to the SDS/D_2O system a gel building ternary system was created. A series of samples containing a total amount of 3 wt. % SDS and CA at varying SDS/CA ratio was investigated during my PhD studies. Based on the macroscopic appearance of the samples as well as DSC and proton NMR measurements the samples were assigned to the existing phase diagram. Gel samples were found for an alcohol amount higher than 2 wt. %.

The structure of one of the gel samples was visualized via cryo-TEM. It was found that the gels consist of uni- and multilamellar vesicles with the most frequent diameter between 0.1 μm and 0.9 μm. The average diameter of all vesicle types is 0.37 μm and the averaged distance between two adjacent bilayers of a multilamellar vesicle is 61.1 nm.

To confirm the sizes of the vesicles, V-SANS experiments of the gel samples were performed. All of the obtained scattering curves were in agreement with the results of the cryo-TEM analysis.

Additionally, the existence of vesicular structures is consistent with the two diffusion coefficients of water, which were found via pulsed gradient spin echo NMR experiments, representing the isotropic motion of free water and the restricted motion of water molecules trapped in vesicles.

By rheological measurements of the samples J1 to J8 it was found that the elastic modulus G' is larger than the loss modulus G'' within the linear viscoelastic regime. Hence, the stored energy dominates over the dissipated energy which is a typical behavior of viscoelastic solids or gels. Besides, the required deformation for breaking down the structure of the samples decreases with increasing amount of SDS. The complex viscosity of the samples, determined via frequency sweep experiments, decreased with increasing frequency. The decrease of the complex viscosity and the weak dependency of the dynamic moduli on the frequency is typical of solid-like materials. Hence, the behavior of the gel samples is similar to the one of solids.

The investigation of small changes of the sample preparation delivered no changes in the NMR spectra. For that reason no further methods were used for sample characterization.

Furthermore, the alcohol of the SDS/CA/D_2O system was changed from $C_{16}OH$ to $C_{14}OH$. The results of the studies on this system showed large similarities to the ones of the SDS/CA/D_2O system.

Moreover, the construction of a proton rheo-NMR probe was described. In first test measurements proton spectra of the thermotropic liquid crystal mixture E7, of the micellar sample J9 and of the gel sample J1 were obtained.

7 Appendix

7.1 Materials

Sodium dodecyl sulfate (SDS, 99% pure), hexadecyltrimethylammonium bromide (CTAB, purity $\geq$ 99%), tetradecanol (MA, purity $\geq$ 99%) and tetrachloroethane (purity $\geq$ 99.8%) were purchased from Sigma Aldrich and hexadecanol (CA, purity $\geq$ 95%) from Carl Roth KG. D_2O (99% pure, Cambridge Isotope Laboratories) was purchased from Buchem BV and didodecyldimethylammonium bromide (DDAB, purity $\geq$ 98%) from Fluka Chemie. The liquid crystal composition E7 was purchased from Merck, chloroform-d_1 (purity $\geq$ 99.8%) from Deutero GmbH and hexa-ethyleneglycol mono n-dodecyl ether ($C_{12}E_6$) from Nikko Chemicals. All chemicals were used as received.

7.2 Instruments and Methods

7.2.1 DSC

The DSC thermograms were obtained by using a Perkin Elmer differential scanning calorimeter (Model Pyris 1). All samples were hermetically sealed in aluminum pans. Before and after the DSC measurement the pans were tared in order to check if water evaporation had occurred. Scans were recorded with a heating rate of 5 K/min from 20 to 70 °C. The peak temperature was determined by the intersection of the tangents of the DSC peak as shown in figure 7.1.

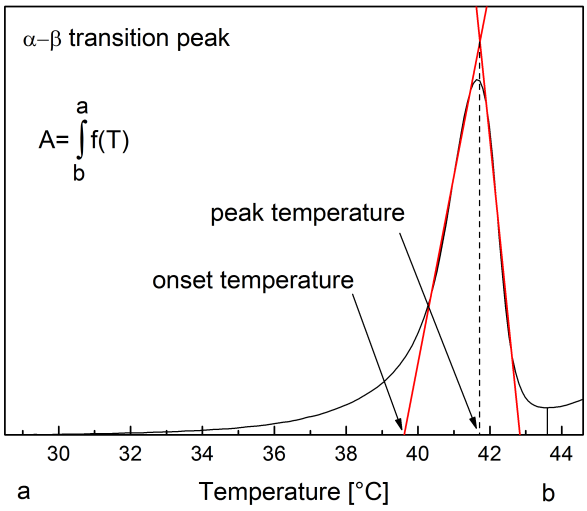

Figure 7.1: *Illustration of the determination of the peak temperature of a DSC signal.*

7.2.2 NMR

For the NMR measurements different spectrometers were used. The standard proton NMR spectra were recorded using a Bruker Avance 500 spectrometer. The standard zg30 pulse sequence of Bruker was used. The diffusion NMR experiments were performed on a Bruker Avance II 200 spectrometer using a PGSE sequence described in chapter 2.2. For the solid state and proton rheo spectra a Tecmag Apollo NMR spectrometer with a 7.05 T magnet of the company Oxford was used. This spectrometer has in contrast to the other ones a wide-bore magnet.

7.2.3 Cryo-TEM

The description of the used instruments and sample preparation is taken from the research report written by Dr. Frank Polzer from February 2012.

> "The TEM specimens were vitrified by plunging the samples into liquid ethane using an automated plunge freezer (Vitrobot Mark IV, FEI Deutschland GmbH, Frankfurt a. M., Germany). The carbon coated copper grids have been pre-treated by 10 seconds of glow discharge. Approximately 5 μl of solution on a TEM copper grid with lacey carbon support film (200 mesh, Science Services,

Munich, Germany). The liquid was blotted 4 times in a row with a filter paper after 30 seconds applying a blot force of 0 for 1 second. No wait time or drain time have been used. The specimen was inserted into a pre-cooled high tilt cryo transfer sample holder (Gatan 914, Gatan, Eching, Germany) and transferred into a JEOL JEM-2100 with a LaB6 cathode (JEOL GmbH, Eching, Germany). The TEM was operated at an acceleration voltage of 200 kV. All images were recorded digitally by a bottom-mounted 4k·4k CMOS camera system using low dose conditions (TemCam-F416, TVIPS, Gauting, Germany) and processed with a digital imaging processing system (EM-Menu 4.0, TVIPS, Gauting, Germany). Sample J3 was extremely difficult in its preparation due to its high viscosity. Several blottings were necessary to yield a film that was transparent to electrons."

7.2.4 SANS

The V-SANS experiments (very small neutron scattering) have been performed with the JCNS (Jülich Centre of Neutron Science)-instrument KWS-3 at FRM II research reactor in Garching/Munich. Both sample-detector distances (9.5 m and 1.2 m) have been used, bridging more than two orders of magnitude in Q-range with a corresponding size scale between 20 nm and several micrometers. The wavelength was $\lambda = 12.8$ Å. Detailed information about the instrument can be found in the publication of G. Goerigk and Z. Varga [66].

For the reduction of the raw data the software qtiKWS [86] was used. Corrections for the empty cell, the background noise and the detector sensitivity were included in the data reduction. The calibration of the scattering data (unit: cm^{-1}) is based on the direct neutron beam [66, 87, 88]. The absolute differential scattering cross section can be calculated by equation 7.1 according to [66].

$$\frac{d\sum}{d\Omega}(Q)^{s,sb} = \frac{L^2}{a^2 \cdot T^{s,sb} \cdot h^{s,sb} \cdot \langle I \rangle^{ec-db}} \cdot \left(\left[I(Q)^{s,sb} - I(Q)^{dc} \right] - T^{s,sb} \left[I(Q)^{ec} - I(Q)^{dc} \right] \right) \tag{7.1}$$

The indices db, s, sb, ec, a, dc and eb refer to direct beam, sample, sample background, empty cell, pixel size, dark current and electronic background. The parameters T, h, $I(q)$, and L correspond to transmission, sample thick-

ness, scattered intensity, and sample-detector distance. The incoming flux $\langle I \rangle^{ec-db}$, is determined by the direct beam measurement of the empty cell. After the calculation of $d\sum/d\Omega\,(q)$ the absolute differential scattering cross section was averaged radially. To obtain the absolute cross section $\Delta\left(d\sum/d\Omega\right)(q)$ the cross section of the sample background was subtracted from the cross section of the sample.

$$\Delta\left(\frac{d\sum}{d\Omega}\right) = \left(\frac{d\sum}{d\Omega}\right)^{s} - \left(\frac{d\sum}{d\Omega}\right)^{sb} \tag{7.2}$$

The obtained scattering curves of the two sample-detector distances were merged by qtiKWS.

7.2.5 SAXS

The X-ray diffraction measurements were carried out with a Bruker AXS D8 Advance diffractometer by using Cu-K_α radiation (40 kV, 40 mA). The step size for low-angle measurements ($\theta < 5°$) was $2\theta = 0.0075°$ with a counting time of 3 s per step.

7.2.6 Rheometer

For the rheological measurements an Anton Paar MCR 5.01 rheometer with a cone and plate geometry was used. The used geometry had a diameter of 24.949 mm, an angle of 0.993°, and a truncation of 49 μm.

7.3 Sample preparation of aqueous surfactant mixtures

The samples were prepared by weighing the desired amounts of surfactant and water into vials. Samples below 20 wt. % SDS and the samples below 10 wt. % CTAB were prepared by mixing the components at 70 °C at a stirring rate of 1000 rpm for 24 hours. For the preparation of the samples between

20 wt. % and 35 wt. % SDS and the samples with a concentration higher than 9 wt. % CTAB an Intelli-Mixer RM-2 bought from LTF Labortechnik running on program b1 with 95 rpm at 50 °C was used. Program b1 is a combination of a continuous rotation along one axis and a continuous small amplitude vortexing.

7.4 Measured data

7.4.1 DSC curves

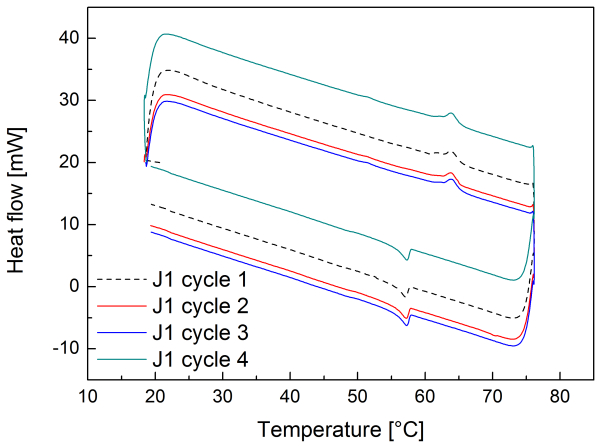

Figure 7.2: *Four measurements of a pan of the stock mixture of sample J1 recorded at a heating rate of 5 K/min in the temperature range from 20 °C to 70 °C.*

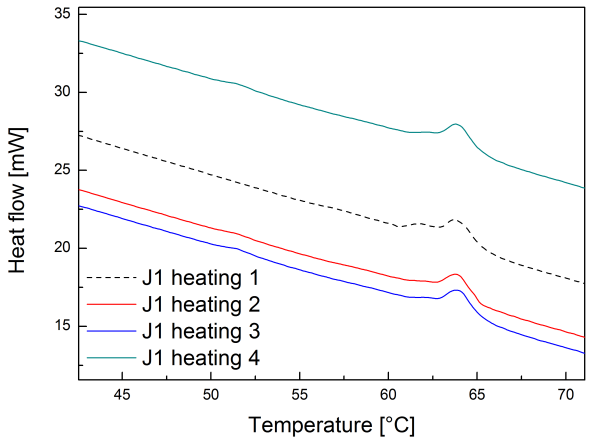

Figure 7.3: *Enlarged DSC signals of the heating process of sample J1.*

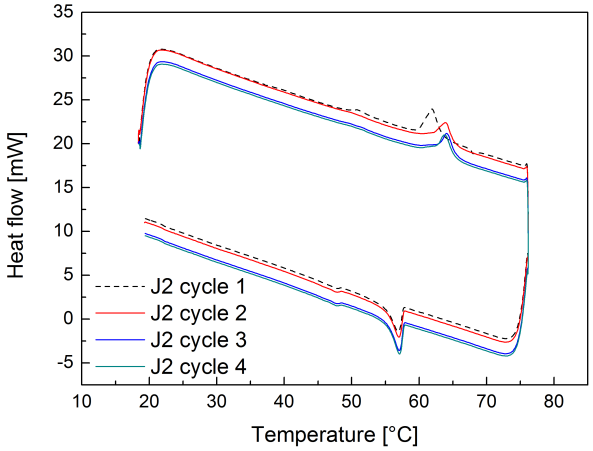

Figure 7.4: *Four measurements of a pan of the stock mixture of sample J2 recorded at a heating rate of 5 K/min in the temperature range from 20 °C to 70 °C.*

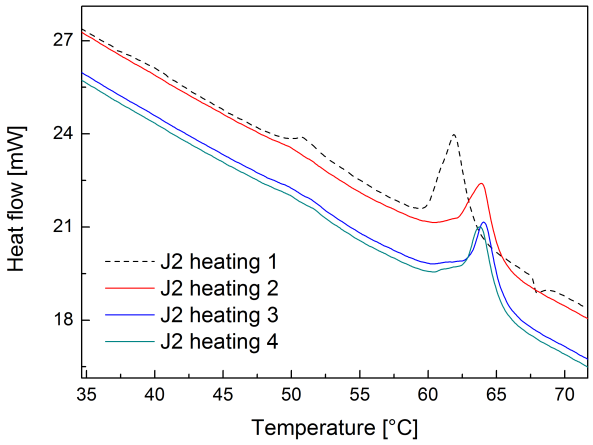

Figure 7.5: *Enlarged DSC signals of the heating process of sample J2.*

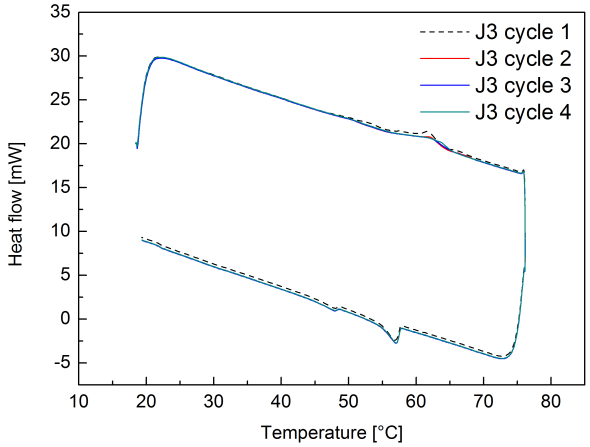

Figure 7.6: *Four measurements of a pan of the stock mixture of sample J3 recorded at a heating rate of 5 K/min in the temperature range from 20 °C to 70 °C.*

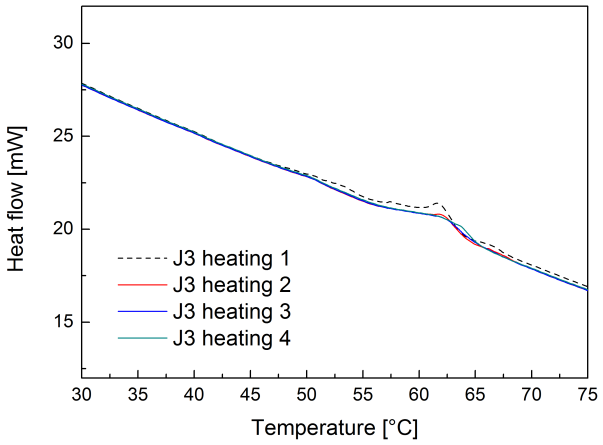

Figure 7.7: *Enlarged DSC signals of the heating process of sample J3.*

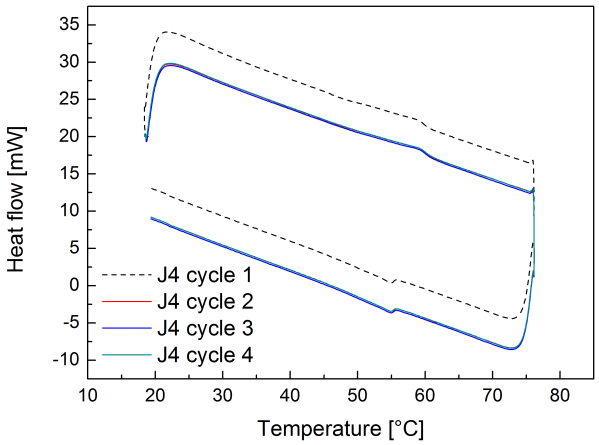

Figure 7.8: *Four measurements of a pan of the stock mixture of sample J4 recorded at a heating rate of 5 K/min in the temperature range from 20 °C to 70 °C.*

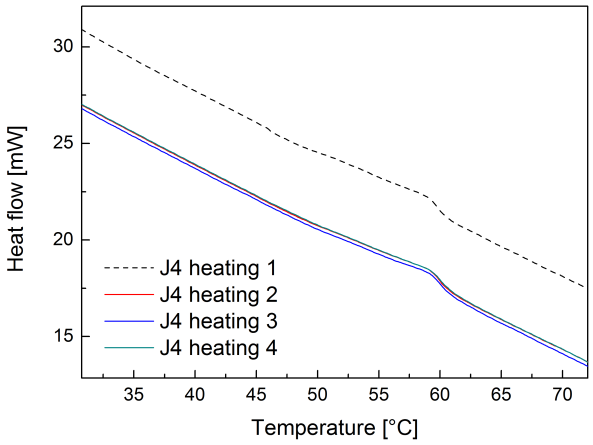

Figure 7.9: *Enlarged DSC signals of the heating process of sample J4.*

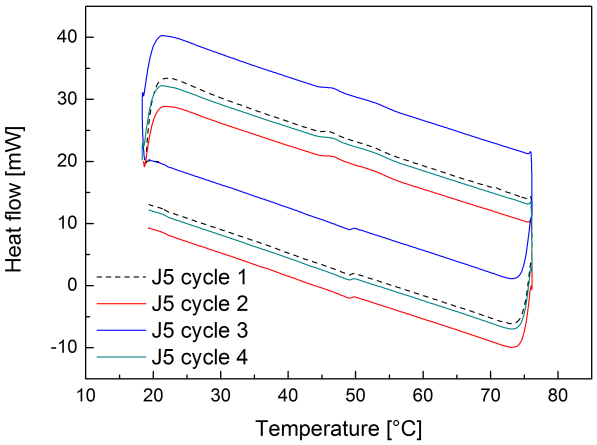

Figure 7.10: *Four measurements of a pan of the stock mixture of sample J5 recorded at a heating rate of 5 K/min in the temperature range from 20 °C to 70 °C.*

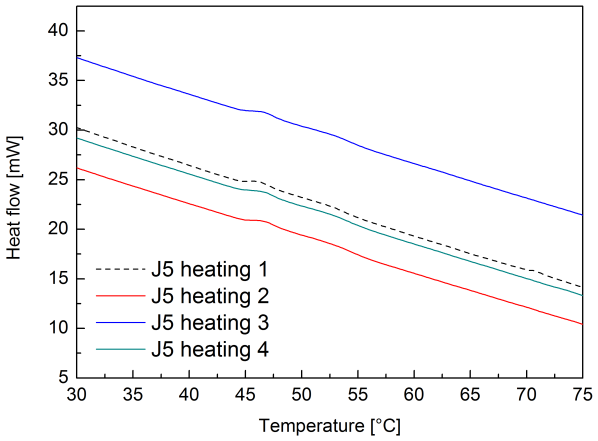

Figure 7.11: *Enlarged DSC signals of the heating process of sample J5.*

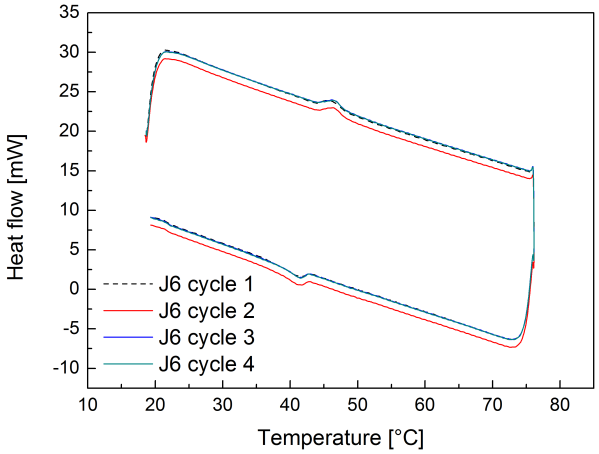

Figure 7.12: *Four measurements of a pan of the stock mixture of sample J6 recorded at a heating rate of 5 K/min in the temperature range from 20 °C to 70 °C.*

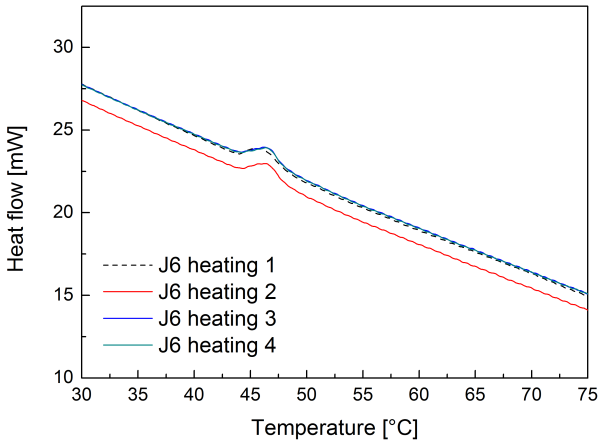

Figure 7.13: *Enlarged DSC signals of the heating process of sample J6.*

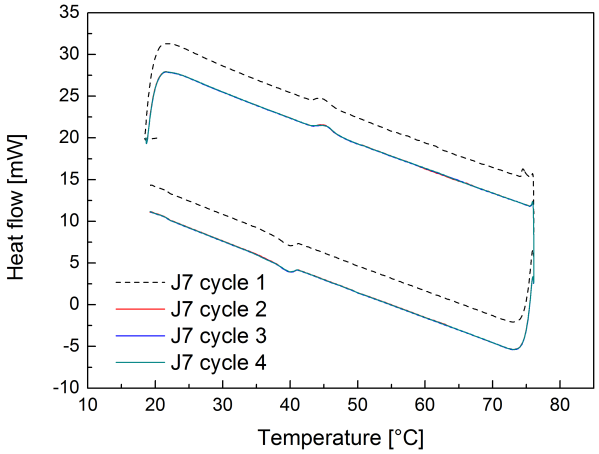

Figure 7.14: *Four measurements of a pan of the stock mixture of sample J7 recorded at a heating rate of 5 K/min in the temperature range from 20 °C to 70 °C.*

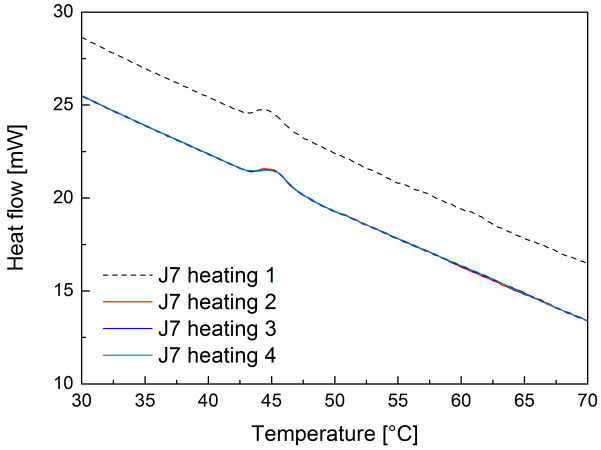

Figure 7.15: *Enlarged DSC signals of the heating process of sample J7.*

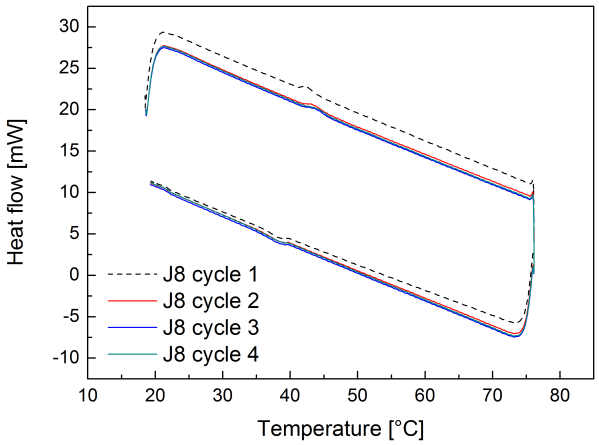

Figure 7.16: *Four measurements of a pan of the stock mixture of sample J8 recorded at a heating rate of 5 K/min in the temperature range from 20 °C to 70 °C.*

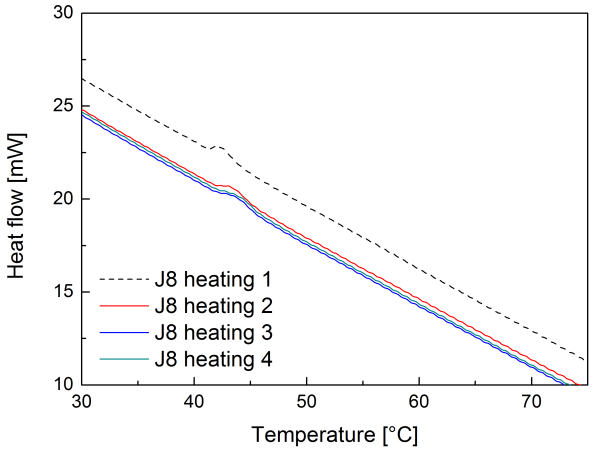

Figure 7.17: *Enlarged DSC signals of the heating process of sample J8.*

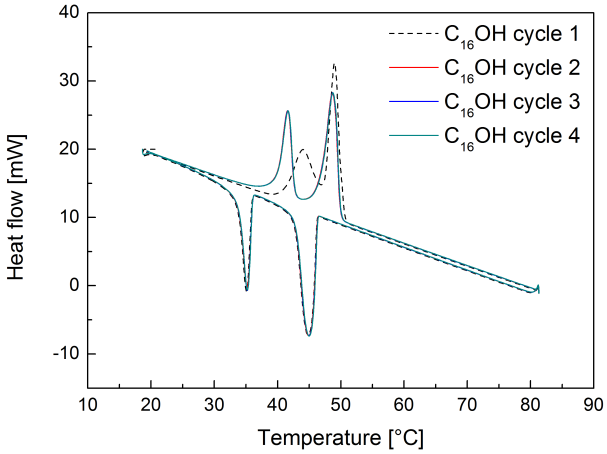

Figure 7.18: *Four measurements of a pan of cetyl alcohol recorded at a heating rate of 5 K/min in the temperature range from 20 °C to 70 °C.*

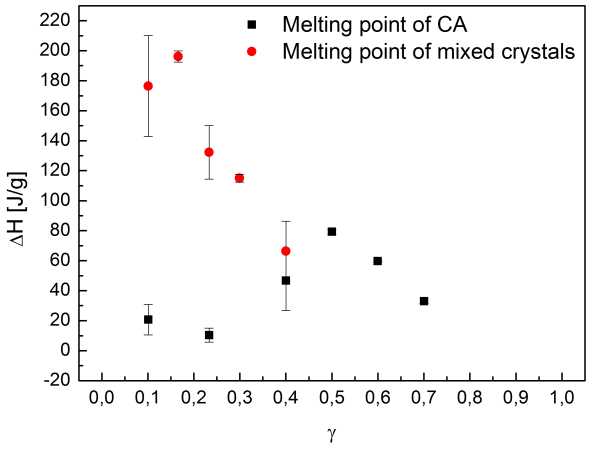

Figure 7.19: *Enthalpies of the melting point signals of CA and mixed crystals of the J series. The error bars represent the standard deviation.*

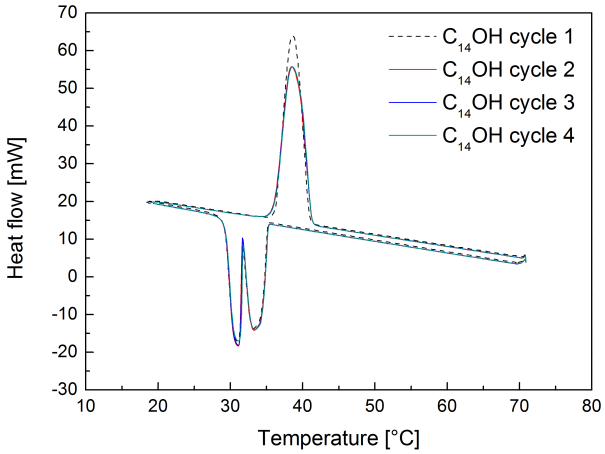

Figure 7.20: *Four measurements of a pan of myristyl alcohol recorded at a heating rate of 5 K/min in the temperature range from 20 °C to 70 °C.*

7.4.2 ^{1}H NMR spectra

7.4.2.1 Enlarged signals of the J1 to J10 spectra at 30 °C and 70 °C

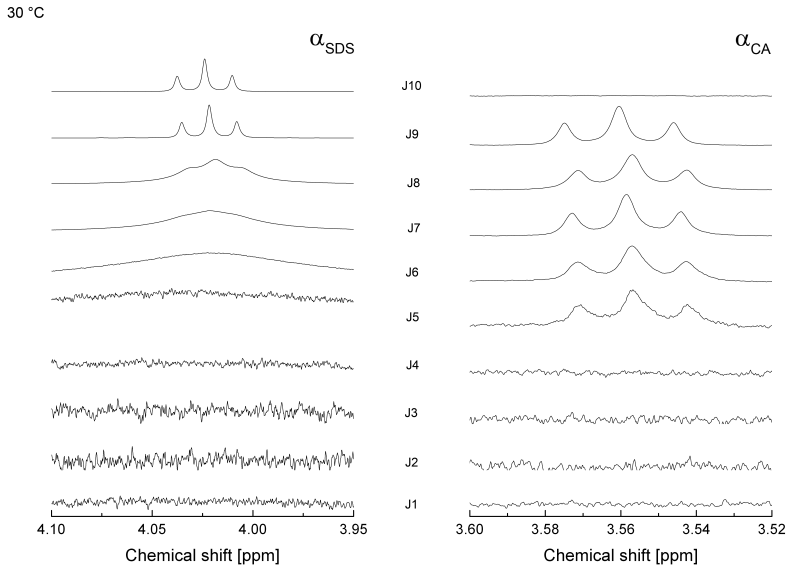

Figure 7.21: *Enlarged signals of the α-CH_2 groups of the J samples at 30 °C.*

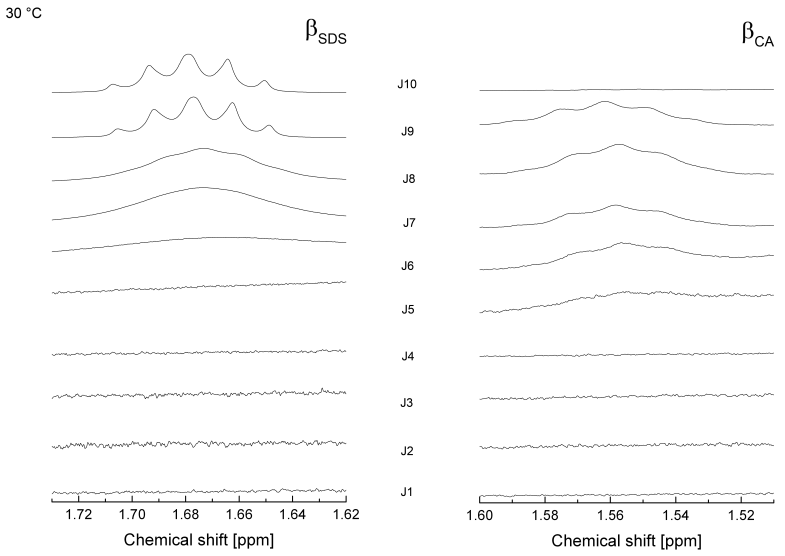

Figure 7.22: *Enlarged signals of the β-CH_2 groups of the J samples at 30 °C.*

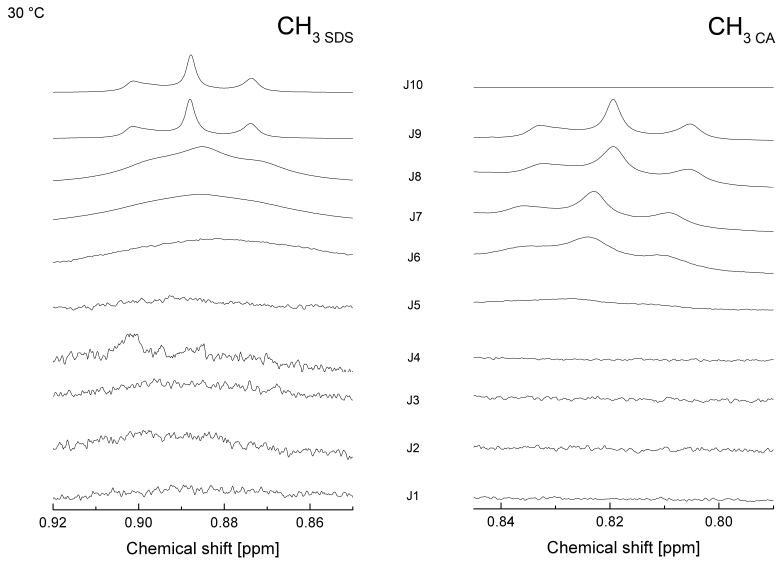

Figure 7.23: *Enlarged signals of the CH_3 groups of the J samples at 30 ˚C.*

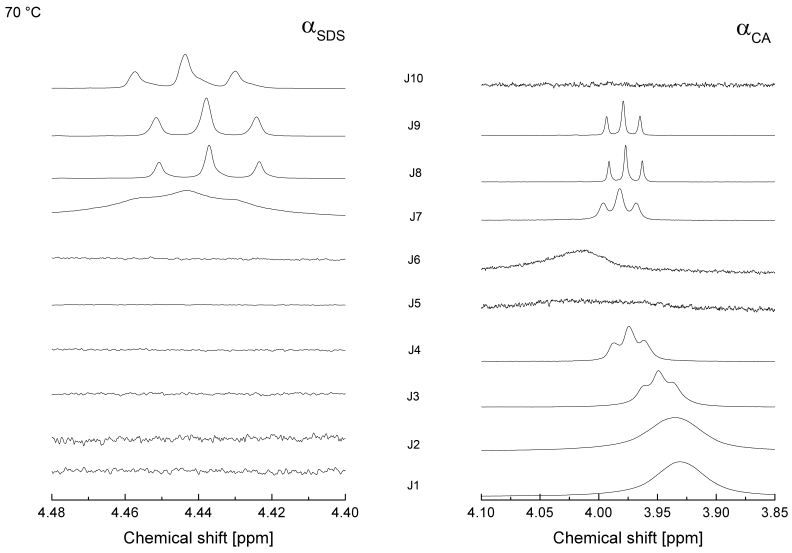

Figure 7.24: *Enlarged signals of the α-CH_2 groups of the J samples at 70 ˚C.*

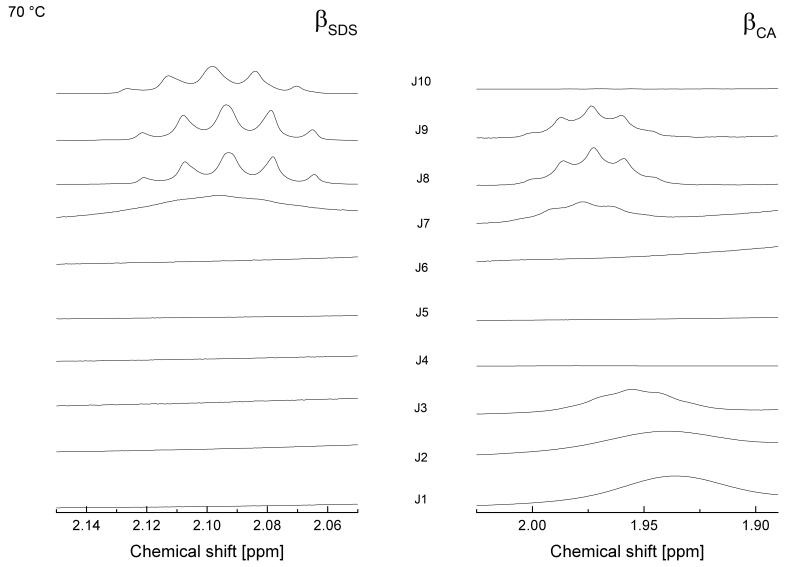

Figure 7.25: *Enlarged signals of the β-CH_2 groups of the J samples at 70 ˚C.*

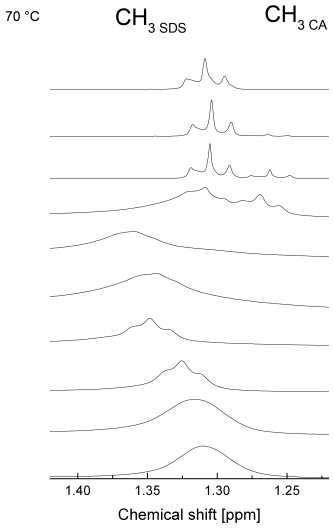

Figure 7.26: *Enlarged signals of the CH_3 groups of the J samples at 70 ˚C.*

7.4.2.2 Enlarged signals of the J14-1 to J14-10 spectra at 30 °C and 55 °C

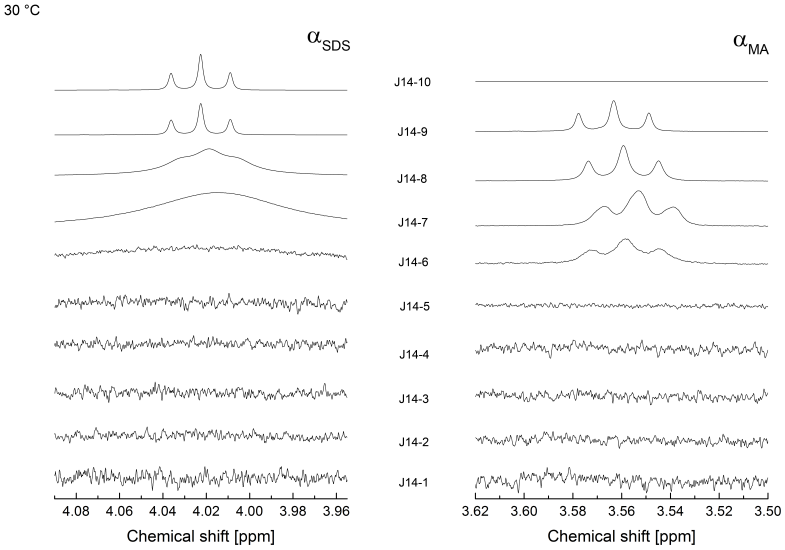

Figure 7.27: *Enlarged signals of the α-CH_2 groups of the J14 samples at 30 °C.*

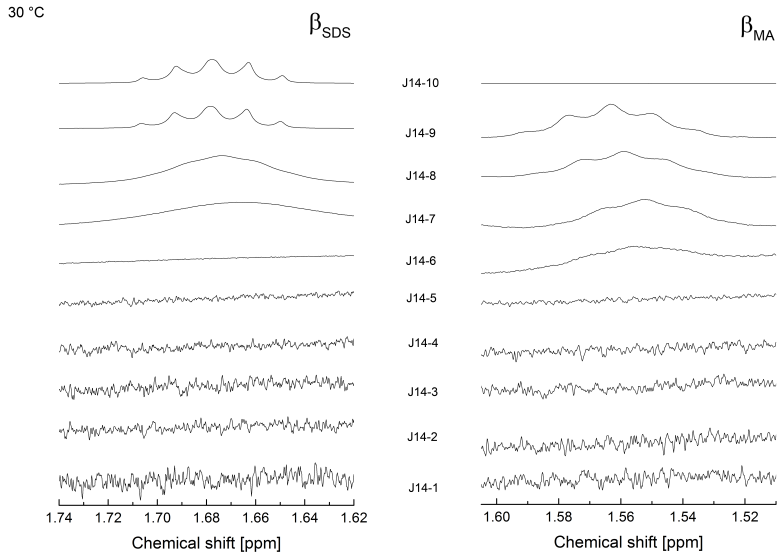

Figure 7.28: *Enlarged signals of the β-CH_2 groups of the J14 samples at 30 °C.*

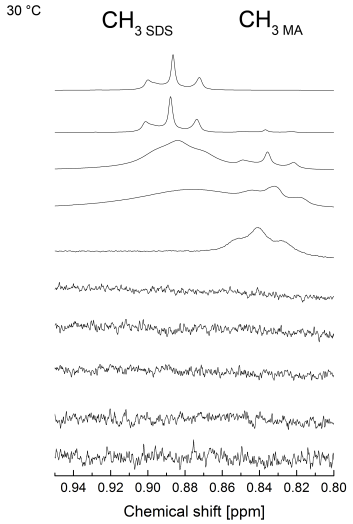

Figure 7.29: *Enlarged signals of the CH_3 groups of the J14 samples at 30 ˚C.*

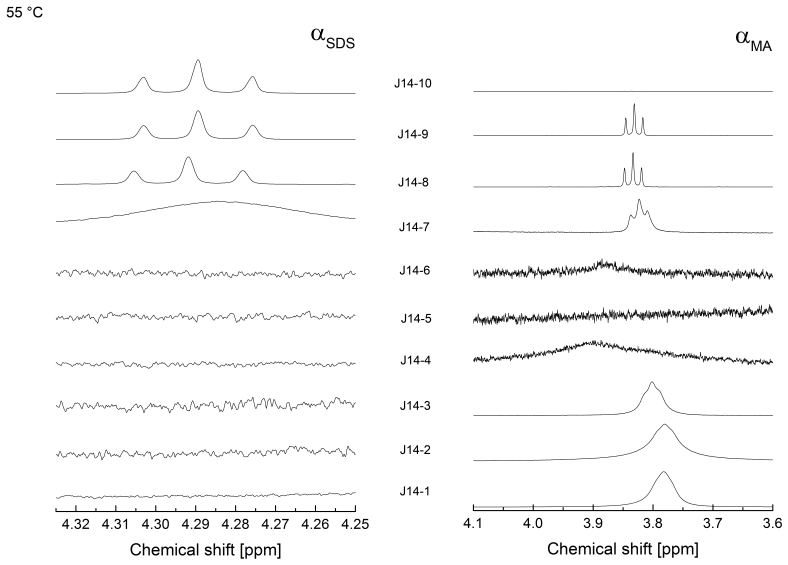

Figure 7.30: *Enlarged signals of the α-CH_2 groups of the J14 samples at 55 ˚C.*

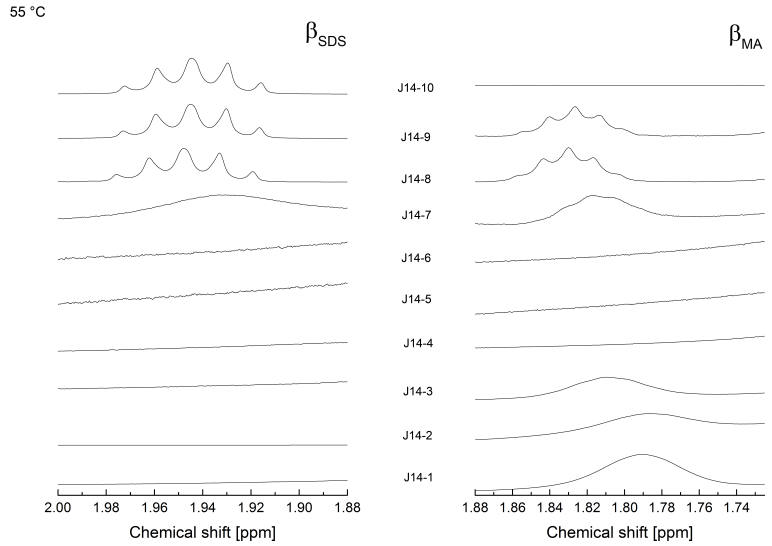

Figure 7.31: *Enlarged signals of the β-CH_2 groups of the J14 samples at 55 °C.*

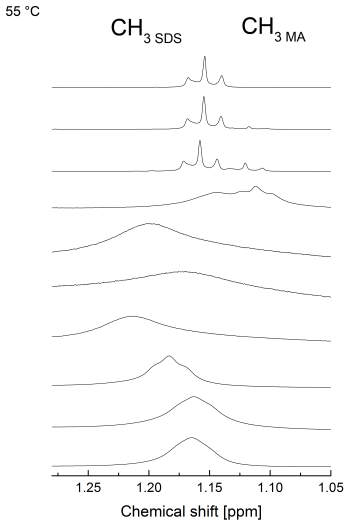

Figure 7.32: *Enlarged signals of the CH_3 groups of the J14 samples at 55 °C.*

7.4.2.3 CH_3 groups of CTAB at 5, 10, 12, 15 and 20 wt. %

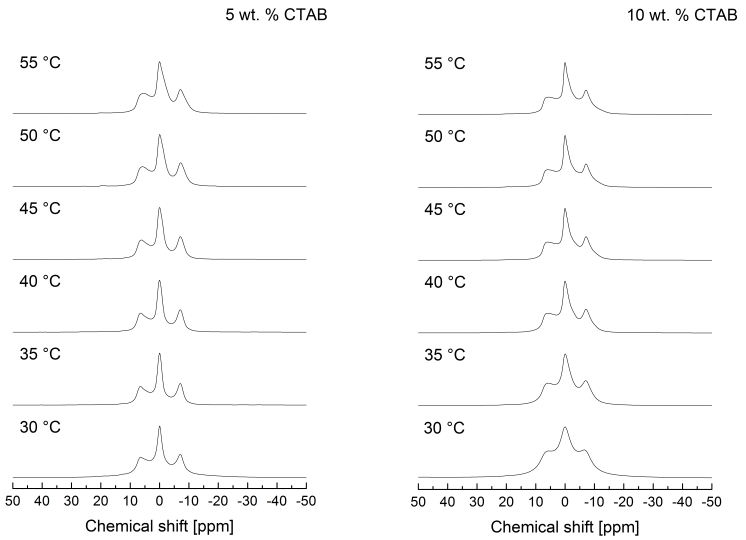

Figure 7.33: *CH_3 groups of CTAB at 5 and 10 wt. %.*

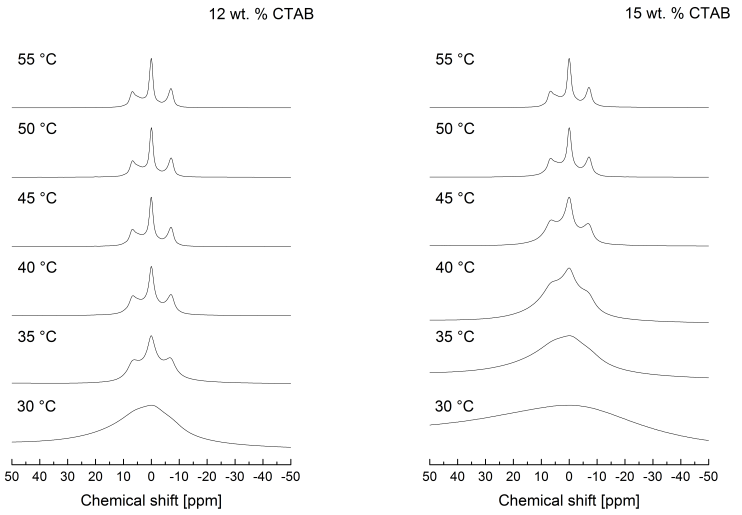

Figure 7.34: *CH_3 groups of CTAB at 12 and 15 wt. %.*

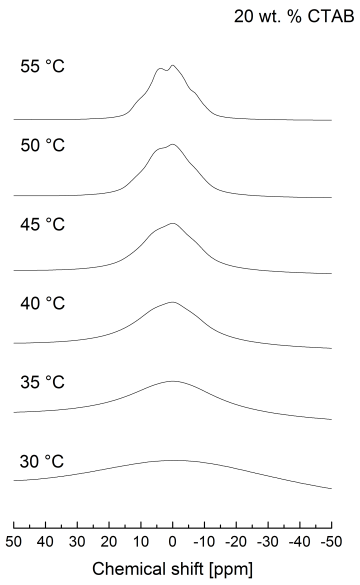

Figure 7.35: *CH_3 groups of CTAB at 20 wt. %.*

7.4.3 SAXS curves

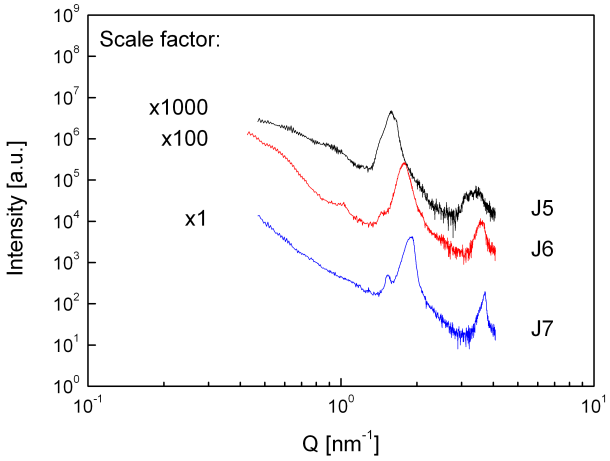

Figure 7.36: *SAXS curves of samples J5 to J7.*

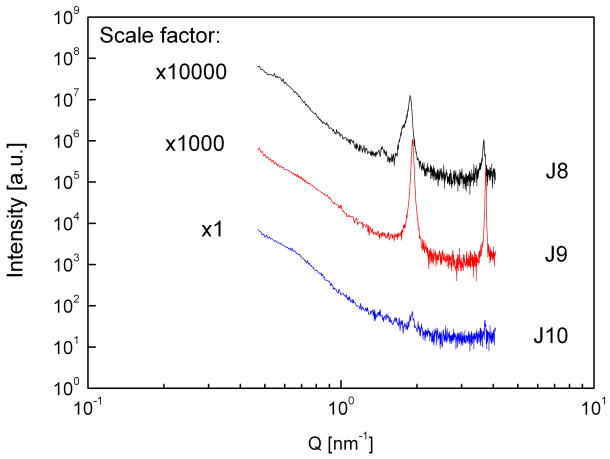

Figure 7.37: *SAXS curves of samples J8 to J10.*

7.4.4 SANS curves

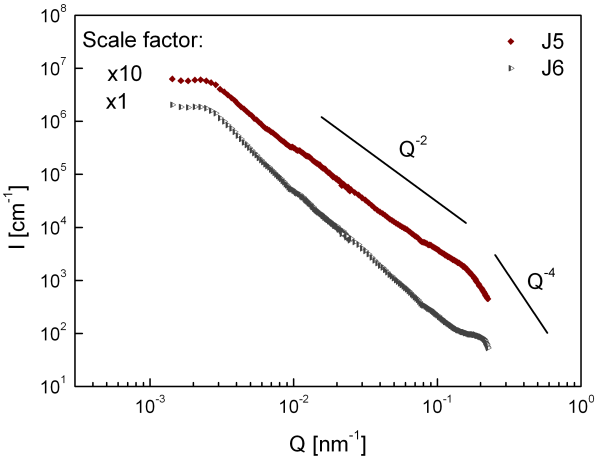

Figure 7.38: *SANS curves of samples J5 and J6.*

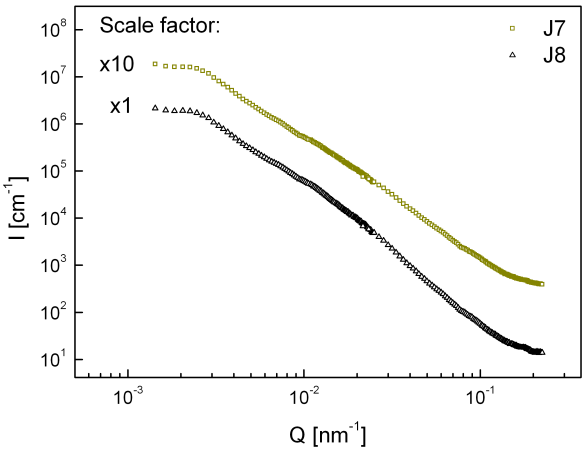

Figure 7.39: *SANS curves of samples J7 and J8.*

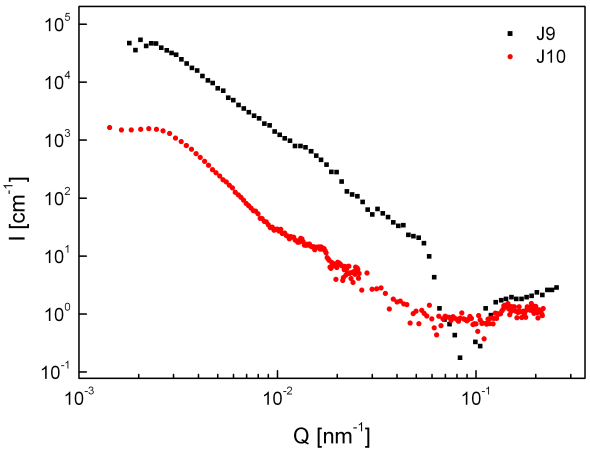

Figure 7.40: *SANS curves of samples J9 and J10.*

7.4.5 Rheology curves

7.4.5.1 Amplitude sweeps

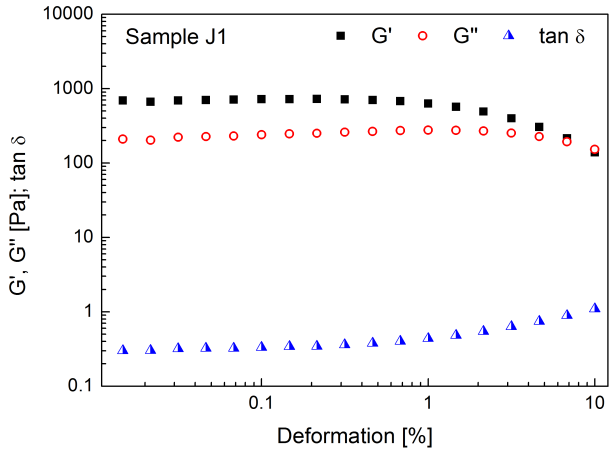

Figure 7.41: *Amplitude sweep of sample J1 at 30 °C.*

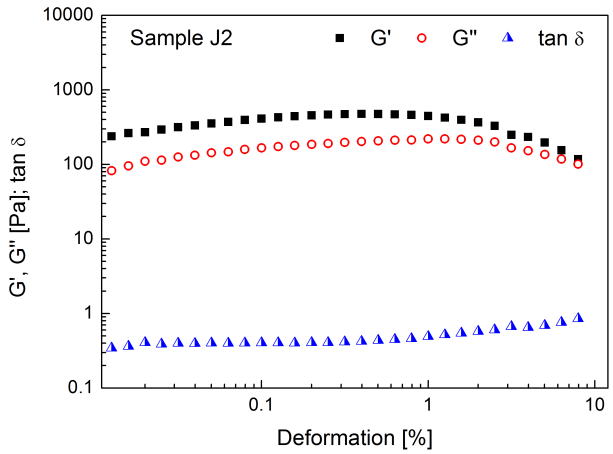

Figure 7.42: *Amplitude sweep of sample J2 at 30 °C.*

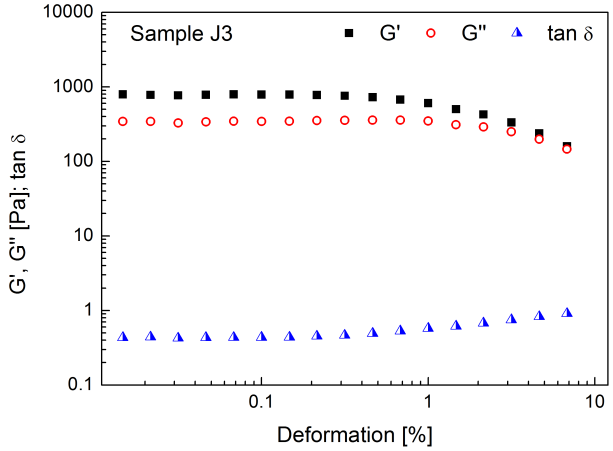

Figure 7.43: *Amplitude sweep of sample J3 at 30 ˚C.*

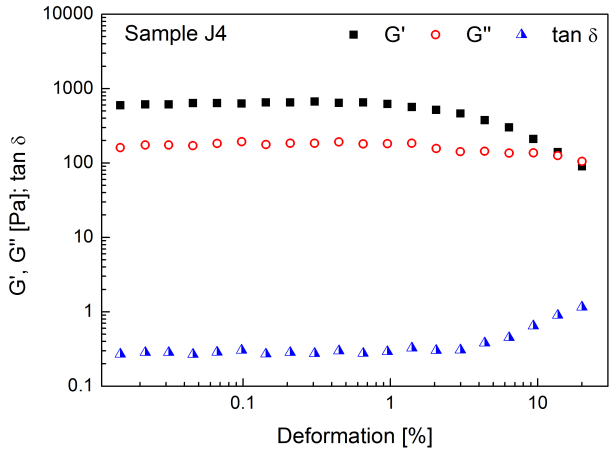

Figure 7.44: *Amplitude sweep of sample J4 at 30 ˚C.*

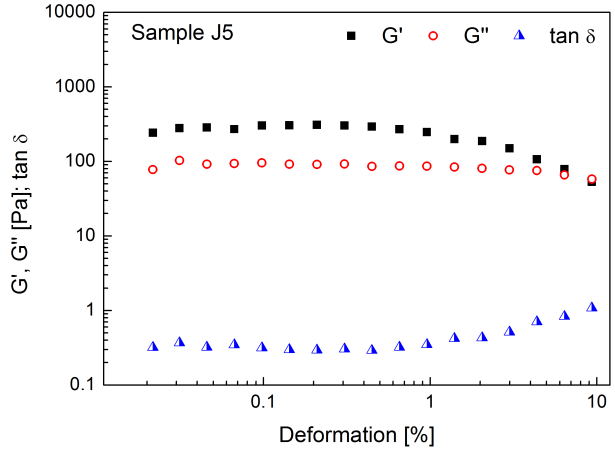

Figure 7.45: *Amplitude sweep of sample J5 at 30 °C.*

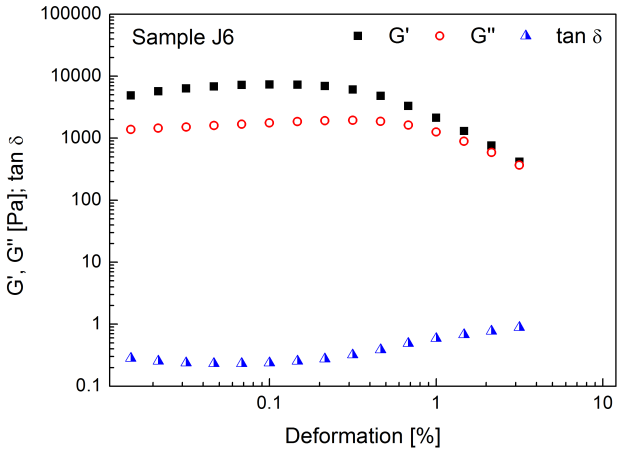

Figure 7.46: *Amplitude sweep of sample J6 at 30 °C.*

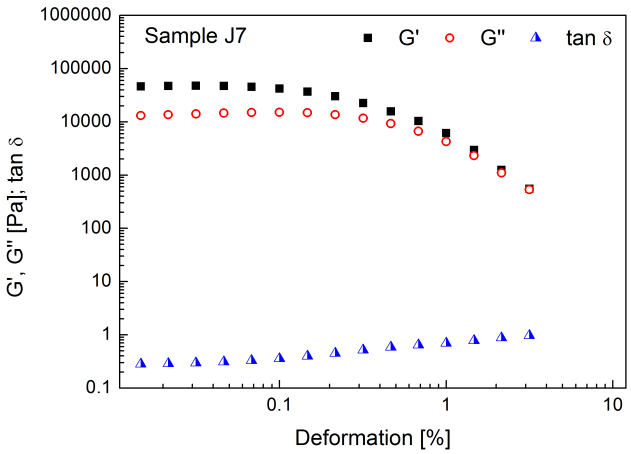

Figure 7.47: *Amplitude sweep of sample J7 at 30 °C.*

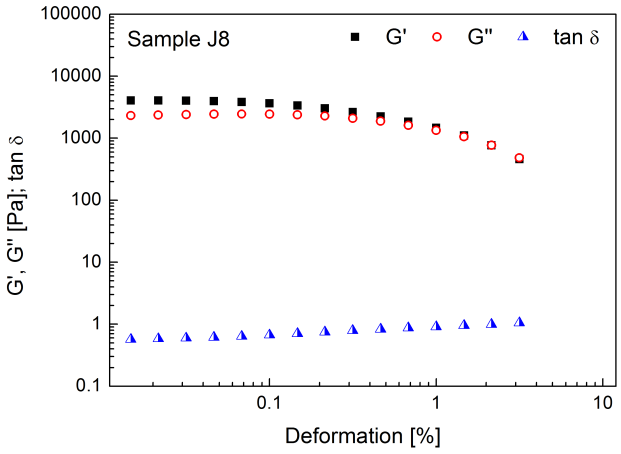

Figure 7.48: *Amplitude sweep of sample J8 at 30 °C.*

7.4.5.2 Frequency sweeps

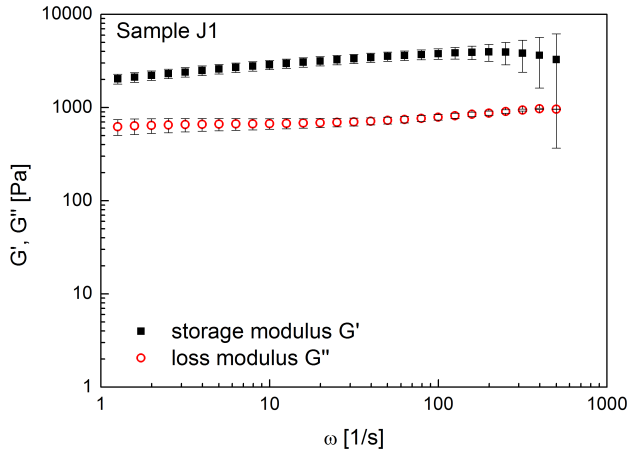

Figure 7.49: *Frequency sweep of sample J1 at 30 °C (used deformation: 0.2 %).*

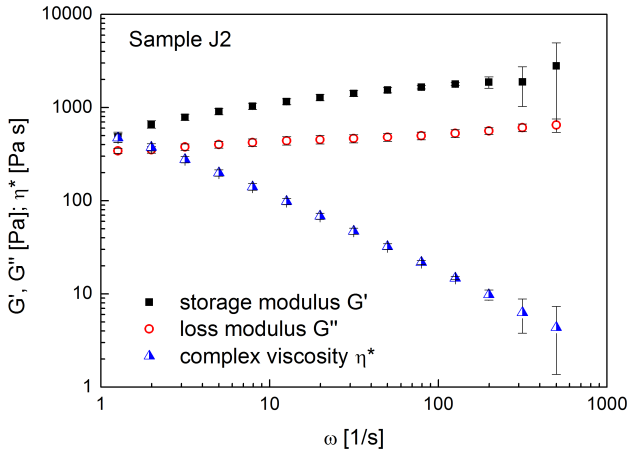

Figure 7.50: *Frequency sweep of sample J2 at 30 °C (used deformation: 0.2 %).*

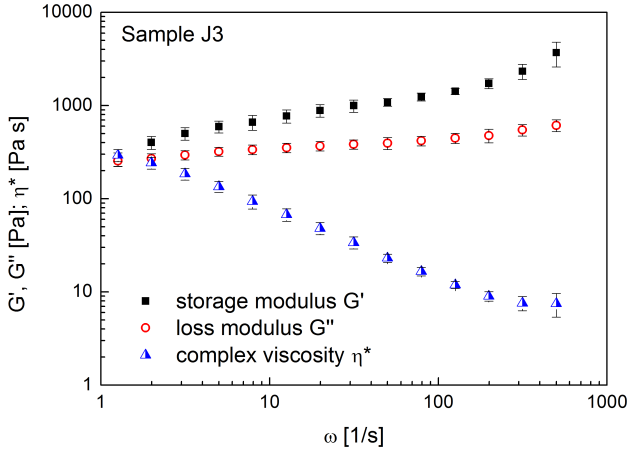

Figure 7.51: *Frequency sweep of sample J3 at 30 °C (used deformation: 0.2 %).*

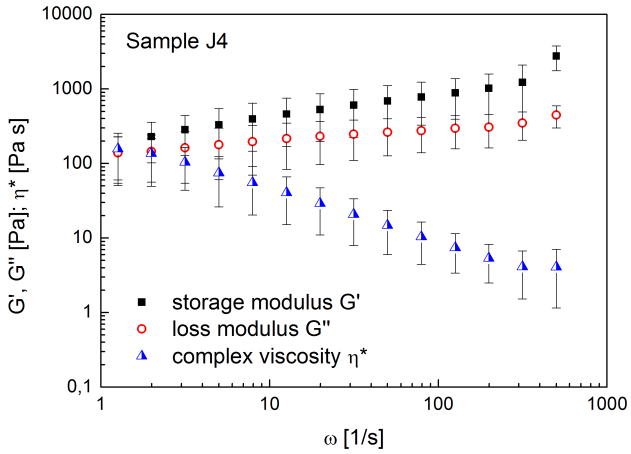

Figure 7.52: *Frequency sweep of sample J4 at 30 °C (used deformation: 0.2 %).*

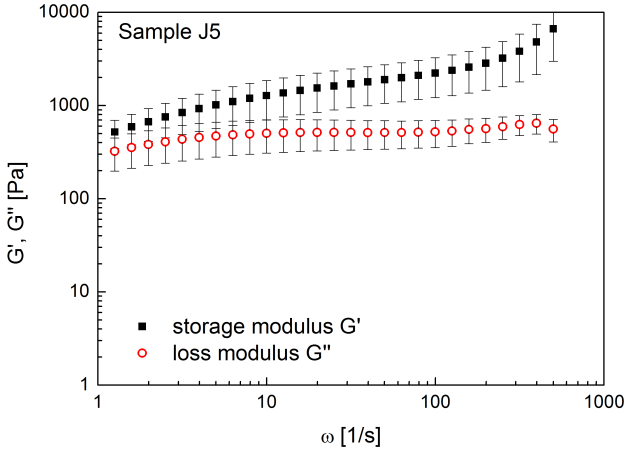

Figure 7.53: *Frequency sweep of sample J5 at 30 °C (used deformation: 0.2 %).*

7.4.5.3 Determination of the viscosity of samples J1 to J6

Figure 7.54 shows the viscosities of samples J1 to J6 determined via rotational measurements. The samples were presheared for 5 min at a shear rate of 1 s^{-1}. Then the samples were sheared for 1300 s at different shear rates. All samples achieved a plateau during the measurements. The shown value is the average of the experimental data recorded from 1260–1300 s.

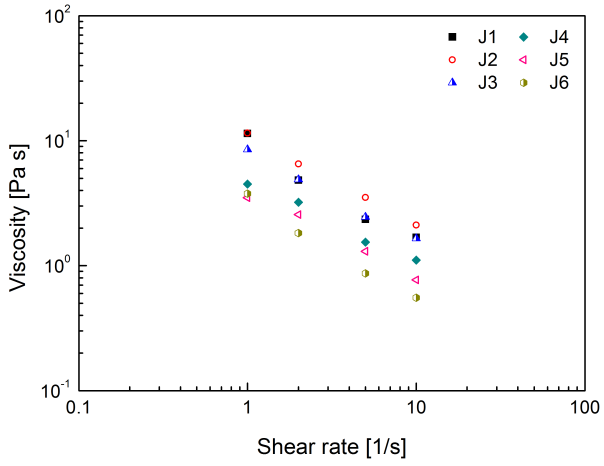

Figure 7.54: *Viscosities of samples J1 to J6.*

Bibliography

[1] D. F. Evans and H. Wennerström, *The Colloidal Domain - Where Physics, Chemistry, Biology, and Technology Meet*, 2nd ed. (Wiley-VCH Publischers, New York, 1999).

[2] R. J. Goetz and M. S. El-Aasser, Langmuir **6**, 132 (1990).

[3] T. S. Awad, E. S. Johnson, A. Bureiko, and U. Olsson, Journal of Dispersion Science and Technology **32**, 807 (2011).

[4] J. F. Yan and M. B. Palmer, Journal of Colloid and Interface Science **30**, 177 (1969).

[5] B. V. N. P. Kumar, S. U. Priyadharsini, G. K. S. Prameela, and A. B. Mandal, Journal of Colloid and Interface Science **360**, 154 (2011).

[6] S. Barhoum and A. Yethiraj, Journal of Chemical Physics **132**, 024909 (2010).

[7] K. D. Lawson and T. J. Flautt, Journal of Physical Chemistry **72**, 2066 (1968).

[8] L. L. Schramm, E. N. Stasiuk, and D. G. Marangoni, Annual Reports Section C **99**, 3 (2003).

[9] C. C. Ho, R. J. Goetz, and M. S. El-Aasser, Langmuir **7**, 630 (1991).

[10] T. de Vringer, J. G. H. Joosten, and H. E. Junginger, Colloid and Polymer Science **265**, 167 (1987).

[11] T. de Vringer, J. G. H. Joosten, and H. E. Junginger, Colloid and Polymer Science **265**, 448 (1987).

[12] O. Diat, D. Roux, and F. Nallet, Journal de Physique II **3**, 1427 (1993).

[13] W. Richtering, Current Opinion in Colloid & Interface Science **6**, 446 (2001).

[14] K. Mortensen, Current Opinion in Colloid & Interface Science **6**, 140 (2001).

[15] M. G. Berni, C. J. Lawrence, and D. Machin, Advances in Colloid and Interface Science **98**, 217 (2002).

[16] M. Gradzielski, Journal of Physics: Condensed Matter **15**, 655 (2003).

[17] M. Bergmeier, H. Hoffmann, and C. Thunig, The Journal of Physical Chemistry B **101**, 5767 (1997).

[18] P. T. Callaghan, Reports on Progress in Physics **62**, 599 (1999).

[19] E. Fukushima, Annual Review of Fluid Mechanics **31**, 95 (1999).

[20] P. T. Callaghan, Encyclopedia of Magnetic Resonance **9**, 737 (2002).

[21] P. T. Callaghan, Current Opinion in Colloid & Interface Science **11**, 13 (2006).

[22] C. Schmidt and H. W. Spiess, in *Handbook of Liquid crystals*, edited by D. Demus, J. Goodby, G. W. Gray, H. W. Spiess, and V. Vill (Wiley-VCH, Weinheim, 1998), Vol. 1, pp. 595–618.

[23] A. I. Nakatani, M. D. Poliks, and E. T. Samulski, Macromolecules **23**, 2686 (1990).

[24] M. V. Badiger, P. R. Rajamohanan, P. M. Suryavanshi, S. Ganapathy, and R. A. Mashelkar, Macromolecules **35**, 126 (2002).

[25] P. T. Callaghan and A. M. Gil, Macromolecules **33**, 4116 (2000).

[26] J. Eastoe, in *Colloid Science: Principles, Methods and Applications*, edited by T. Cosgrove (Blackwell Publishing Ltd, Bristol, 2005), pp. 50–76.

[27] K. Hiltrop, in *Lyotrope Flüssigkristalle: Grundlagen, Entwicklung, Anwendung*, edited by H. Stegemeyer (Steinkopff Verlag, Darmstadt, 1999), pp. 1–57.

[28] K. Hiltrop, in *Liquid Crystals*, edited by H. Stegemeyer (Steinkopff Verlag, Darmstadt, 1994), pp. 143–171.

[29] C. Tanford, Science Magazine **200**, 1012 (1978).

[30] I. W. Hamley, *Introduction to soft matter: synthetic and biological self-assembling materials*, revised ed. (Wiley, West Sussex, 2007), pp. 160–220.

[31] H.-D. Dörfler, *Grenzflächen und kolloid-disperse Systeme: Physik und Chemie* (Springer Verlag, Berlin; Heidelberg, 2002).

[32] J. N. Israelachvili, D. J. Mitchell, and B. W. Ninham, Journal of the Chemical Society, Faraday Transactions 2 **72**, 1525 (1976).

[33] P. Mukerjee, P. Kapauan, and H. G. Meyer, Journal of Physical Chemistry **70**, 783 (1966).

[34] S. S. Berr, Journal of Physical Chemistry **91**, 4760 (1987).

[35] L. Q. Amaral, O. S. Filho, G. Taddei, and N. Vila-Romeu, Langmuir **13**, 5016 (1997).

[36] E. O. Stejskal, Journal of Chemical Physics **43**, 3597 (1965).

[37] E. O. Stejskal and J. E. Tanner, Journal of Chemical Physics **42**, 288 (1965).

[38] W. S. Price and P. W. Kuchel, Journal of Magnetic Resonance **94**, 133 (1991).

[39] W. S. Price, Concepts in Magnetic Resonance **9**, 299 (1997).

[40] W. S. Price, Concepts in Magnetic Resonance **10**, 197 (1998).

[41] T. G. Mezger, *Das Rheologie Handbuch: Für Anwender von Rotations- und Oszillations-Rheometern*, 3. überarbeitete ed. (Vincentz Network, Hannover, 2010).

[42] J. B. Lambert, S. Gronert, H. F. Shurvell, and D. A. Lightner, *Spektroskopie - Strukturaufklärung in der Organischen Chemie*, 2., aktualisierte ed. (Pearson Deutschland, München, 2012).

[43] H. Günther, *NMR-Spektroskopie: Grundlagen, Konzepte und Anwendungen der Protonen- und Kohlenstoff-13-Kernresonanz-Spektroskopie in der Chemie*, 3. neubearbeitete und erweiterte ed. (Georg Thieme Verlag, Stuttgart, 1992).

[44] M. Karplus, The Journal of Chemical Physics **30**, 11 (1959).

[45] V. F. Bystrov, Russian Chemical Reviews **41**, 281 (1972).

[46] *http://www.chemgapedia.de (18.07.2013).*

[47] *Small Angle X-ray scattering*, edited by O. Glatter and O. Kratky (Academic Press, London, 1982).

[48] P. Kékicheff, C. Grabielle-Madelmont, and M. Ollivon, Journal of Colloid and Interface Science **131**, 112 (1989).

[49] J. Zhao and B. M. Fung, Langmuir **9**, 1228 (1993).

[50] M. Varshney, Colloids and Surfaces A **96**, 273 (1995).

[51] H. Wennerström and B. Lindman, Physics Reports **52**, 1 (1979).

[52] R. E. Wasylishen and J. A. Ripmeester, Journal of Magnetic Resonance **65**, 162 (1985).

[53] J. S. Clawson, G. P. Holland, and T. M. Alam, Journal of Physical Chemistry **8**, 2635 (2006).

[54] X. Auvray, C. Petipas, R. Anthore, I. Rico, and A. Lattes, Journal of Physical Chemistry **93**, 7458 (1989).

[55] P. J. Kreke, L. J. Magid, and J. C. Gee, Langmuir **12**, 699 (1996).

[56] J. Cheng, A. Xenopoulos, and B. Wunderlich, Magnetic Resonance in Chemistry **30**, 917 (1992).

[57] C. C. Ho, R. J. Goetz, M. S. El-Aasser, J. W. Vanderhoff, and F. M. Fowkes, Langmuir **7**, 56 (1991).

[58] S. Fukushima and M. Yamaguchi, in *Surface and colloid science Volume*, Vol. 16 of *surface and colloid science*, edited by E. Matijevic (Kluwer Academic/Plenum Publishers, New York, 2001), pp. 1–98.

[59] K. Higasi and M. Kubo, Scientific Papers of the Institute of Physical and Chemical Research (Japan) **36**, 286 (1939).

[60] A. Trapeznikov, Acta Physicochimica URSS **20**, 589 (1945).

[61] A. Lawrence, A. Bingham, C. B. Capper, and K. Hume, The Journal of Physical Chemistry **68**, 3470 (1964).

[62] J. H. Brooks and A. E. Alexander, in *The Spreading Behavior and Crystalline Phases of Fatty Alcohols*, edited by V. K. L. Mer (Academic Press, New York, 1962), pp. 245–269.

[63] J. H. Brooks and A. E. Alexander, The Journal of Chemical Physics **66**, 1851 (1962).

[64] H. E. Gottlieb, V. Kotlyar, and A. Nudelman, Journal of Organic Chemistry **62**, 7512 (1997).

[65] E. Y. Sheu, M. B. Shields, and D. A. Storm, ACS Symposium Series **578**, 167 (1994).

[66] G. Goerigk and Z. Varga, Journal of Applied Crystallography **44**, 337 (2011).

[67] C. A. McKelvey and E. W. Kaler, Journal of Colloid and Interface Science **245**, 68 (2002).

[68] L. L. Brasher and E. W. Kaler, Langmuir **12**, 6270 (1996).

[69] L. Auvray and P. Auroy, in *Neutron, X-Ray and Light Scattering: Introduction to an Investigative Tool for Colloidal and Polymeric Systems*, edited by P. Lindner and T. Zemb (North-Holland Delta Series, Amsterdam, 1991), pp. 199–221.

[70] P. Alexandridis, U. Olsson, and B. Lindman, Langmuir **14**, 2627 (1998).

[71] M. Minasyants, V. Zakaryan, A. Shaginyan, and I. Chistayakov, Kristallografiya **24**, 319 (1979).

[72] H. Weingärtner, Zeitschrift fur Physikalische Chemie Neue Folge **132**, 129 (1982).

[73] H. M. Ribeiro, J. A. Morais, and G. M. Eccleston, International Journal of Cosmetic Science **26**, 47 (2004).

[74] P. Kudla, T. Sokolowski, B. Blümich, and K.-P. Wittern, Journal of Colloid and Interface Science **349**, 554 (2010).

[75] S. Ishikawa and I. Ando, Journal of Molecular Structure **271**, 57 (1992).

[76] C. Mosselman, J. Mourik, and H. Dekker, Journal of Chemical Thermodynamics **6**, 477 (1974).

[77] *The Physical Chemistry of Lipids. From Alkanes to Phospholipids*, Vol. 4 of *Handbook of Lipid Research*, edited by D. M. Small (Plenum Press, New York, 1986), pp. 233–284.

[78] A. Patist, T. Axelberd, and D. O. Shah, Journal of Colloid and Interface Science **208**, 259 (1998).

[79] B. Medronho, S. Shafaei, R. Szopko, M. G. Miguel, U. Olsson, and C. Schmidt, Langmuir **24**, 6480 (2008).

[80] S. Müller, C. Börschig, W. Gronski, C. Schmidt, and D. Roux, Langmuir **15**, 7558 (1999).

[81] D. M. Ginsberg and M. J. Melchner, Review of Scientific Instruments **41**, 122 (1970).

[82] C. E. G. Salmon, E. L. G. Vidoto, M. J. Martins, and A. Tannus, Brazilian Journal of Physics **36**, 4 (2006).

[83] H. Stroppe, *Physik für Studenten der Natur- und Technikwissenschaften*, 10., verbesserte ed. (Fachbuchverlag Leipzig GmbH, Leipzig, 1994), pp. 280–282.

[84] A. N. Temnikov, Instruments and Experimental Techniques **48**, 636 (2005).

[85] L. Bedjaoui, N. Gogibus, B. Ewen, T. Pakula, X. Coqueret, M. Benmouna, and U. Maschke, Polymer **45**, 6555 (2004).

[86] *http://www.qtikws.de (02.07.2013).*

[87] G. D. Wignall and F. S. Bates, Journal of Applied Crystallography **20**, 28 (1987).

[88] K. Nusser, S. Neueder, G. J. Schneider, M. Meyer, W. Pyckhout-Hintzen, L. Willner, A. Radulescu, and D. Richter, Macromolecules **43**, 9837 (2010).